AFML-TR-76-215

NONLINEAR MULTIAXIAL MODELING OF GRAPHITIC AN CARBON-CARBON MATERIALS

ROBERT M. JONES
CIVIL & MECHANICAL ENGINEERING DEPARTMENT
SCHOOL OF ENGINEERING AND APPLIED SCIENCE
SOUTHERN METHODIST UNIVERSITY
DALLAS, TEXAS 75275

DECEMBER 1976

FINAL REPORT MARCH 1975 - JUNE 1976

Approved for public release; distribution unlimited

AIR FORCE MATERIALS LABORATORY
AIR FORCE WRIGHT AERONAUTICAL LABORATORIES
AIR FORCE SYSTEMS COMMAND
WRIGHT-PATTERSON AIR FORCE BASE, OHIO 45433

NOTICE

When Government drawings, specifications, or other data are used for any purpose other than in connection with a definitely related Government procurement operation, the United States Government thereby incurs no responsibility nor any obligation whatsoever; and the fact that the Government may have formulated, furnished, or in any way supplied the said drawings, specifications, or other data, is not to be regarded by implication or otherwise as in any manner licensing the holder or any other person or corporation, or conveying any rights or permission to manufacture, use, or sell any patented invention that may in any way be related thereto.

This technical report has been reviewed and is approved for publication.

Clarence A. Pratt
Project Monitor
Space and Missiles Branch
Systems Support Division
AF Materials Laboratory

FOR THE DIRECTOR

Albert Olevitch, Chief
Non-Metals Materials Branch
Systems Support Division
AF Materials Laboratory

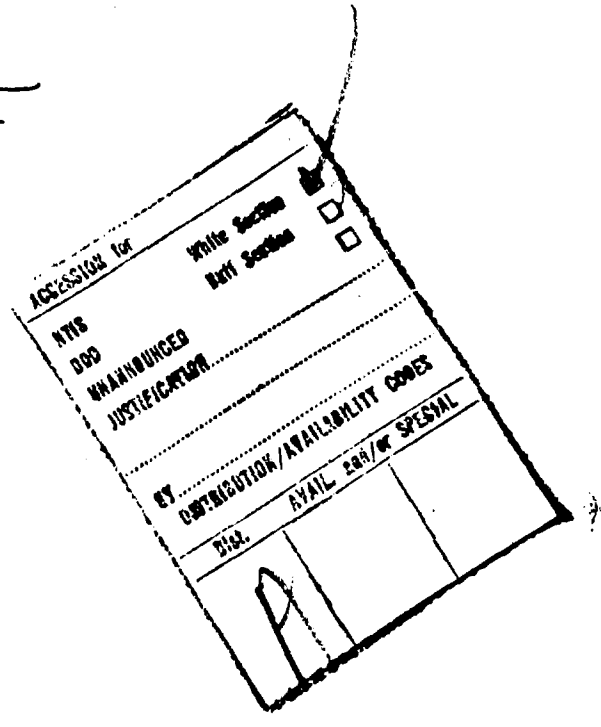

Copies of this report should not be returned unless return is required by security considerations, contractural obligations, or notice on a specific document.

UNCLASSIFIED

SECURITY CLASSIFICATION OF THIS PAGE (When Data Entered)

REPORT DOCUMENTATION PAGE	READ INSTRUCTIONS BEFORE COMPLETING FORM
1. REPORT NUMBER: AFML-TR-76-215	2. GOVT ACCESSION NO. / 3. RECIPIENT'S CATALOG NUMBER
4. TITLE (and Subtitle): NONLINEAR MULTIAXIAL MODELING OF GRAPHITIC AND CARBON-CARBON MATERIALS.	5. TYPE OF REPORT & PERIOD COVERED: FINAL TECHNICAL REPORT. MAR 75 — JUN 76.
	6. PERFORMING ORG. REPORT NUMBER: none
7. AUTHOR(s): ROBERT M. JONES, III	8. CONTRACT OR GRANT NUMBER(s): F33615-75-C-5212
9. PERFORMING ORGANIZATION NAME AND ADDRESS: CIVIL AND MECHANICAL ENGINEERING DEPARTMENT, SCHOOL OF ENGINEERING AND APPLIED SCIENCE, SOUTHERN METHODIST UNIVERSITY DALLAS, TX 75275	10. PROGRAM ELEMENT, PROJECT, TASK AREA & WORK UNIT NUMBERS
11. CONTROLLING OFFICE NAME AND ADDRESS: AIR FORCE MATERIALS LABORATORY/MXS, WRIGHT-PATTERSON AFB, OHIO 45433	12. REPORT DATE: JUNE 1976 (11) DEC 76
	13. NUMBER OF PAGES: (12) 197 p.
14. MONITORING AGENCY NAME & ADDRESS (if different from Controlling Office)	15. SECURITY CLASS. (of this report): UNCLASSIFIED
	15a. DECLASSIFICATION/DOWNGRADING SCHEDULE

16. DISTRIBUTION STATEMENT (of this Report)

Approved for Public Release; Distribution Unlimited

17. DISTRIBUTION STATEMENT (of the abstract entered in Block 20, if different from Report)

18. SUPPLEMENTARY NOTES

19. KEY WORDS (Continue on reverse side if necessary and identify by block number)

Graphite, Carbon-Carbon, Composite Materials, Orthotropy, Anisotropy, Stress Analysis, Material Modeling

20. ABSTRACT (Continue on reverse side if necessary and identify by block number)

The nonlinear material model due to Jones and Nelson is extended to temperature-dependent material behavior and applied to the analysis of the Southern Research Institute Thermal Stress Disk Test. The predicted diametral deformations of the annular disk are within three percent of the measured deformations at three times in a specific test. The Jones-Nelson model is extended to treatment of materials with first nonlinear then linear stress-strain behavior in what is called the Jones-Nelson-Morgan nonlinear material model. The JNM model is necessary for materials with strong nonlinearities as

DD FORM 1 JAN 73 1473 EDITION OF 1 NOV 65 IS OBSOLETE

UNCLASSIFIED

SECURITY CLASSIFICATION OF THIS PAGE (When Data Entered)

BLOCK 20. ABSTRACT, continued

is demonstrated for ATJ-S graphite in a reentry vehicle nosetip stress analysis. The JNM model is also speculated to be useful for carbon-carbon materials because all pertinent numbers and types of nonlinearities can be treated. A linear elastic multimodulus analysis is used to demonstrate that the ASTM Flexure Test does not lead to useful results for carbon-carbon and other multimodulus materials. Necessary future modeling work for carbon-carbon is outlined.

FOREWORD

This final report is submitted by the Civil and Mechanical Engineering Department, School of Engineering and Applied Science, Southern Methodist University, Dallas, Texas 75275 under USAF Contract F33615-75-C-5212. The work, an extension of the nonlinear deformation material model for graphitic reentry vehicle nosetip materials, was performed for the Air Force Materials Laboratory, Wright-Patterson AFB, Ohio 45433. The AFML/MXS project monitors in order of service were Captain Charles L. Budde, Lt. Terry Hinnerichs, Captain Perry Cockerham, and Mr. Clarence A. Pratt.

Dr. Robert M. Jones was the Principal Investigator. The assistance of Mr. Harold S. Morgan in developing and discussing the extended stress-strain curve approach and the JNMDATA computer program is gratefully acknowledged. The extensive cooperation of Mr. H. Stuart Starrett, Head, Analytical Section, Mechanical Engineering Division, Southern Research Institute, Birmingham, Alabama 35205 in interpreting various experimental results is sincerely appreciated.

TABLE OF CONTENTS

TABLE OF CONTENTS, continued

LIST OF FIGURES

LIST OF FIGURES, continued

LIST OF FIGURES, continued

LIST OF FIGURES, continued

LIST OF FIGURES, continued

LIST OF TABLES

TABLES, continued

1. INTRODUCTION

Artificial graphitic materials have been used for more than the past decade in reentry vehicle nosetips. The exacting requirements imposed in their use necessitate accurate stress analysis techniques. An integral part of every stress analysis is the stress-strain relationship or material model.

The stress analysis problems inherent to reentry vehicle nosetip design were discussed by Jones [1-1] in 1967 along with numerous specific problems by other authors in the same conference proceedings volume. Since that time, periodic reviews of nosetip stress analysis technology have been made. The most recent review by Jones and Koenig [1-2] is addressed to the material modeling characteristics necessary for graphite and carbon-carbon. Two of the significant deficiencies of current material modeling that they point out are (1) biaxial softening and (2) different moduli under tensile loading than under compressive loading. These characteristics are described along with other characteristics of graphite and carbon-carbon in the following paragraphs.

1.1 BIAXIAL SOFTENING

Biaxial softening is characterized by the development of slightly larger strains in biaxial tension than in uniaxial tension, as shown in Figure 1-1. This behavior of generally decreasing Poisson's ratios is in contradiction to what might be anticipated on the basis of conventional Poisson effects (where ν increases). This phenomenon was apparently first observed by Jortner [1-3 thru 1-6] for graphite and is attributed to plastic volume changes resulting from internal tearing or microcracking. Jones and Nelson [1-7] developed a material model for descrip-

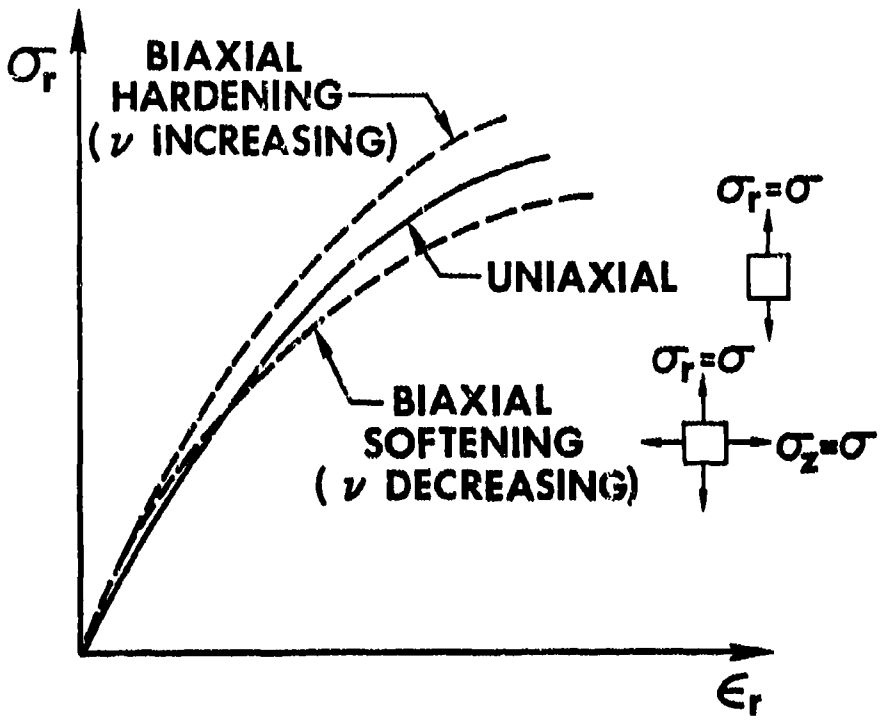

FIGURE 1-1 BIAXIAL SOFTENING OF GRAPHITE

tion of the deformation behavior of ATJ-S graphite under biaxial tension. Their model is used in the SAAS III program to obtain predicted strains for Jortner's biaxial test specimen shown in Fig. 1-2. The predicted strains are shown along with Jortner's experimentally observed strains in Figure 1-3 for room temperature behavior at a constant principal stress of 3550 psi. The Jones and Nelson strain predictions are within 3% of the equal biaxial tension strains and are identical to the two uniaxial tension cases.

Actually, the Jones-Nelson model is more a general model for non-linear behavior of orthotropic materials than just a biaxial softening model. Thus, the Jones-Nelson model should be considered for use in

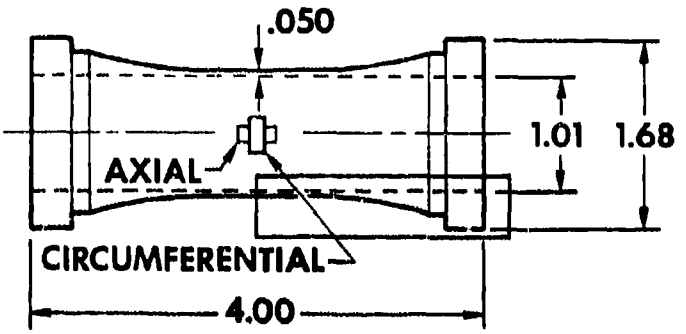

FIGURE 1-2 HOLLOW GRAPHITE BIAXIAL SPECIMEN

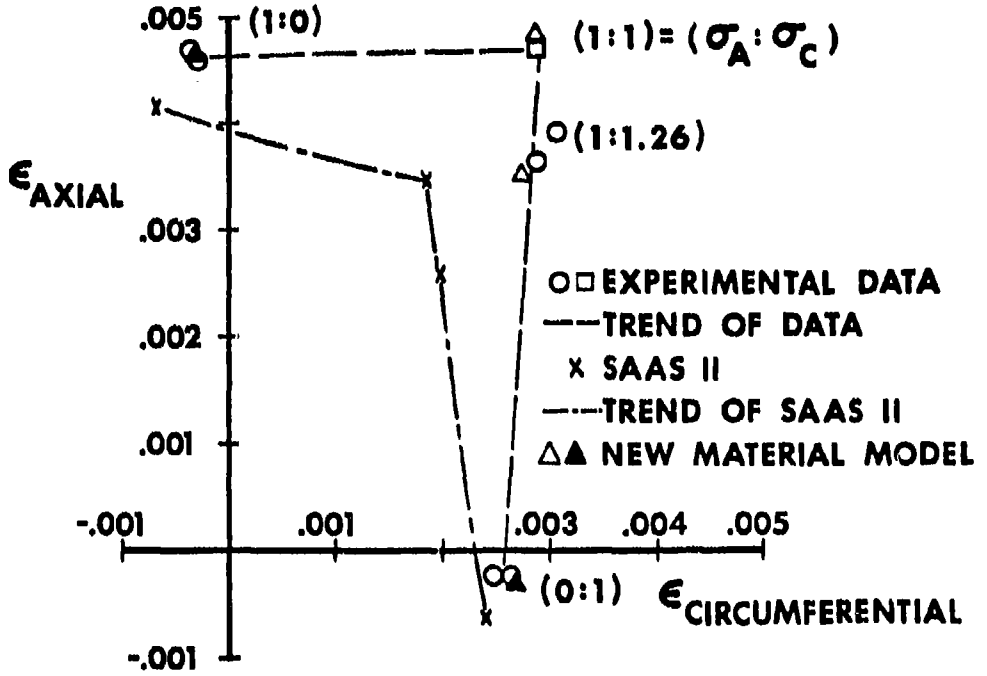

FIGURE 1-3 BIAXIAL STRAIN RESPONSE OF A HOLLOW ATJ-S GRAPHITE SPECIMEN AT ROOM TEMPERATURE (70°F) AND 3550 psi PRINCIPAL STRESS

modeling other materials. Specifically, carbon-carbon will be shown to be a nonlinear orthotropic material, and the basic Jones-Nelson model will be proposed for analysis of carbon-carbon.

1.2 DIFFERENT MODULI IN TENSION AND COMPRESSION

Many composite materials behave differently under tensile and compressive loads. Both the elastic moduli (stiffnesses) and the strengths in principal material property directions of these orthotropic materials are different for tensile loading than for compressive loading. This characteristic behavior is shown schematically in the stress-strain curve of Figure 1-4. This phenomenon is but one of several differences that make composite materials more difficult to analyze (and hence design) than the more common structural materials such as aluminum.

Both fiber-reinforced and granular composite materials have different moduli in tension and compression as displayed in Table 1-1. Unidirectional glass fibers in an epoxy matrix have compression moduli 20% lower than the tension moduli [1-8]. For some unidirectional boron/epoxy fiber-reinforced laminae, the compression moduli are about 15-20% larger than the tension moduli [1-9]. In contrast, some unidirectional graphite/epoxy fiber-reinforced laminae have tension moduli up to 40% greater than the compression moduli [1-9]. Other fiber-reinforced composites such as carbon-carbon have tension moduli from two to five times the compression moduli [1-10]. Thus, no clear pattern of larger tension than compression moduli or vice versa exists for fiber-reinforced composite materials. A plausible physical explanation for this puzzling circumstance has yet to be made.

For granular composite materials, the picture is no clearer. ZTA graphite has tension moduli as much as 20% lower than the compression

TABLE 1-1

TENSION AND COMPRESSION MODULI RELATIONSHIPS
FOR SEVERAL COMMON COMPOSITE MATERIALS

MATERIAL	FIBROUS OR GRANULAR	REPRESENTATIVE MODULI RELATIONSHIP
GLASS/EPOXY	FIBROUS	$E_t = 1.2E_c$
BORON/EPOXY	FIBROUS	$E_c = 1.2E_t$
GRAPHITE/EPOXY	FIBROUS	$E_t = 1.4E_c$
CARBON/CARBON	FIBROUS	$E_t = 2\text{-}5E_c$
ZTA GRAPHITE	GRANULAR	$E_c = 1.2E_t$
ATJ-S GRAPHITE	GRANULAR	$E_t = 1.2E_c$

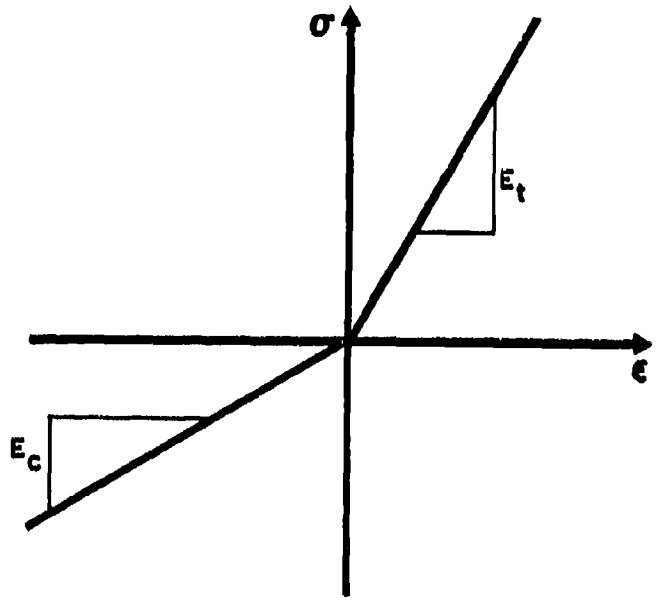

FIGURE 1-4 STRESS-STRAIN CURVE FOR A MATERIAL WITH DIFFERENT MODULI IN TENSION AND COMPRESSION

moduli [1-11]. On the other hand, ATJ-S graphite has tension moduli as much as 20% more than the compression moduli [1-12].

Many other materials have different tension and compression moduli. Which modulus is higher may depend on the fiber or granule stiffness relative to the matrix stiffness. Such a relationship would influence whether the fibers or granules tend to contact and hence stiffen the composite. A general physical explanation of the reasons for different behavior in tension and compression is not yet available. Investigation of the micromechanical behavioral aspects of composite materials may lead to a rational explanation of this phenomenon. Until such an explanation is available, the apparent behavior can be used in analyzing the stress-strain behavior of materials. That is, even without knowing why the materials behave as they do, we can model their apparent behavior.

Actual stress-strain behavior is probably not as simple as shown in Figure 1-4. Instead, a nonlinear transition region may exist between the tension and compression linear portions of the stress-strain [1-13]. The measurement of strains near zero stress is difficult to perform accurately, but the stress-strain behavior might be as shown in Figure 1-5 wherein replacement of the actual behavior by a bilinear model is offered as a simplification of the obviously nonlinear behavior. For most materials, the mechanical property data are insufficient to justify use of a more complex material model. However, one possible disadvantage of the bilinear stress-strain curve approximation is that a discontinuity in slope (modulus) occurs at the origin of the stress-strain curve.

Given that the uniaxial stress-strain behavior is approximated by a bilinear representation, the definition remains of the actual multiaxial stress-strain, or constitutive, relations that are required in structural

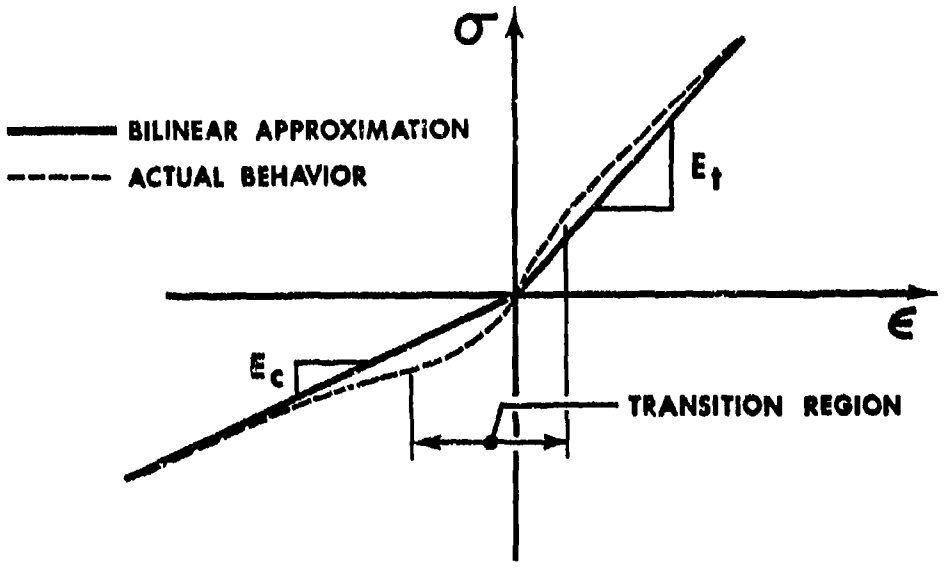

FIGURE 1-5 COMPARISON OF BILINEAR MODEL WITH ACTUAL BEHAVIOR

analysis. Over the past ten years, Ambartsumyan and his co-workers [1-14 thru 1-17], in the process of obtaining solutions for stress analysis of shells and bodies of revolution, defined a set of stress-strain relations that will be referred to herein as the Ambartsumyan material model. Jones [1-18] applied the model to the problem of buckling under biaxial loading of circular cylindrical shells made of an isotropic material. However, in application of the Ambartsumyan material model to orthotropic materials, certain deficiencies, such as a nonsymmetric compliance matrix in the stress-strain relations [1-19], are apparent.

Jones [1-20] also applied modified bilinear stress-strain relations to buckling of shells with multiple layers of orthotropic materials having different moduli in tension and compression. His modifications consist of weighting tension and compression compliances according to the

proportions of the principal stresses in order to obtain a symmetric compliance matrix. Isabekian and Khachatryan [1-21] made the Ambartsumyan material model have a symmetric compliance matrix by enforcing certain relations between the material properties. Both Jones' and Isabekian and Khachatryan's relations are used in the modified Jones-Nelson model, but only Jones' weighted compliance matrix material model is used in the present report.

When the different moduli in tension and compression characteristic is combined with the biaxial softening characteristic, the Jones-Nelson material model leads to predicted versus experimental strains shown in Figure 1-6. There, the predicted strains in the mixed tension and compression quadrant are within 3 to 9% of the measured strains at room temperature for the data shown. Similar, but less accurate, results (from 9-12% error) are shown for 2000°F in Figure 1-7. The experimental data in Figure 1-7 are much less accurate than the data in Figure 1-6 because of testing difficulties at elevated temperatures. Thus, the Jones-Nelson graphite material model is validated by favorable comparison with a well-defined set of biaxial experimental data.

1.3 CHARACTERISTICS OF GRAPHITE

Graphites used in reentry vehicle nosetips are macroscopically homogeneous, transversely isotropic, and generally fail in a brittle manner. The typical stress-strain curve shown in Figure 1-8 is nonlinear to failure. A typical initial modulus versus temperature relationship is also shown in Figure 1-8. There, the modulus actually increases from its room temperature value until a temperature of about 3500°F is reached and subsequently decreases to nearly zero as graphite approaches sublimation. In addition, at all temperatures, the axial

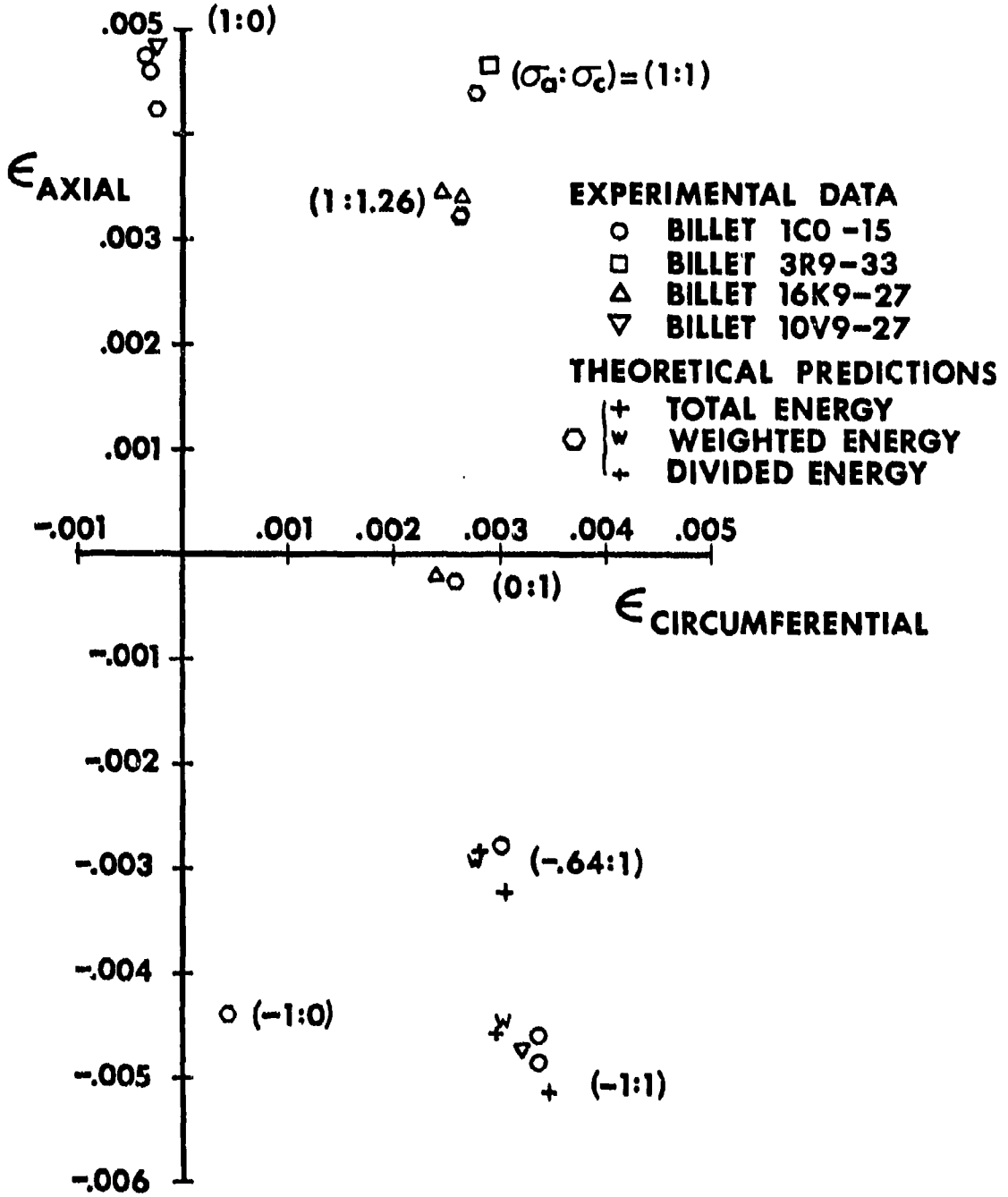

FIGURE 1-6 BIAXIAL RESPONSE OF A HOLLOW ATJ-S GRAPHITE SPECIMEN AT ROOM TEMPERATURE (70°F) AND 3550 psi PRINCIPAL STRESS

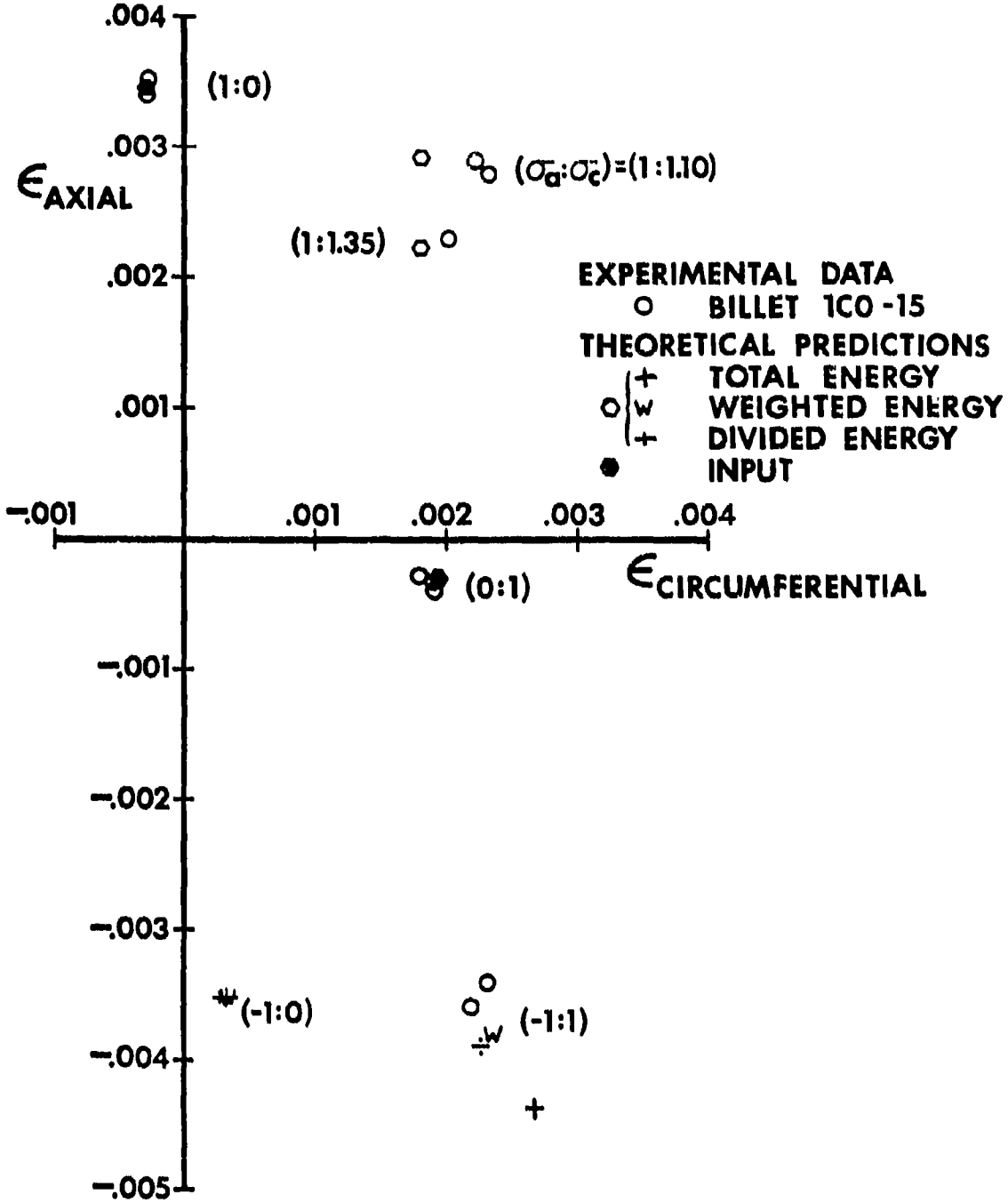

FIGURE 1-7 BIAXIAL RESPONSE OF A HOLLOW ATJ-S GRAPHITE SPECIMEN AT 2000°F AND 3550 psi PRINCIPAL STRESS

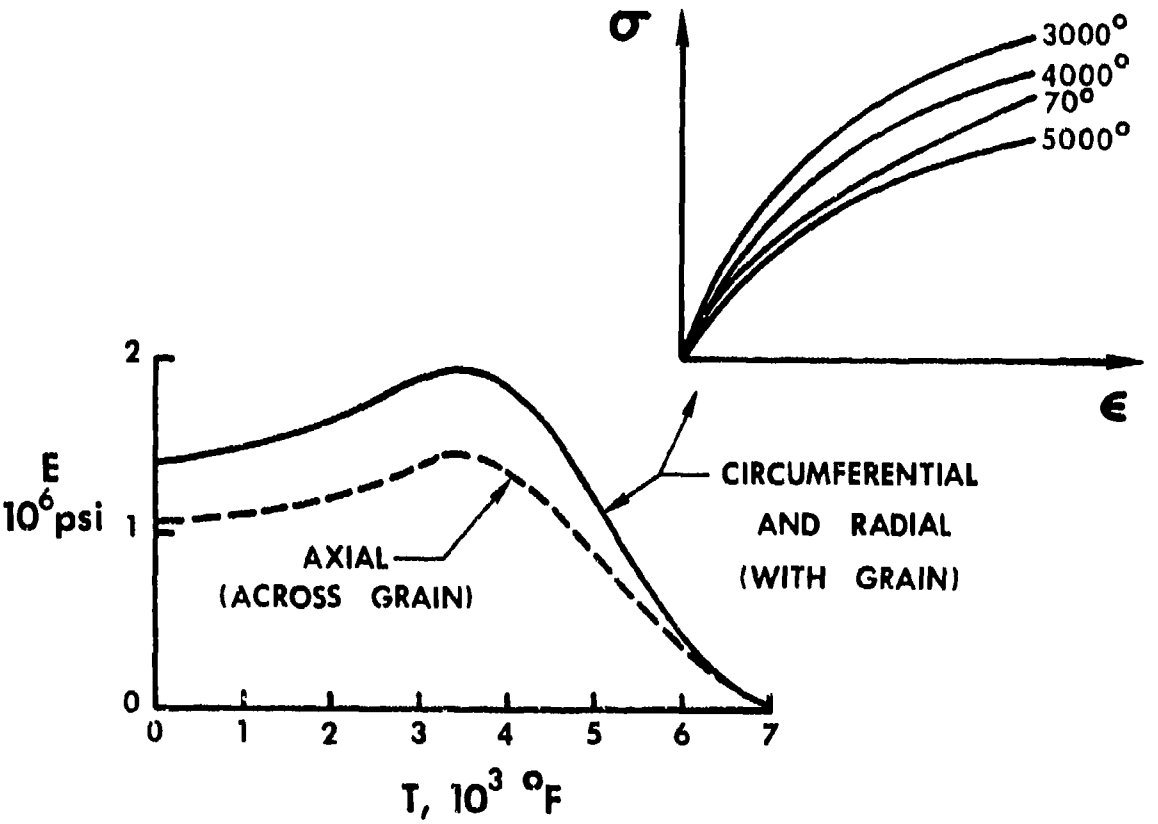

FIGURE 1-8 GRAPHITE BEHAVIOR

modulus is lower than the modulus in the circumferential and radial directions.

Graphite, as mentioned previously, exhibits the biaxial softening phenomenon and has different moduli and stress-strain curves in tension than in compression. These characteristics were successfully modeled by the Principal Investigator in Air Force Contract F33615-73-C-5124. However, the temperature-dependent characteristic has not yet been coupled to the other characteristics nor has an actual nosetip been analyzed.

1.4 CHARACTERISTICS OF CARBON-CARBON

Carbon-carbon materials used in reentry vehicle nosetips are macroscopically inhomogeneous because of large fibers in the axial direction of the nosetip. These materials can be characterized as orthotropic if the fibers are in orthogonal directions, but are anisotropic if fibers at other than 90° angles are inserted. Carbon-carbon fails in a progressive manner as illustrated in Figure 1-9. There, the material is stressed in the direction of axial fibers which apparently slip relative to the matrix material as stress is applied. The initial modulus versus temperature relationship is also shown for the circumferential and radial directions in Figure 1-9. The three curves shown are interpretations of the same experimental data by different people. Thus, considerable disagreement exists as to the actual modulus versus temperature relationship. The axial modulus for this particular carbon-carbon material is about twice the circumferential modulus. Such a relation (quite different from graphite) is not unexpected when the large fibers in the axial direction are considered.

Carbon-carbon, like graphite, exhibits different moduli in tension than in compression; however, the differences are strikingly greater for carbon-carbon than for graphite. No evidence currently exists that carbon-carbons exhibit the biaxial softening phenomenon. Some of the specific mechanical properties of carbon-carbon are given by Legg, Starrett, Sanders, and Pears [1-22].

The most evident difference of carbon-carbon from graphite is its three-dimensional woven character as opposed to the fine-grained structure of graphite. The fibers in carbon-carbon are placed in three mutu-

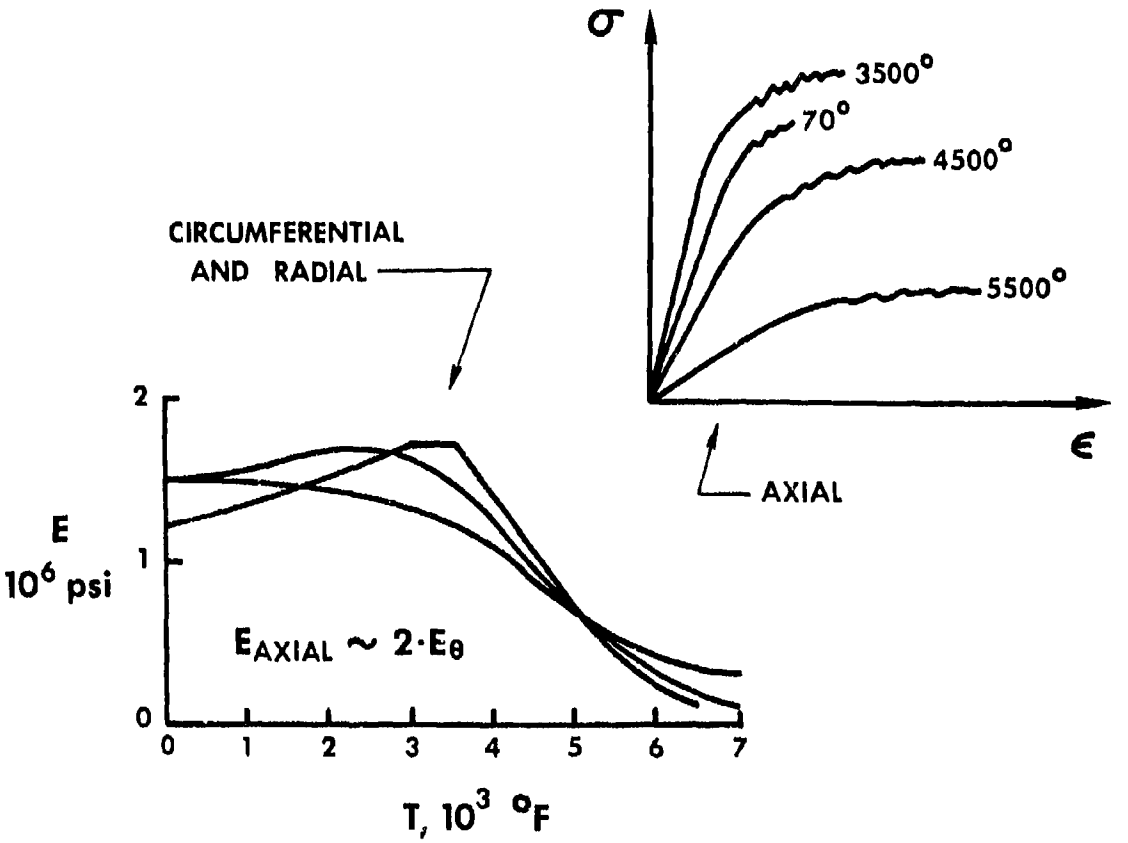

FIGURE 1-9 CARBON-CARBON BEHAVIOR

ally perpendicular directions. Thus, carbon-carbon is a highly orthotropic material in the r-θ plane of a nosetip (as opposed to the isotropy of graphite in this plane). Geiler [1-23] used a linear elastic model in the ASAAS program due to Crose [1-24] to account for the circumferentially varying orthotropy. Geiler obtained apparently good results. However, the ASAAS program would be very difficult to adapt to nonlinear analysis because of the already highly coupled, time consuming internal workings of the computer program.

A related characteristic of carbon-carbon is that the size of the fibers is not negligible in comparison to the size of the billets in which it is manufactured or in comparison to the critical dimensions of the nosetip into which the billets are machined. (Note the Z-direction fibers are the white streaks in the axial direction of the nosetip in Figure 1-10.) Another way of saying the same thing is that the fiber spacing is of the same order of magnitude as the distance over which the

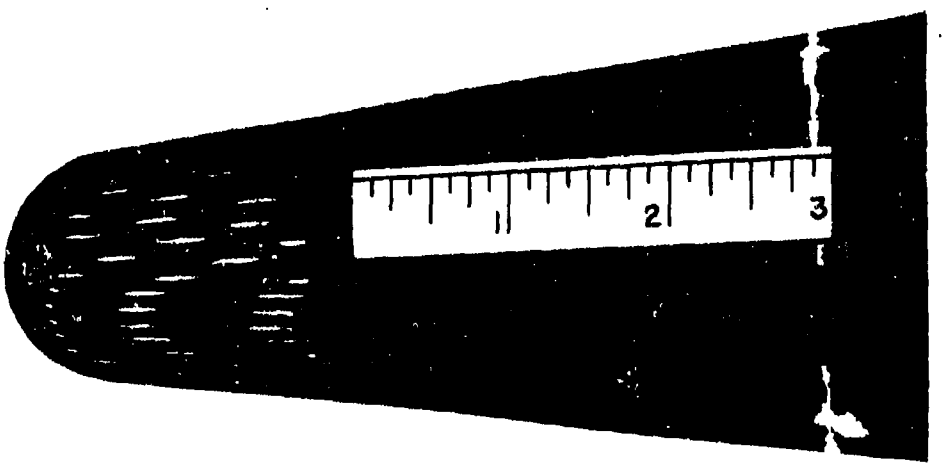

FIGURE 1-10 CARBON-CARBON PLUG NOSETIP

stresses change rapidly. Thus, we would anticipate possible difficulties in applying a macromechanical or continuum mechanics model to carbon-carbon materials. Not enough work has been done, however, to resolve or even clarify the macromechanics versus micromechanics issue.

1.5 STATEMENT OF THE PROBLEM

Two principal efforts are involved in this research: one on graphite material modeling and the other on carbon-carbon material modeling.

The graphite modeling is essentially a continuation of efforts begun under Air Force Contract F33615-73-C-5124. In that contract, graphite multiaxial stress-strain behavior was successfully modeled under both biaxial tension and mixed tension and compression load at room temperature and at 2000°F. The remaining tasks include (1) incorporating a temperature-dependent character in the material model (previously mentioned results are for a constant temperature), (2) validating the model by comparison with further experimental data, and (3) exercising the model in a thermostructural analysis of an actual reentry vehicle nosetip. Upon completion of these tasks, the graphite material model should be ready for routine use in Air Force reentry vehicle nosetip analysis.

The carbon-carbon modeling is a new effort with the objective of applying the basic concepts of the successful graphite model to the analysis of carbon-carbon stress-strain behavior. Generally, carbon-carbon stress-strain curves are more jagged than those of graphite. Thus, some modifications to the graphite model are anticipated. The first step in carbon-carbon modeling is to describe and evaluate the stress-strain curve characteristics. Next, a revised model will be formulated based on these characteristics and on discussions with researchers who have been dealing with carbon-carbon for some time (at Southern Research

Institute, McDonnell-Douglas, AFML, SAMSO, Prototype Development Associates, and Weiler Research, Inc.). The model will then be correlated with available experimental data in a validation stage. If the model does, or can be refined enough to, give good correlation with experimental data, then the model will be evaluated for implementation in AFML and SAMSO nosetip thermostructural analysis computer programs.

1.6 STATEMENT OF RESEARCH

The present research is divided in two major phases, graphite and carbon-carbon, each of which are further divided as follows:

Phase G - Graphite

- G-I - Model Formulation
- G-II - Correlation
- G-III - Nosetip Demonstration
- G-IV - Implementation
- G-V - Reporting

Phase C - Carbon-Carbon

- C-I - Data Evaluation
- C-II - Model Formulation
- C-III - Correlation
- C-IV - Implementation
- C-V - Reporting

These phases are described in the following paragraphs.

1.6.1 PHASE G - GRAPHITE

Phase G-I - Model Formulation

The graphite material model has but one essential characteristic to be incorporated prior to use in actual nosetip analysis. That charac-

teristic is temperature-dependent material behavior. A new scheme must be devised to express the material model as a function of temperature based on data at a finite number of temperatures. Basically, the objective is a material property versus temperature interpolation scheme. However, this scheme is complicated by the presence of many more material property characterization constants in the present model than in previous models for which such interpolation is well-known.

Phase G-II - Correlation

The graphite material model will continue to be correlated with available experimental data. All known biaxial data generated on constant temperature tube specimens by Jortner of McDonnell-Douglas has been successfully correlated. The next logical step is to attempt correlation with data on specimens with a nonconstant temperature, i.e., a temperature gradient. The data for the wedge-shaped disc shown in Figure 1-11 generated in the Temperature/Stress Test developed by Southern

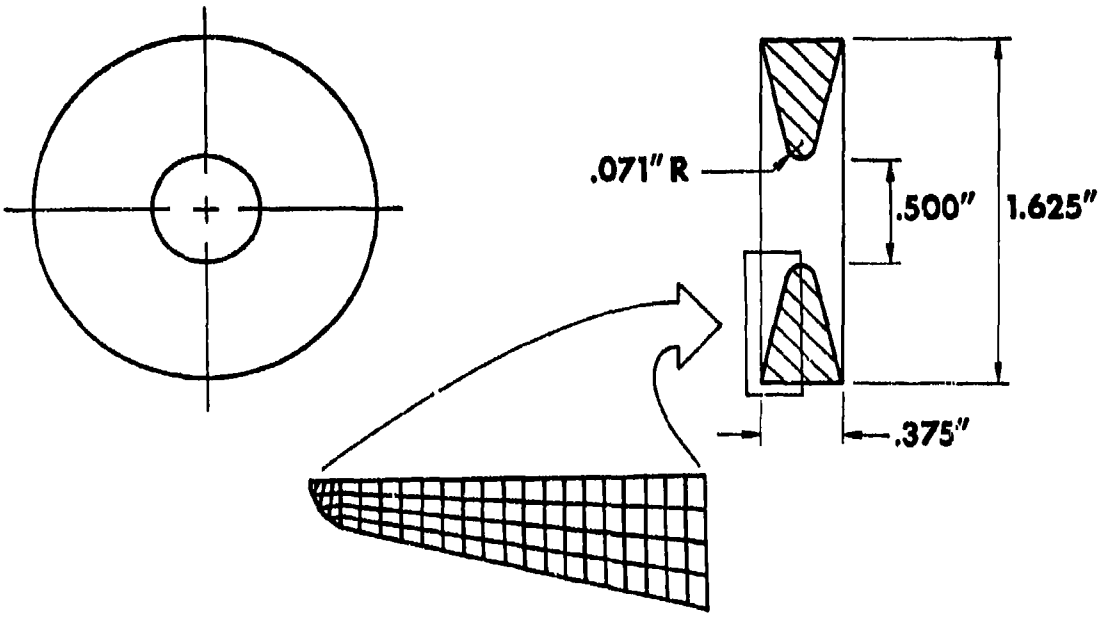

FIGURE 1-11 WEDGE-SHAPED DISK SPECIMEN

Research Institute [1-25] is most appropriate. Limited correlation studies will be performed with that data. Calculated temperature profilges (verified by measurement) through the disc will be used in conjunction with the temperature-dependent material model to predict disc diameter changes. These predictions will be compared with Southern Research Institute measurements to further validate the material model.

Phase G-III - Nosetip Demonstration

The final stage in the development of the material model is to exercise the model in thermostructural analysis of a reentry vehicle nosetip. Although "experimental" data are limited (obviously only flight tests with limited instrumentation can be considered experiments in the present context), the comparison of predictions of the present model with previously used models is essential. Without such comparisons, the real worth of the present graphite material model for reentry vehicle nosetip stress analysis cannot be established.

The finite element data cards for the nosetip and its thermal (and mechanical) loading will be chosen by AFML and supplied to Southern Methodist University in the SAAS III format. These data cards shall have been previously verified to work on SAAS III by another contractor for an all-elastic analysis or an elastic-plastic bilinear analysis. Accordingly, the nosetip demonstration will involve a single variable, the material model. All other variables will be provided to SMU in ready-to-run form.

Phase G-IV - Implementation

The graphite material model developed and validated in previous phases and in Air Force Contract F33615-73-C-5124 will be incorporated in a version of the SAAS III computer program [1-26]. That program is

the basic finite element computer program operational at Southern Methodist University. Duplicate computer decks, listings, test cases, and output will be provided to AFML should an operational deck be desired. In view of Southern Methodist University's mission of graduate education and research, limited manpower, and small computer, the graphite material model will not be implemented in any program other than SAAS III.

Phase G-V - Reporting

The graphite material modeling efforts, correlation studies, and nosetip analysis are described in the present Technical Report.

1.6.2 PHASE C - CARBON-CARBON

Phase C-I - Data Evaluation

Carbon-carbon materials have many different manufacturing processes and hence many different characteristics, as alluded to earlier. The objective of the data evaluation phase is to examine the available material property data and isolate the significant characteristics that must be modeled to accurately predict thermostructural response. This objective will be met by review of published data, review of published material modeling efforts, and consultation with AFML, SAMSO, Southern Research Institute, McDonnell-Douglas, Prototype Development Associates, and Weiler Research, Inc. The latter consultation should take place both in this phase and in subsequent phases. Because of this consultation and the expectation that important material properties will likely be found to not have been measured, data evaluation will be regarded as a phase continuing throughout the remainder of the program.

Phase C-II - Model Formulation

The basic material model used for graphite and described in Reference

1-7 will be fit to the thermostructural characteristics of carbon-carbon. Should a more complicated relationship be necessary, studies will be initiated to determine an appropriate relationship.

The behavior of carbon-carbon will be studied in this initial effort from the standpoint of the axisymmetric macromechanics or continuum mechanics analysis in SAAS III [1-26]. In addition to the basic SAAS III analysis with the new material model, an essentially one-element model with the new material model will be used in modeling feasibility studies such as were carried out in Air Force Contract F33615-73-C-5124. Neither the asymmetric linear elastic analysis of ASAAS [1-24] nor micromechanical analyses will be attempted. Evaluation of the need for and benefit from more geometrically sophisticated models will be made in conjunction with the data evaluation phase. That is, we must be certain the quality and sophistication of the data merit the increased expense of, e.g., asymmetric micromechanical analyses.

Carbon-carbon will be modeled in uniaxial on-axis and off-axis stress states for which material property data exist. Moreover, limited biaxial stress state data will also be modeled to the level of sophistication possible within the scope of two-dimensional or axisymmetric macromechanics theory.

Phase C-III - Correlation

The material model developed in the previous phase will be used to obtain stress-strain predictions for situations in which carefully obtained experimental results are available. These experimental data will be selected in cooperation with AFML. These experiments will include uniaxial on-axis and off-axis tests, the most logical starting point for any material modeling effort. In this manner, the material model will

either be validated by comparison with experimental data or will be invalidated and improvements will be made.

Phase C-IV - Implementation

The carbon-carbon material model developed and validated in previous phases will be incorporated in a version of the SAAS III computer program [1-26]. That program is the basic finite element computer program operational at Southern Methodist University. This research program is not likely to advance the state of the art of carbon-carbon modeling to the point where the model is judged completely ready for widespread Air Force use in reentry vehicle nosetip stress analysis. Instead, the present effort is best described as a bold step toward that goal with some hope of a reasonable model being obtained within the next year. Southern Methodist University expects that further work on carbon-carbon modeling will be necessary before the real question of implementation of the carbon-carbon model in Air Force computer programs arises.

Phase C-V - Reporting

The carbon-carbon material modeling studies, including data evaluation and characterization, model formulation, and correlation activities, are described in the present report.

1.7 SCOPE OF REPORT

The actual accomplishments during the contract are presented in the following sections. First, the Jones-Nelson nonlinear material model is reviewed in Section 2. Also, that model is extended to temperature-dependent material behavior and to treatment of extrapolated stress-strain curves in what is called the Jones-Nelson-Morgan model. Then in Section 3, the graphite modeling efforts are described. First, the correlation

studies for the Southern Research Institute thermal stress disk test are discussed. Then, the AFFDL 50 MW nosetip correlation studies are described. The carbon-carbon modeling efforts are discussed in Section 4. The general modeling is first described and then a characteristic of carbon-carbon in bending tests is treated. The current contract efforts are summarized in Section 5.

2. JONES-NELSON-MORGAN NONLINEAR MATERIAL MODEL

2.1 INTRODUCTION

First, the basic Jones-Nelson nonlinear material model is briefly reviewed in Section 2.2, and some new aspects of its behavior are described. In particular, procedures are developed for temperature interpolation of temperature-dependent material behavior. Then, methods of extending the range of applicability of the material model are discussed in Section 2.3. The major accomplishment in that section is the development of an extended stress-strain curve version of the Jones-Nelson model which is called the Jones-Nelson-Morgan nonlinear material model. Finally, the JNMDATA computer program is described in Section 2.4. This program is used to convert the various measured stress-strain curve data directly to the parameters of the Jones-Nelson and Jones-Nelson-Morgan material models suitable for use in the SAAS IIIM finite element stress analysis computer program which is a modification of the SAAS III program [2-1]. The JNMDATA program is a very useful aid in the modeling of a material because the results are obtained automatically and are presented visually for rapid evaluation of the model.

2.2 JONES-NELSON NONLINEAR MATERIAL MODEL

The Jones-Nelson nonlinear material model was developed under USAF Contract F33615-73-C-5124 and reported in AFML-TR-74-259 [2-2]. Several other related and more accessible publications are condensed from Ref. 2-2, namely Refs. 2-3 thru 2-6. That work will be summarized in Section 2.2.1 for the sake of convenience in reading this report. The necessary further details will be referenced where required. Then, a new discussion of how to implement the model is presented in Section 2.2.2. There,

the recent experience in application of the model is reflected. Finally, the model is extended in Section 2.2.3 to interpolation of temperature-dependent material behavior at temperatures between available data.

2.2.1 BASIC APPROACH

The basic problem is the stress analysis of nonlinear elastic bodies whose stress-strain behavior is described with, for the example of an orthotropic axisymmetric body under axisymmetric load, the equations:

$$\begin{Bmatrix} \varepsilon_r \\ \varepsilon_z \\ \varepsilon_\theta \\ \gamma_{rz} \end{Bmatrix} = \begin{bmatrix} \frac{1}{E_r} & -\frac{\nu_{rz}}{E_r} & -\frac{\nu_{r\theta}}{E_r} & 0 \\ -\frac{\nu_{rz}}{E_r} & \frac{1}{E_z} & -\frac{\nu_{z\theta}}{E_z} & 0 \\ \frac{\nu_{r\theta}}{E_r} & -\frac{\nu_{r\theta}}{E_z} & \frac{1}{E_\theta} & 0 \\ 0 & 0 & 0 & \frac{1}{G_{rz}} \end{bmatrix} \begin{Bmatrix} \sigma_r \\ \sigma_z \\ \sigma_\theta \\ \tau_{rz} \end{Bmatrix} \tag{2.1}$$

where the directions denoted with the subscripts r, z, and θ are principal material directions. The material properties in the compliance matrix of Eq. (2.1) are

E_r = Young's modulus in the r direction

E_z = Young's modulus in the z direction

E_θ = Young's modulus in the θ direction

$\nu_{rz} = -\varepsilon_z/\varepsilon_r$ for the loading $\sigma_r = \sigma$ (all other stresses zero)

$\nu_{r\theta} = -\varepsilon_\theta/\varepsilon_r$ for the loading $\sigma_r = \sigma$ (all other stresses zero)

$\nu_{z\theta} = -\varepsilon_\theta/\varepsilon_z$ for the loading $\sigma_z = \sigma$ (all other stresses zero)

G_{rz} = Shear modulus in the rz plane

The reciprocal relations of orthotropic elasticity

$$\nu_{rz}/E_r = \nu_{zr}/E_z \qquad \nu_{r\theta}/E_r = \nu_{\theta r}/E_\theta \qquad \nu_{z\theta}/E_z = \nu_{\theta z}/E_\theta \tag{2.2}$$

can be used to express alternative definitions for the Poisson's ratios in terms of the seven independent material properties in Eq. (2.1). The material properties in Eq. (2.1) are a function of stress level because the material is nonlinearly elastic. However, we do not examine the unloading behavior nor any subsequent reloading behavior of the body.

The basic stress analysis problem could be more complicated than is represented with Eq. (2.1). For example, the material could have principal material directions at some angle to the r-z-θ coordinate system. Or, the material could have different stress-strain behavior in tension than in compression. The stress-strain relations for multimodulus materials are derived by Jones and Nelson [2-2, 2-5] and are applied to stress analysis of graphitic materials in Ref. 2-6. The foregoing considerations are obviously more complicated than what is represented with Eq. (2.1). However, those equations will suffice for our discussion of the Jones-Nelson material model.

The basic premise of the Jones-Nelson nonlinear material model is that the mechanical properties of a material, e.g., the material properties in Eq. (2.1), are expressed in terms of the strain energy of the body with the approximate equation

$$\text{Mechanical Property}_i = A_i[1 - B_i(U/U_{o_i})^{C_i}] \tag{2.3}$$

where the A_i are the elastic values of the material property, the B_i and C_i are related to the initial curvature and rate of change of curvature, respectively, of the stress-strain curve [2-2, 2-4] (slightly different

interpretations exist when the mechanical property is a Poisson's ratio), and U is the strain energy density of an equivalent elastic system at each stage of nonlinear deformation:

$$U = (\sigma_r\varepsilon_r + \sigma_z\varepsilon_z + \sigma_\theta\varepsilon_\theta + \tau_{rz}\gamma_{rz})/2 \tag{2.4}$$

The strain energy density U is normalized by U_{o_i} in Eq. (2.3) so that B_i and C_i are dimensionless. Typical stress-strain curves, the corresponding mechanical property versus strain energy curves, and the associated mechanical property equations for a Young's modulus and a Poisson's ratio are shown in Fig. 2-1.

The nonlinear stress-strain model is actually much more complicated than Eq. (2.3). When mixed tensile and compressive stresses are excited, the strain energy used in Eq. (2.3) could be a weighted combination of the strain energy of compression and that of tension. Moreover, all coefficients have different values in tension than in compression. The choice of which properties, tension or compression, should be used is made in the Ambartsumyan superposition manner [2-7] after rotating the stress-strain relations to principal stress directions as described in Ref. 2-2.

The stress-strain relations, Eq. (2.1), and the mechanical property versus energy equations, Eq. (2.3), are a set of indeterminate relations which are solved with the iteration procedure shown in Fig. 2-2. That is, the stresses and strains depend on the mechanical properties (through Eq. 2.1) which, in turn, depend on the stresses and strain [through Eqs. (2.3 and (2.4)]. The determination of mechanical properties and, consequently, the stress-strain relationships is based on both the proportions of the principal stresses and on the magnitude of an energy func-

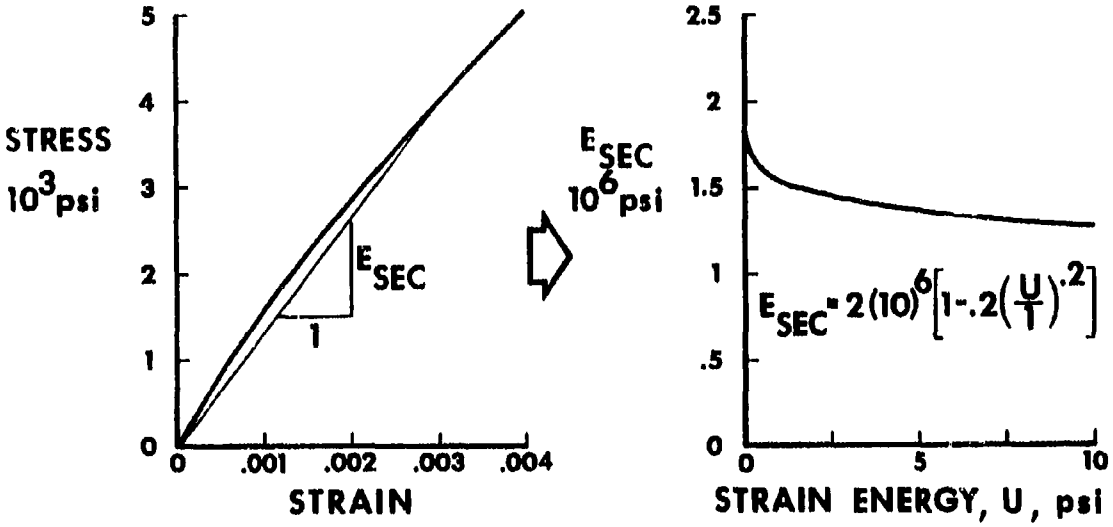

(a) DIRECT MODULUS

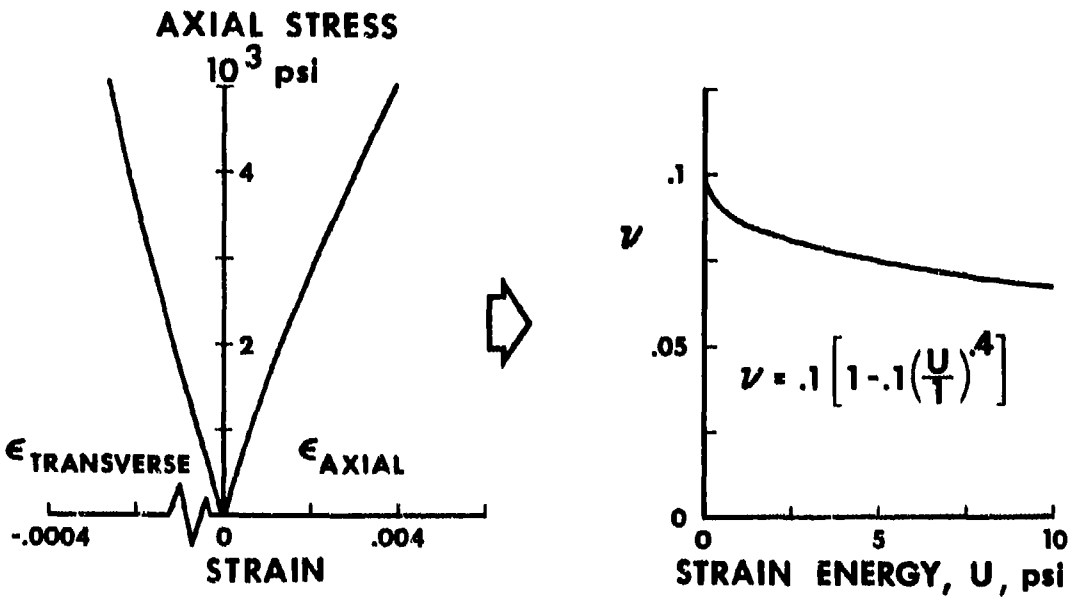

(b) POISSON'S RATIO

FIGURE 2-1 REPRESENTATION OF STRESS-STRAIN RELATIONS FOR DIRECT MODULI AND POISSON'S RATIOS

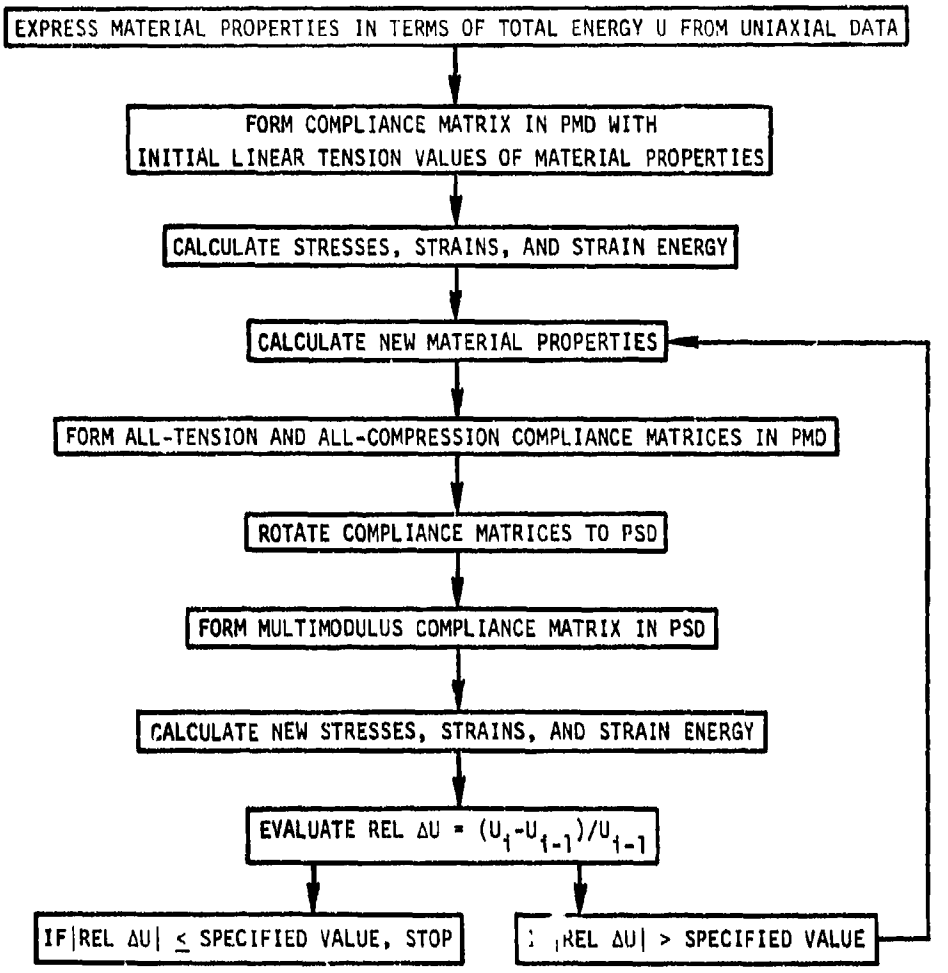

PMD = PRINCIPAL MATERIAL DIRECTIONS

PSD = PRINCIPAL STRESS DIRECTIONS

FIGURE 2-2 ITERATION PROCEDURE FOR NONLINEAR MULTIMODULUS MATERIALS

tion. Each step in the iteration procedure is described in Refs. 2-2 and 2-5.

Two different energy functions - total strain energy and weighted strain energy - can be used in the Jones-Nelson material model. The total strain energy is defined in Eq. (2.4). On the other hand, in the weighted strain energy, the total strain energy is separated into two components: (1) the contribution from the tensile principal stresses and (2) the contribution from the compressive principal stresses. Then, the effective energy level, U_w, in terms of the tension and compression components of the total strain energy is

$$U_w = (U_t^2 + U_c^2)/U \tag{2.5}$$

This energy U_w is used to determine both the tension and compression material properties.

2.2.2 IMPLEMENTATION OF THE MATERIAL MODEL

Much of the work in implementing the Jones-Nelson nonlinear material model is in calculating appropriate values of A, B, and C in the governing equation, Eq. (2.3). To reach the point where these calculations can be made, we must first determine the secant values of the mechanical properties and the corresponding values of strain energy from uniaxial stress-strain curves of the material under investigation. For example, the values of the secant shear modulus and corresponding values of U can be determined from a shear stress - shear strain curve such as shown in Fig. 2-3. There, for two shear stress levels, the corresponding shear strains are found from the experimentally determined shear stress - shear strain curve. Then, $G_{12_{sec}}$ and U are calculated from

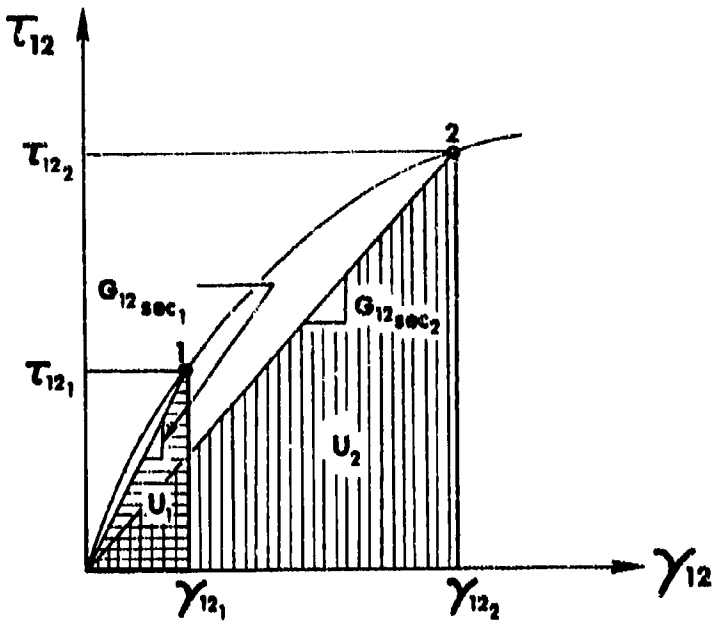

FIGURE 2-3 NONLINEAR SHEAR STRESS - SHEAR STRAIN CURVE

$$G_{12_{sec}} = \frac{\tau_{12}}{\gamma_{12}} \tag{2.6}$$

$$U = \tau_{12}\gamma_{12}/2 \tag{2.7}$$

Similarly, the remaining secant mechanical properties and their corresponding strain energies are found from the appropriate stress-strain curves in principal material directions.

Next, all secant mechanical properties are plotted versus the strain energy as in Fig. 2-4. Now, we can begin to calculate or otherwise find the values of A, B, and C in Eq. (2.3). First, the constant A is the initial (elastic) value of the mechanical property. That is, it is the initial slope of the stress-strain curve in Fig. 2-3 or the intercept of the mechanical property versus energy curve in Fig. 2-4. The value of A is higher than you would expect from the normal procedure of placing a

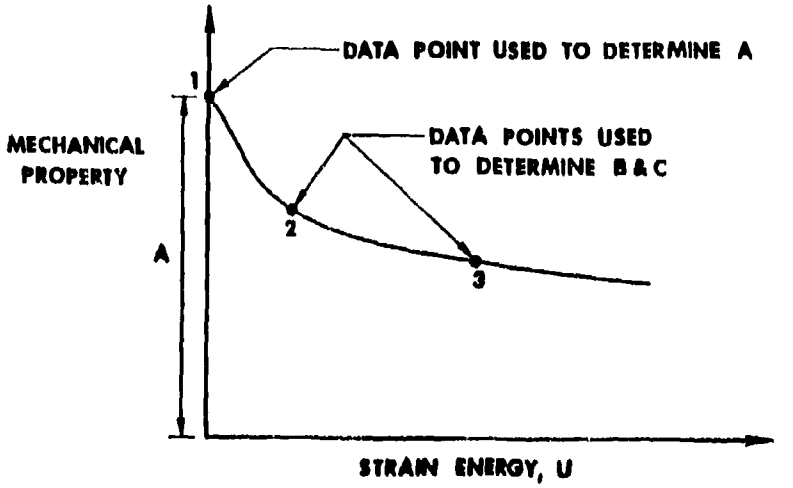

FIGURE 2-4 REPRESENTATIVE MECHANICAL PROPERTY VERSUS U CURVE

straightedge on a stress-strain curve such as Fig. 2-3. We draw this conclusion on the basis of many observed fits of the material model to stress-strain curves with simultaneous fits to a corresponding mechanical property versus energy curve. That is, the curve on a plot of mechanical energy versus energy "heads" for a much higher intercept at U=0 than you would expect from looking at the stress-strain curve alone. This conclusion is not surprising when viewed in the context that the mechanical property is the slope (first derivative) of the stress-strain curve and hence is a more sensitive indicator of the behavior when plotted against energy than when visually determined from a necessarily somewhat inaccurate stress-strain curve.

The constants B and C are determined from data at two points on the material property versus U curve as shown in Fig. 2-4. The values of the mechanical property and the values of U at these two data points are substituted in Eq. (2.3). Two equations in the two unknowns, B and C, result. These two equations are solved simultaneously for B and C to get

$$C = \frac{\log\left[\frac{A-(M.P.)_2}{A-(M.P.)_3}\right]}{\log\left(\frac{U_2}{U_3}\right)} \tag{2.8}$$

$$B = \frac{A-(M.P.)_2}{A}\left(\frac{U_2}{U_o}\right)^{-C} \tag{2.9}$$

where $(M.P.)_2$ and $(M.P.)_3$ are the values of the mechanical property at the two data points chosen from the mechanical property versus U curve. The values U_2 and U_3 in Eqs. (2.8) and (2.9) are the strain energies at the two chosen data points. The proper choice of data points from the mechanical property versus U curve is an important part in the application of the material model to a specific material and will be discussed next.

The use of Eq. (2.3) to approximate each mechanical property corresponds to the mathematical procedure of three-point interpolation. At the three data points used in determining A, B, and C, the approximate values of the mechanical property are the same as the actual values. In the region between these three points, Eq. (2.3) is a reasonable approximation of the mechanical property versus strain energy data. Thus, an interval of strain energy for which Eq. (2.3) is a valid representation of the mechanical property is defined by the positions of points 1 and 3 in Fig. 2-4. This interval of strain energy is bounded on the left by U=0, the strain energy at point 1, and on the right by the strain energy at point 3. The approximate mechanical property versus U curve must pass through point 2 so the shape of this curve between points 1 and 3 is determined from the position of point 2. Obviously, more information than

just data to calculate B and C is gained about the mechanical property approximation from the data points 1, 2, and 3 in Fig. 2-4. The functions of these points can be summarized as follows:

(a) Point 1 is used to determine the constant A in Eq. (2.3) and is the left bound of the interval of strain energy for which the approximate mechanical property versus U curve is valid.

(b) Point 3 is used in determining B and C in Eq. (2.3) and is the right bound of the interval of strain-energy for which the approximate mechanical property versus U curve is valid.

(c) Point 2 is also used in determining B and C in Eq. (2.3), and the shape of the approximate mechanical property versus U curve is defined by the position of point 2 in the interval between points 1 and 3.

The choice of data points used to determine B and C is quite important. If B and C are calculated from data at points 2 and 3 on the actual mechanical property versus strain energy curve (solid line) in Fig. 2-5, the dashed-dotted curve labeled 2-3 is the result. This curve is a reasonable representation of the actual data in the interval $0 < U < U_3$ where U_3 is the value of the strain energy at point 3. For strain energies larger than U_3, the "2-3" curve does not and is not supposed to represent the mechanical property versus strain energy behavior accurately. The mechanical property equation is valid over a larger interval of strain energy if a point further out than point 3 on the actual mechanical property versus U curve is used in the calculation of B and C. For example, when point 4 is used in determining B and C, Eq. (2.3) is valid in the interval $0 < U < U_4$ where U_4 is the value of the strain energy at point 4. Both the "2-4" curve (B and C determined from data at points

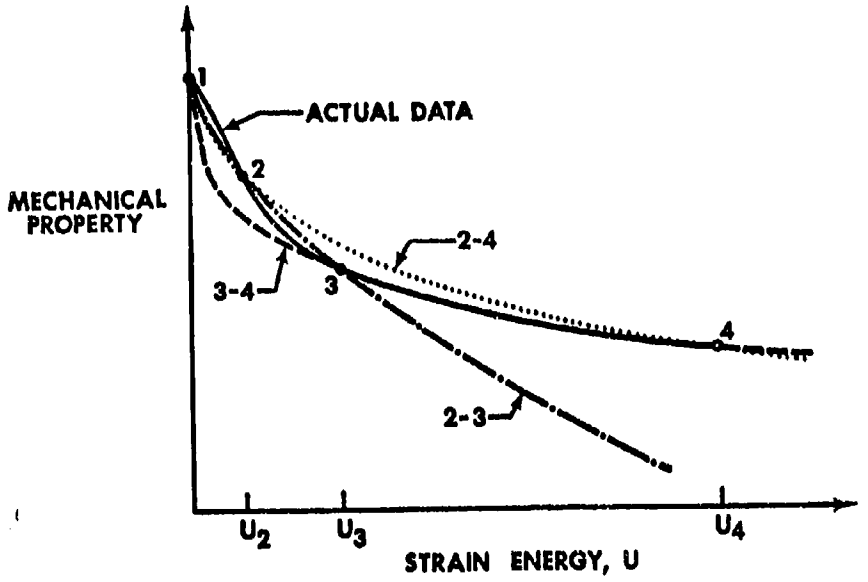

FIGURE 2-5 REPRESENTATIVE MECHANICAL PROPERTY VERSUS U BEHAVIOR AND POSSIBLE APPROXIMATIONS

2 and 4) and the "3-4" curve (B and C determined from data at points 3 and 4) in Fig. 2-5 are reasonable approximations of the actual mechanical property versus strain energy data for $0 < U < U_4$. However, in the interval $0 < U < U_3$ neither the "2-4" nor the "3-4" curve are as good a representation of the actual data as the "2-3" curve. Thus, the mechanical property equation is valid over a large interval of strain energy when point 4 is used in finding B and C, but the accuracy of the approximation in smaller subintervals of the overall interval is sacrificed.

Although the "2-4" and "3-4" curves are valid over the same interval of strain energy, the two curves have different shapes in the interval because different combinations of data points are used in determining B and C. The "2-4" curve must pass through point 2 whereas the "3-4" curve must pass through point 3. (Both curves must pass through points 1 and

4.) Because the mechanical property at point 3 is less than the mechanical property at point 2 and because U_3 is greater than U_2, the "3-4" curve is steeper than the "2-4" curve for $U < U_2$ and flatter for $U > U_3$. In the interval $U_2 < U < U_3$ the two curves have basically the same shape. As a result, the "2-4" curve is a better approximation in the interval $0 < U < U_2$ and the "3-4" curve is a better approximation in the interval $U_3 < U < U_4$. Obviously, in the interval $U_2 < U < U_3$, both approximations are about equally good; the "2-4" approximation is better for the strain energies nearer U_2, and the "3-4" approximation is better for the strain energies nearer U_3. The interval $U_3 < U < U_4$ in Fig. 2-5 is larger than the interval $0 < U < U_2$ so the "3-4" approximation is better than the "2-4" approximation over a large portion of the overall interval of validity $0 < U < U_4$. Thus, the interior data point used to determine B and C should be chosen so that the approximate mechanical property versus U curve takes on the shape desired by the user of the material model and represents the actual data accurately over the desired subinterval of the overall range of validity of the approximation.

With the criteria discussed above as a guide, the actual determination of the constants A, B, and C seems quite easy. However, measured stress-strain data and corresponding mechanical property - strain energy data are somewhat random by nature and do not usually plot as smooth curves. When A, B, and C are determined without regard for the random nature of the data, several pitfalls arise which are not obvious at first. These problems can occur if a single set of constants (A, B, and C) for a single mechanical property is calculated by hand or if many sets of constants for many mechanical properties are calculated with the aid of a computer.

The procedure for determining A, B, and C can be quite tedious when performed by hand calculation. The measured stress-strain data must first be converted to mechanical property - strain energy data. Then, a value for the constant A must be determined. By definition, A is the initial elastic value of the mechanical property, but obviously this initial value cannot be determined from the data at the origin of the stress-strain curve ($\sigma/\varepsilon = 0$). Hence, the initial slope of the measured stress-strain curve, i.e., the tangent modulus at the origin of the stress-strain curve, is often used as the value of A. An alternative approach for finding A is to calculate the value of the mechanical property at the data point corresponding to the lowest measurable stress-strain level and then to arbitrarily use this value of the mechanical property as the value of A. Thus, in this approach, a point on the mechanical property versus U curve for which the strain energy is small is translated to the mechanical property axis. One consequence of determining A in this manner is that the value of A is less than the value obtained by using the initial slope of the stress-strain curve. Another consequence is that data at this point cannot be used in the calculation of the constants B and C. After A is found, the actual mechanical property - strain energy data is plotted, and points to be used in determining B and C are chosen. Once B and C are calculated, the approximate mechanical property versus U is plotted to ensure that a reasonable representation of the actual data is obtained.

For materials with more than one stress-strain nonlinearity, the use of hand calculations in determining the constants for each mechanical property is inefficient because of the large amount of time involved. As a result, the procedure for determining A, B, and C should be auto-

mated so that the calculations are performed by a computer and so that the curves are plotted by an associated mechanical plotter. In the JNMDATA computer program written for this purpose, the measured stresses and strains are input data. The corresponding mechanical properties and strain energies are calculated in the program, and the value of the mechanical property at the first input data point is used as the value of A. The user of the program is able to specify which data points, other than the first one, are used in determining the constants B and C. After the constants B and C are calculated, the program is designed so that the actual mechanical property - strain energy data and the approximate mechanical property versus strain energy curve are plotted on the same page. Also, the measured stress-strain data and the stress-strain curve implied from Eq. (2.3) and calculated in the program are plotted in a similar fashion. Checks of the input data are performed in the program as a precautionary measure to avoid the pitfalls which arise in choosing data points to determine B and C. These pitfalls, due mainly to the random nature of the measured stress-strain data, are mentioned briefly in a preceding paragraph and are discussed in detail in the following paragraphs.

One of the pitfalls which arises if B and C are determined from an arbitrarily chosen combination of data points is that the value of the constant C can be indeterminant. If B and C are chosen from data points 2 and 3 in Figure 2-6a, the mechanical property at point 2, $(M.P.)_2$, is greater than A, and the mechanical property at point 3, $(M.P.)_3$, is less than A. As a result, the argument of the logarithm in Eq. (2.8) is negative so C cannot be determined. If a mechanical property versus strain energy curve passed through points 2 and 3 in Fig. 2-6a, the correspond-

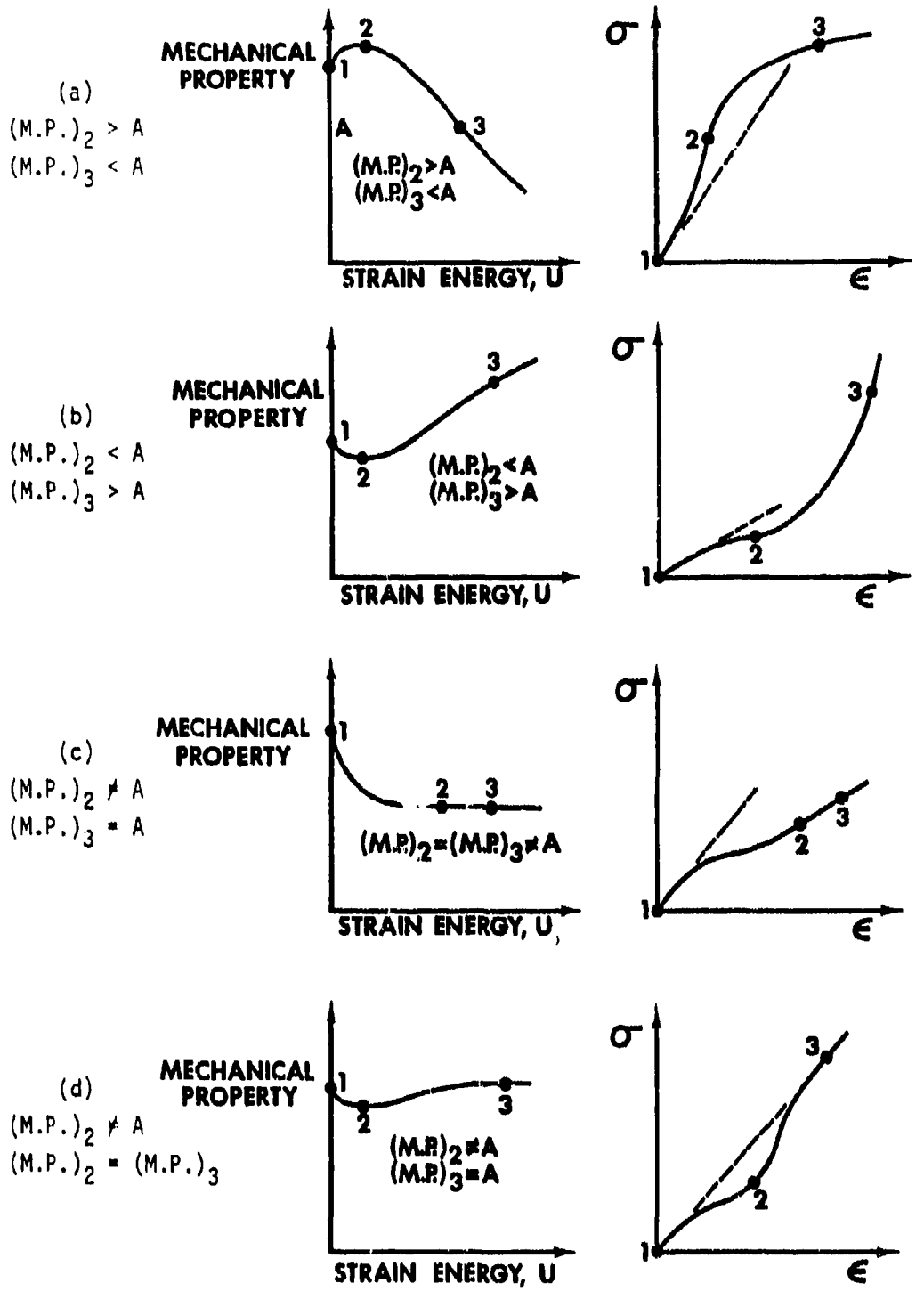

FIGURE 2-6 DATA POINTS WHICH LEAD TO PITFALLS IN CALCULATING B AND C

ing stress-strain curve, also shown in Fig. 2-6a, would be initially concave upward and then would become concave downward. This type of stress-strain behavior is highly unusual and will probably never be encountered. However, measured stress-strain data often has the characteristic that at least one data point is out of line with the rest of the data. If this data point is one of the points used to determine B and C, the situation shown in Fig. 2-6a where $(M.P.)_2$ is greater than A and $(M.P.)_3$ is less than A is encountered. When this situation arises, the process of finding the values of B and C, whether performed by hand or with the aid of a computer, should be stopped and new data points chosen.

The concave downward then concave upward stress-strain behavior in Fig. 2-6b, like the stress-strain behavior in Fig. 2-6a, will probably never be encountered. However, a point at which the mechanical property is less than A, such as point 2 in Fig. 2-6b, and a point at which the mechanical property is greater than A, such as point 3 in Fig. 2-6b, could easily be chosen as the two data points to determine B and C. If two such points are used, the argument of the logarithm in Eq. (2.8) is again negative. The constant C is again indeterminant so the process of calculating B and C should be stopped, and new data points should be chosen.

The initially linear, then nonlinear, and finally linear stress-strain behavior in Fig. 2-6c is also highly unusual but is shown to illustrate a problem which occurs when B and C are determined from another combination of data points. The mechanical property at point 2 in Fig. 2-6c is not equal to A, but the mechanical property at point 3 is equal to A. When these data points are used in finding the values of B and C, the denominator of the argument of the logarithm in Eq. (2.3) is zero so

C cannot be calculated. Thus, this combination of points must be avoided in choosing data points to use in determining B and C.

A different type of problem arises if the mechanical property at point 2 is equal to the mechanical property at point 3 but is not equal to A as in Fig. 2-6d. Because of random measured data, this situation can occur when points 2 and 3 are chosen close to each other. For this combination of data points, the constant C is zero so the approximate mechanical property is not dependent on the strain energy. The value of B is A - $(M.P.)_2$. The approximate mechanical property is a constant but is neither equal to A nor to the mechanical property at point 2 or point 3. That is, the stress-strain behavior in Fig. 2-6d is approximated by a straight line with slope less than A but greater than the value of the mechanical property at point 2 or point 3. Thus, the condition that the approximate mechanical property curve must pass through the three data points used to determine A, B, and C is violated. The unusual stress-strain curve with two linear portions of different slope in Fig. 2-6d cannot be represented exactly. Only an approximation of the behavior, in which the two linear portions are modeled as being nonlinear, can be obtained when Eq. (2.3) is used to approximate the mechanical property. To obtain this mechanical property approximation, point 2 in Fig. 2-6d must be located on the nonlinear portion of the stress-strain curve so that values for B and C can be found.

Pitfalls similar to those discussed above can arise even when common types of stress-strain behavior are modeled if the points used to determine B and C are chosen indiscriminately. The stress-strain behavior of many materials is represented by the initially linear and then nonlinear stress-strain curve in Fig. 2-7a. However, Eq. (2.3) cannot be used to

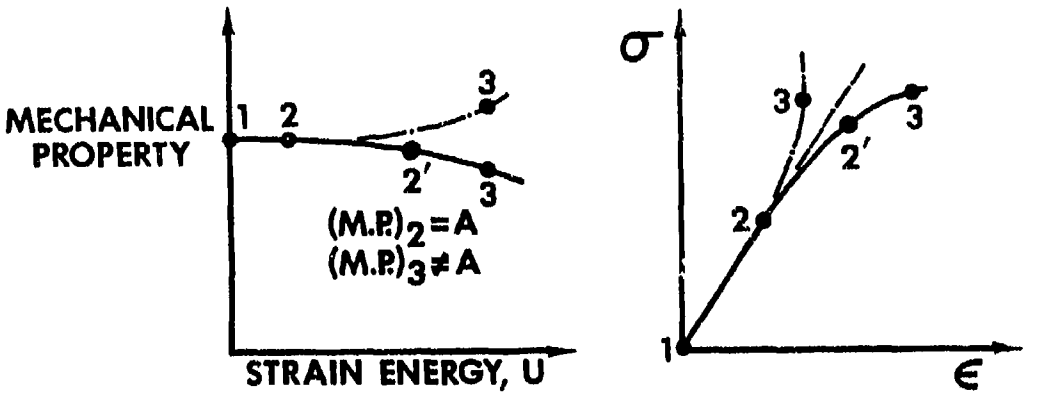

(a) $(M.P.)_2 = A$, $(M.P.)_3 \neq A$

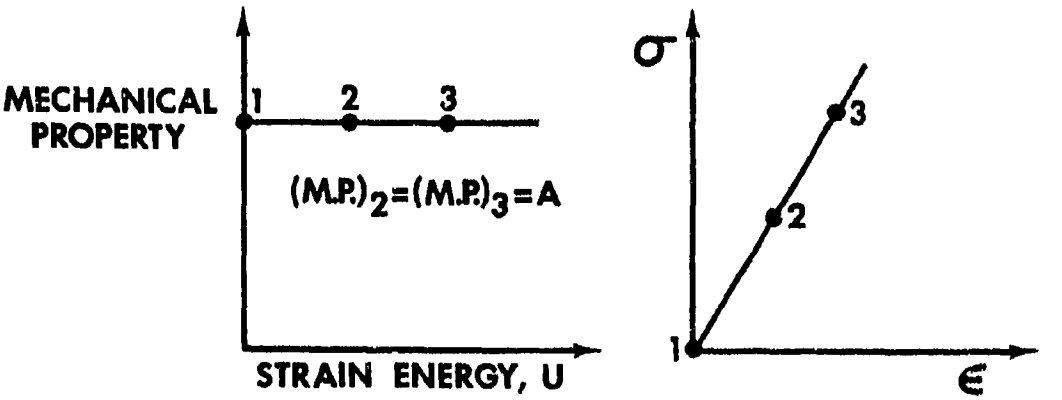

(b) $(M.P.)_2 = (M.P.)_3 = A$

FIGURE 2-7 MECHANICAL PROPERTY VERSUS U BEHAVIORS WHICH CAUSE DIFFICULTIES IN DETERMINING B AND C

approximate the corresponding mechanical property behavior if points 2 and 3 in Fig. 2-7a are used in determining B and C. The mechanical property at point 2 is equal to A but not equal to the mechanical property at point 3. The constant C is indeterminant because the argument of the logarithm in Eq. (2.8) is zero. Hence, the procedure for calculating B and C must be stopped. This problem is avoided by choosing point 2' on the nonlinear portion of the stress-strain curve to be used to determine B and C instead of point 2. The implied stress-strain curve resulting from this approximation is nonlinear at all levels of stress and strain and is a reasonable approximation of the stress-strain curve in Fig. 2-7a, but the measured linear then nonlinear stress-strain behavior cannot be modeled exactly with Eq. (2.3).

Even for linear stress-strain behavior shown in Fig. 2-7b, B and C must be determined carefully. Obviously, the value of the mechanical property at points 2 and 3 in Fig. 2-7b is equal to A, but if B and C are determined with Eq. (2.8) and Eq. (2.9), the argument of the logarithm in Eq. (2.8) is indeterminant (0/0) so C cannot be calculated. However, linear stress-strain behavior is implied from Eq. (2.3) if B is zero and C is finite. Thus, the problem of C being indeterminant is solved by skipping the calculations in Eqs. (2.8) and (2.9) and assigning B the value of zero and C some arbitrary but finite value.

With B and C determined from a proper choice of data points on the mechanical property versus strain energy curve, the mechanical property equation is a valid approximation of the actual mechanical property data over a specfied range of strain energy. However, under many loading conditions, a value of the mechanical property is desired for a strain energy larger than the maximum value of U for which the actual mechani-

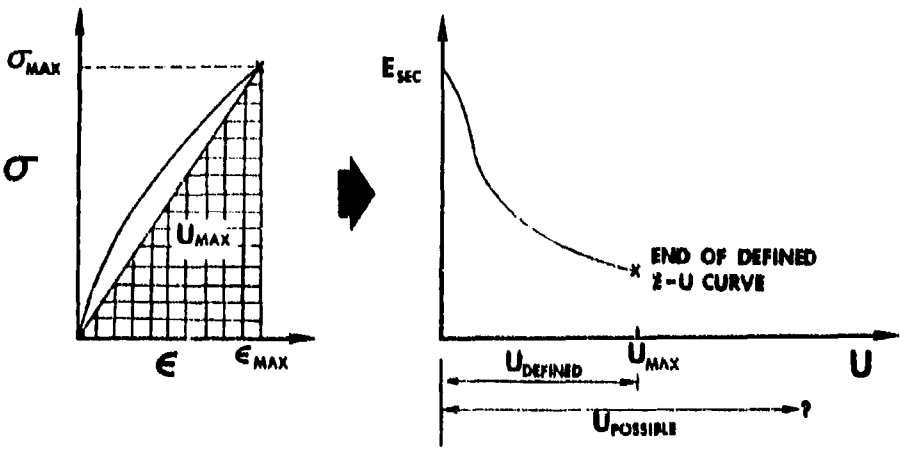

FIGURE 2-8 UNIAXIAL STRESS-STRAIN BEHAVIOR AND CORRESPONDING MATERIAL PROPERTY VERSUS U BEHAVIOR

cal property versus U curve is defined. For example, the mechanical property versus U curve in Fig. 2-8 is defined for strain energies in the range $0 \leq U \leq U_{max}$. This curve is obtained from the uniaxial stress-strain curve also in Fig. 2-8 which is not defined for stresses greater than σ_{max} and strains greater than ϵ_{max}. Hence, E_{sec} is not defined for strain energies greater than $U_{max} = \sigma_{max}\ \epsilon_{max}/2$. A problem arises if a value of the mechanical property is needed for a strain energy greater than U_{max}. Thus, the actual mechanical property versus strain energy curve must be extrapolated in some way. Two extrapolation procedures for the material model are described in Section 2.3.

2.2.3 TEMPERATURE INTERPOLATION OF DEFORMATION BEHAVIOR

Many materials have temperature-dependent deformation behavior. Typically, that deformation behavior is measured at discrete values of temperature over some pertinent range of temperatures. We propose to use such data in finite element stress analysis of bodies subjected to temperature gradients. Then, the basic problem is: given two stress-

strain curves at two temperatures with associated mechanical property versus strain energy curves for which we known A, B, C, and U_o, find the correct property for an intermediate temperature at a specified energy level along with the associated point on the stress-strain curve for the intermediate temperature. Repeated answering of this question for many energy levels would lead us to a mechanical property versus energy curve and a stress-strain curve for the intermediate temperature. These curves must lie appropriately between the respective two original curves for the temperatures between which we interpolated the deformation behavior.

At least three approaches are possible: parameter interpolation, property interpolation, and stress-strain curve interpolation. Each of these approaches is defined and discussed in this section. Moreover, the consequences of using each approach are discussed relative to what is perceived to be the desired result. The word perceived is used because the actual variation of mechanical properties with temperature is often not known except, as stated before, at discrete temperatures. That is, the actual, smooth variation with temperature of properties or stress-strain curves is not known so we have little with which to compare our results.

The basic example for all three approaches will involve the interpolation of ATJ-S graphite properties at 1403°F when we are given the properties at 70°F and 2000°F. We examine only the deformation behavior in the isotropic plane, i.e., σ_θ versus ε_θ and E_θ versus U (or σ_r versus ε_r and E_r versus U). The stress-strain curves are shown for 70°F and 2000°F in Fig. 2-9 and are taken from an SoRI report [2-8]. The boxes in Fig. 2-9 are the SoRI data points and the curves are those obtained

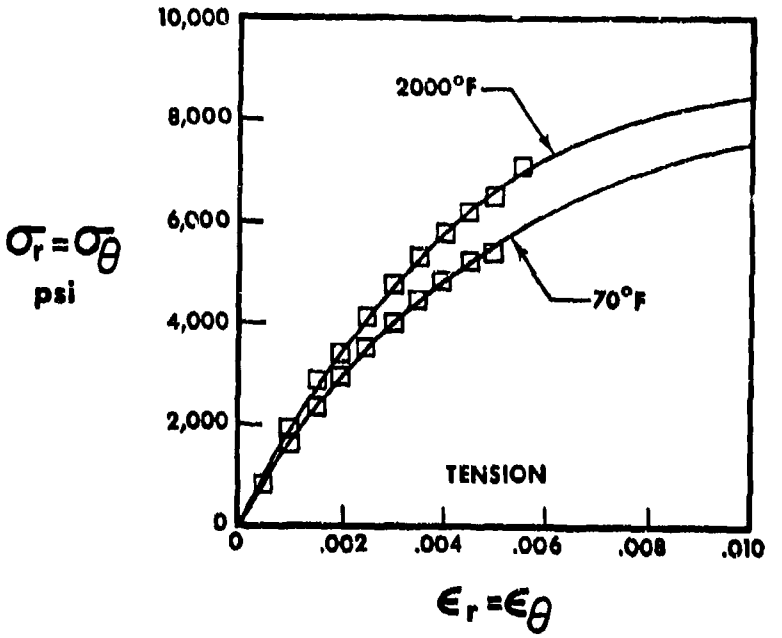

FIGURE 2-9 ATJ-S GRAPHITE STRESS-STRAIN CURVES FOR 70°F AND 2000°F

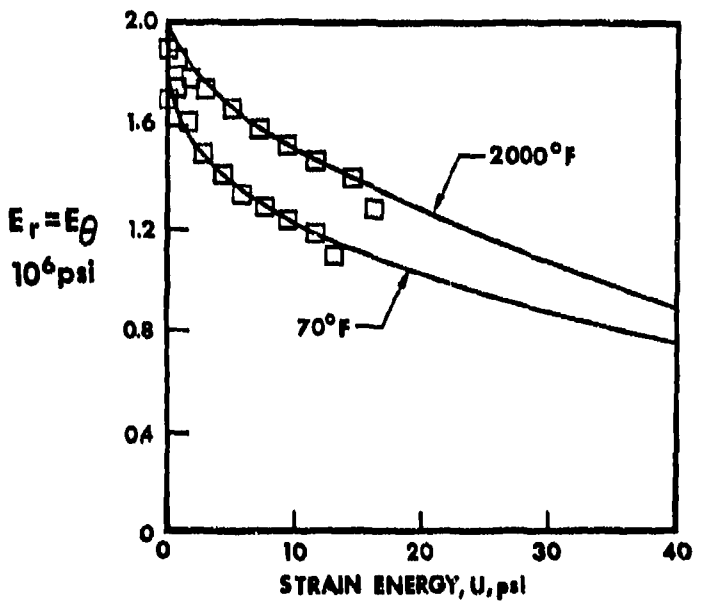

FIGURE 2-10 ATJ-S GRAPHITE MECHANICAL PROPERTY ($E_r = E_\theta$) VERSUS STRAIN ENERGY FOR 70°F AND 2000°F

with the JNMDATA program which will be described in Section 2.4. The associated mechanical property versus strain energy curves are displayed in Fig. 2-10 for which the mechanical property constants in Eq. (2.3) are given in Table 2-1.

TABLE 2-1 ATJ-S GRAPHITE MECHANICAL PROPERTY CONSTANTS FOR $E_r = E_\theta$ VERSUS ENERGY

T	A,psi	B	C	U_o,psi
70°F	2,000,000.	.182	.337	1.
2000°F	2,000,000.	.0651	.583	1.

2.2.3.1 Parameter Interpolation

In parameter interpolation, the values of the parameters (mechanical property constants) A, B, C, and U_o for the intermediate temperature T are found by linear interpolation of the corresponding parameters at the bounding temperatures T_1 and T_2. For example, if $T = (T_1 + T_2)/2$, then

$$A = (A_1 + A_2)/2 \qquad B = (B_1 + B_2)/2$$
$$C = (C_1 + C_2)/2 \qquad U_o = (U_{o_1} + U_{o_2})/2$$

We might expect the resulting mechanical property versus energy and stress-strain curves to lie midway between the respective interpolated curves. However, they do not. In fact, at a temperature of 1403°F for which A = 2,000,000 psi, B = .101, C = .507, and U_o = 1 psi (from linear interpolation), at stresses above 7,000 psi in Fig. 2-11 the resulting stress-strain curve lies <u>below</u> the 70°F curve and <u>not</u> fairly close to the 2000°F curve as we would hope. Moreover, at U = 40 psi, the resulting E_θ is <u>less</u> than E_0 for 70°F. Part of this undesirable result may

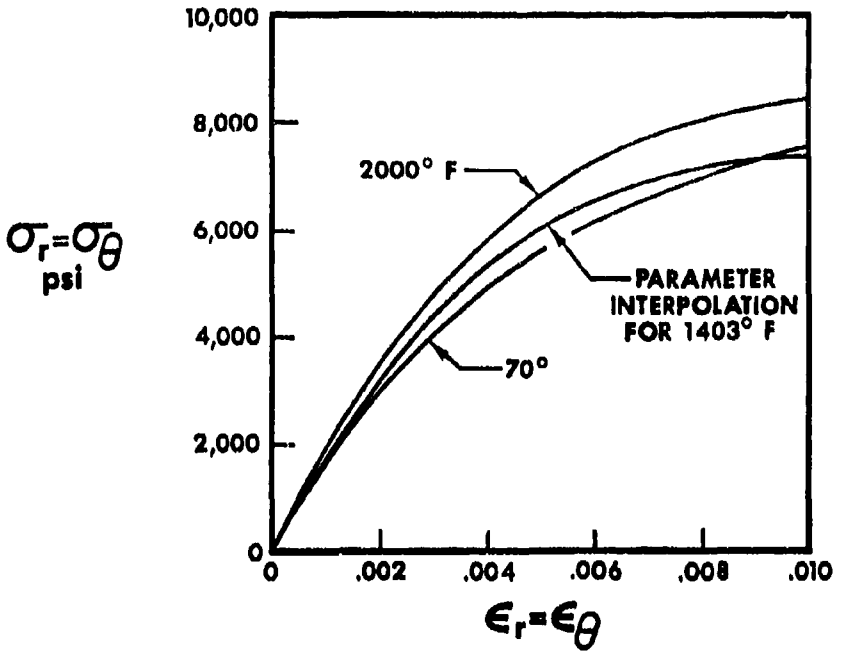

FIGURE 2-11 STRESS-STRAIN CURVE AT 1403°F

FROM PARAMETER INTERPOLATION

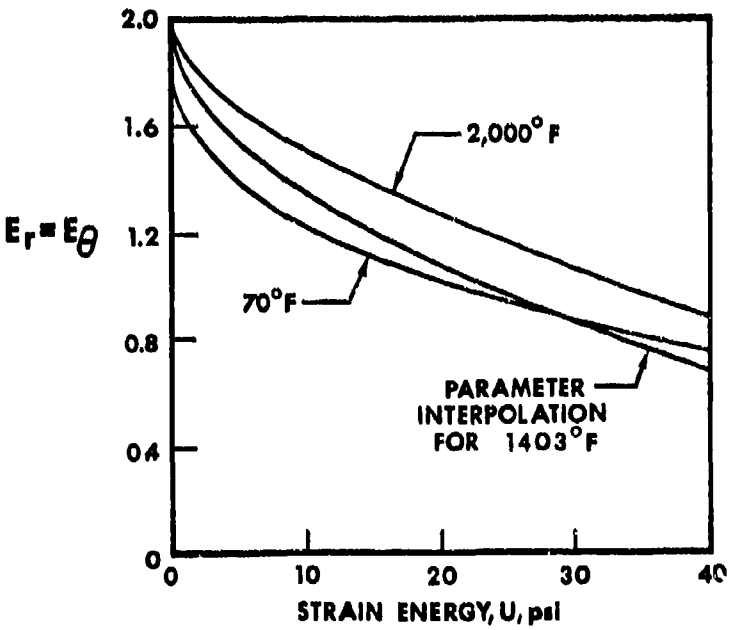

FIGURE 2-12 MECHANICAL PROPERTY VERSUS ENERGY CURVE AT 1403°F

FROM PARAMETER INTERPOLATION

stem from the simultaneously constant A's, decreasing B's, and increasing C's (but not from the constant U_o). At any rate, parameter interpolation is obviously undependable since the resulting interpolated curves may not even lie between the curves being interpolated!

2.2.3.2 Property Interpolation

In property interpolation, the mechanical property for the intermediate temperature T is found by linear interpolation of the mechanical properties at the bounding temperatures T_1 and T_2 for a specified energy level. That is, if for example T lies midway between T_1 and T_2, then

$$\text{Mechanical Property}_T = \frac{1}{2}\left(\text{Mechanical Property}_{T_1} + \text{Mechanical Property}_{T_2}\right) \tag{2.10}$$

The resulting mechanical property versus energy curve lies precisely midway between the two curves being interpolated, by definition. However, the resulting stress-strain curve may be closer to the higher of the two curves being interpolated. When T = 1403°F, the interpolated stress-strain curve in Fig. 2-13 is "about the right distance" from the two curves from which it is indirectly interpolated. Also, the interpolated mechanical property versus energy curve is precisely where it must be when we assume that the mechanical properties are a linear function of temperature between the discrete temperature values at which the mechanical behavior is measured. We delay an appraisal of the value of this method until after the next sub-section on stress-strain curve interpolation.

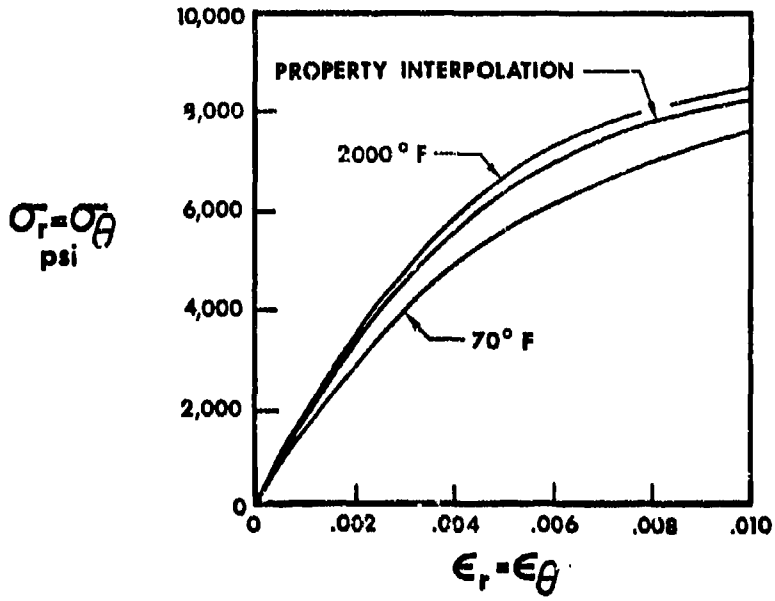

FIGURE 2-13 STRESS-STRAIN CURVE AT 1403°F
FROM PROPERTY INTERPOLATION

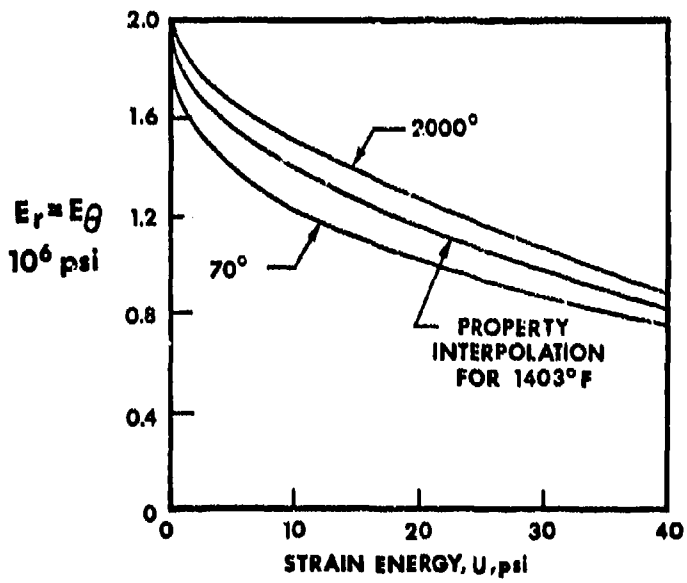

FIGURE 2-14 MECHANICAL PROPERTY VERSUS ENERGY CURVE AT 1403°F
FROM PROPERTY INTERPOLATION

2.3.3.3 STRESS-STRAIN CURVE INTERPOLATION

In stress-strain curve interpolation, the coordinates of points on the interpolated stress-strain curve are found from the information known for the stress-strain curves at the bounding temperatures. Actually, we are assuming that the stress-strain curves vary linearly with temperature between the curves at input discrete temperature levels. For example, the stress-strain curve for a temperature midway between the two temperatures at which the stress-strain curves are prescribed lies, by definition, precisely midway between the two prescribed stress-strain curves. However, since there is no direct equation for the stress-strain curves, we must construct the interpolated stress-strain curve by calculation of stresses and strains for a succession of energy levels.

The calculation procedure is straightforward, but several steps are necessary for each energy level:

(1) Calculate E_1 and E_2 at T_1 and T_2, the bounding temperatures (the 1 and 2 subscripts will be used hereafter in association with T_1 and T_2, respectively).

(2) Calculate the corresponding strains ε_1 and ε_2 by realizing that

$$\sigma_1 = E_1\varepsilon_1$$

$$\sigma_2 = E_2\varepsilon_2$$

but

$$U = \frac{1}{2}\sigma_1\varepsilon_1 = \frac{1}{2}(E_1\varepsilon_1)\varepsilon_1$$

$$U = \frac{1}{2}\sigma_2\varepsilon_2 = \frac{1}{2}(E_2\varepsilon_2)\varepsilon_2$$

so

$$\varepsilon_1 = (2U/E_1)^{1/2}$$

$$\varepsilon_2 = (2U/E_2)^{1/2}$$

(3) Calculate the corresponding stresses σ_1 and σ_2 from

$$\sigma_1 = E_1\varepsilon_1 = (2UE_1)^{1/2}$$

$$\sigma_2 = E_2\varepsilon_2 = (2UE_2)^{1/2}$$

(4) Interpolate (σ_1,ε_1) and (σ_2,ε_2) along a straight line joining them to get (σ_T,ε_T):

$$\sigma_T = \frac{\Delta T}{T_2 - T_1}(\sigma_2 - \sigma_1) + \sigma_1$$

$$\varepsilon_T = \frac{\Delta T}{T_2 - T_1}(\varepsilon_2 - \varepsilon_1) + \varepsilon_1$$

(5) Calculate the mechanical property at T:

$$E_T = \frac{\sigma_T}{\varepsilon_T}$$

The foregoing five steps are repeated for increasing energy levels until the stress-strain and mechanical property versus energy curves are sufficiently well defined.

With this approach, the $\sigma_T - \varepsilon_T$ curve lies midway between the two stress-strain curves if $T = (T_1 + T_2)/2$. Also, the interpolated mechanical property versus energy lies closer to the lower specified curve than to the upper curve. However, for the ATJ-S graphite example at 1403°F, the resulting stress-strain curve is indistinguishable from that obtained with property interpolation in Fig. 2-13 (slight numerical differences exist, but they are not visually detectable at the scale of Fig. 2-13). Moreover, the resulting mechanical property versus energy curve is indistinguishable from that obtained with property interpolation in Fig. 2-14.

2.2.3.4 Summary

Three different approaches to interpolation of deformation behavior

are discussed. One, parameter interpolation, is found to be inaccurate and unreliable. The other two, property interpolation and stress-strain curve interpolation, are found to be equivalent. The two methods are both applied to the case where the temperature is midway between the two input temperatures. Although the interpolated mechanical property versus energy curve is precisely midway between the two input curves for property interpolation, the interpolated stress-strain curve might theoretically be a little too high. On the other hand, the interpolated stress-strain curve is precisely midway between the two input curves for stress-strain curve interpolation, but the interpolated mechanical property versus energy curve might theoretically be a little too low. The two methods are also applied to an actual case for ATJ-S graphite where the temperature is 1403°F and stress-strain data are known at 70°F and 2000°F. In this practical case, the differences between the two interpolation approaches are negligible. That is, property interpolation leads to an interpolated stress-strain curve which is also linearly interpolated between the respective input stress-strain curves. And, stress-strain curve interpolation leads to an interpolated mechanical property versus energy curve which is also linearly interpolated between the respective input mechanical property versus energy curves. Thus, the two approaches are equivalent for practical purposes. The property interpolation approach is used in the SAAS IIIM program and the steps involved in property interpolation are simpler than those for stress-strain curve interpolation.

2.3 EXTRAPOLATION PROCEDURES FOR MATERIAL MODELS

2.3.1 INTRODUCTION

The strain energy can exceed the defined range of the mechanical property versus U curve for two reasons. First, the nonlinear model is applied to materials subjected to multiaxial stress states in which the strain energy is higher than in the uniaxial stress states where the properties are measured. All the stresses and strains of a multiaxial stress state contribute to the value of U, and, thus, the multiaxial strain energy is often larger than the maximum U attainable from a uniaxial stress state. The second reason for the existence of strain energies outside the defined range of the mechanical property versus U curve is that orthotropic materials have drastically different load capacities and hence drastically different strain energy capacities in different directions. The strain energy capacities for loading in the 2-direction and for shear loading are generally much lower than the strain energy capacity for loading in the 1-direction. For example, the representative longitudinal stress - longitudinal strain curve in Fig. 2-15 is associated with strain energies as high as 250 psi. However, the maximum value of U which can be used to define the mechanical property $E_{2_{sec}}$ from the transverse stress - transverse strain curve in Fig. 2-8 is only 40 psi. Thus, strain energies corresponding to some uniaxial loading conditions, such as loading in the 1-direction or off-axis loading, can be much larger than the U_{max} for which $E_{2_{sec}}$ is defined.

The mechanical property versus U curve can be extended past its defined range by the two extrapolation procedures described in this section. The procedure described in Section 2.3.2 consists of using Eq. (2.3) for all values of strain energy including those which exceed the maximum

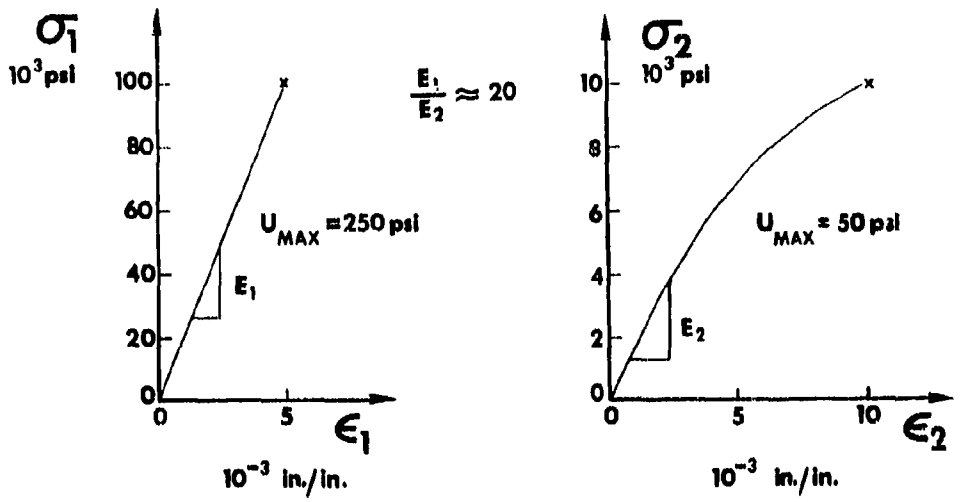

FIGURE 2-15 NORMAL STRESS - NORMAL STRAIN BEHAVIOR OF AN ORTHOTROPIC MATERIAL

strain energy for which the actual mechanical property data are defined. When the extrapolation procedure in Section 2.3.2 fails, the extrapolation procedures described in Section 2.3.3 are used. There, extensions of the defined stress-strain curve are involved as opposed to the direct extension of the mechanical property versus strain energy curve in Section 2.3.2. The stress-strain curve is extended by following the trend of the defined portion of the curve until the slope attains some preassigned value, i.e., until $\frac{d\sigma}{d\varepsilon} = \left(\frac{d\sigma}{d\varepsilon}\right)^*$. For strains larger than ε^*, the strain at which $\frac{d\sigma}{d\varepsilon} = \left(\frac{d\sigma}{d\varepsilon}\right)^*$, the stress-strain curve is extended as a straight line with slope $\left(\frac{d\sigma}{d\varepsilon}\right)^*$ to represent the behavior of ductile fiber-reinforced composite materials. Equation (2.3) is used to represent the mechanical property - U behavior for strain energies corresponding to points on the stress-strain curve to the left of ε^*. Another expression which will be developed in Section 2.3.3 is used to define the mechanical property for strains larger than ε^*.

2.3.2 EXTENDED MECHANICAL PROPERTY VERSUS STRAIN ENERGY CURVE APPROACH

The simplest means of extrapolating the mechanical property versus strain energy curve is to use the mechanical property equation for all values of U including, because of extrapolation, those beyond the defined range of strain energy. A representative mechanical property versus U curve is shown in Fig. 2-16. This curve is defined for strain energies less than or equal to U_{max}. Also shown in Fig. 2-16 is an extended approximate mechanical property versus U curve corresponding to Eq. (2.3). For this curve, B and C are determined from the data point with strain energy equal to U_{max} and another point with strain energy close to U_{max}. This approximate curve is an accurate interpolation of the actual data for strain energies between zero and U_{max} as discussed earlier. In addition, this curve has the same shape as the actual mechanical property versus U curve in the neighborhood of U_{max} and is a reasonable extension of the actual data for strain energies greater than U_{max}. Thus, if data at the point corresponding to $U = U_{max}$ and data at another point near the

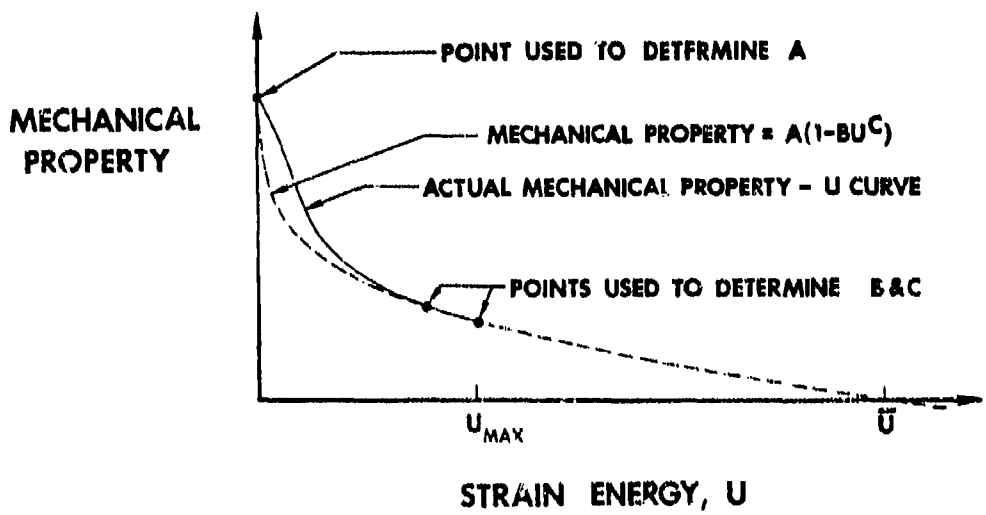

FIGURE 2-16 ACTUAL AND EXTRAPOLATED MECHANICAL PROPERTY VERSUS U BEHAVIOR

limit of the defined mechanical property versus U curve are used to determine the constants B and C, the use of Eq. (2.3) is potentially a valid means of extrapolating the actual mechanical property - U data.

However, the use of Eq. (2.3) as an extrapolation is restricted. At some large value of U, the approximate mechanical property curve in Fig. 2-16 crosses the U-axis, i.e., the extrapolated value of the mechanical property becomes negative. The strain energy at which the mechanical property is zero is designated as $\bar{U}$ in Fig. 2-16. If a mechanical property is less than or equal to zero, a thermodynamic constraint on the mechanical properties of a material is violated. This constraint, imposed on the properties to avoid the creation of energy, is that the work done by the stresses applied to a material must be positive. Lempriere [2-9] interprets this constraint as meaning that both the stiffness and compliance matrices of an orthotropic material must be positive definite. These matrices are positive definite only if the mechanical properties E_1, E_2, and G_{12} are positive. Thus, the mechanical properties of a material cannot be defined with Eq. (2.3) for strain energies greater than or equal to $\bar{U}$. The value of $\bar{U}$ can be determined from Eq. (2.3) and depends only on the constants B and C:

$$\bar{U} = \left(\frac{1}{B}\right)^{\frac{1}{C}} \tag{2.11}$$

For a constant value of B, the value of $\bar{U}$ increases when C decreases.

The stress-strain behavior implied from Eq. (2.3) must be a reasonable extension of the actual stress-strain behavior of the material. For the implied stress-strain curves in Fig. 2-17, the stresses reach a maximum value and then decrease with increasing strain. As the strain in-

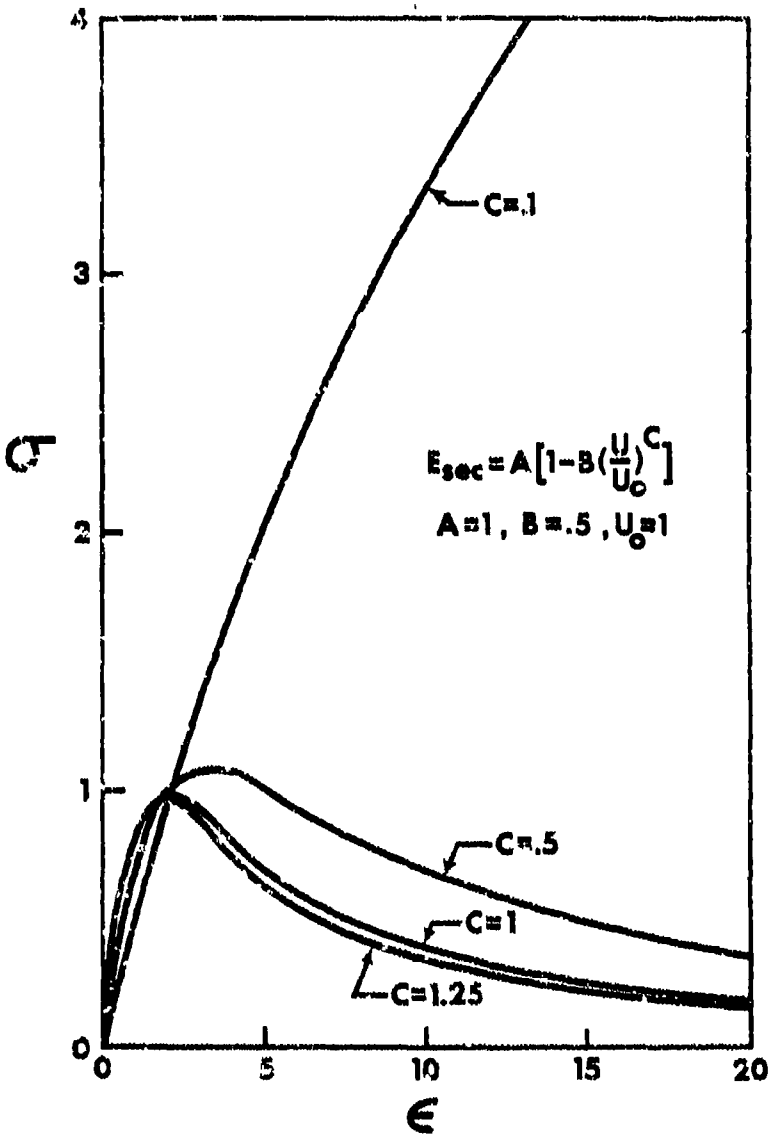

FIGURE 2-17 EXTENDED IMPLIED STRESS-STRAIN CURVES FOR A = 1, B = .5, U_o = 1

creases without bound, the stress approaches zero asymptotically. Also, the strain energies determined from the implied stress-strain curves in Fig. 2-17 approach but never reach the value $\bar{U}$, i.e.,

$$\lim_{\substack{\sigma \to 0 \\ \varepsilon \to \infty}} U = \bar{U} = \left(\frac{1}{B}\right)^{\frac{1}{C}} \tag{2.12}$$

Hence, $\bar{U}$ is the maximum strain energy which can be associated with both the mechanical property equation and its implied stress-strain curve.

The stress-strain curve implied from the mechanical property equation is not necessarily representative of the actual stress-strain behavior of fiber-reinforced materials in the range $0 < U < \bar{U}$. The schematic implied stress-strain curve shown in Fig. 2-18 reaches a maximum at the point $(\tilde{\sigma}, \tilde{\varepsilon})$. The portion of the curve to the left of $(\tilde{\sigma}, \tilde{\varepsilon})$ is representative of actual stress-strain behavior. The implied stress-strain behavior to the right of $(\tilde{\sigma}, \tilde{\varepsilon})$ where the stress decreases as the strain increases has not been observed for fiber-reinforced composite

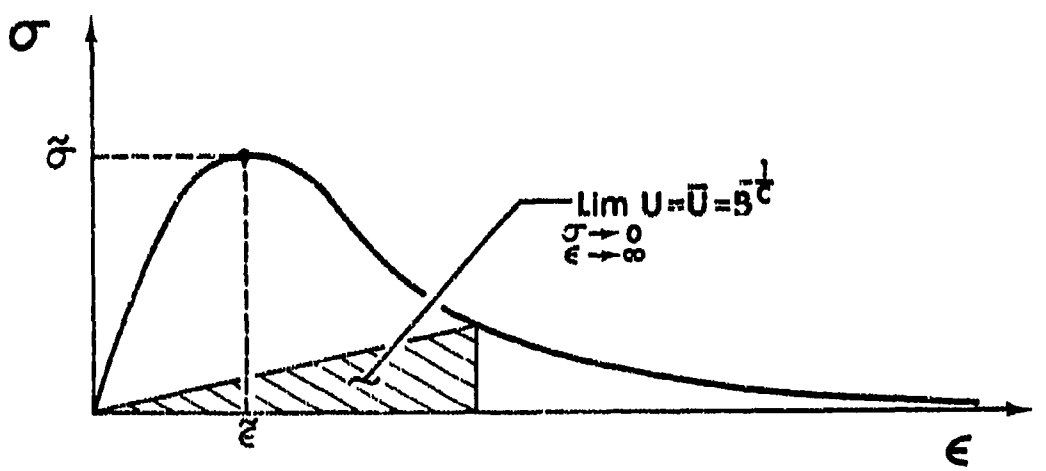

FIGURE 2-18 REPRESENTATIVE IMPLIED STRESS-STRAIN BEHAVIOR CORRESPONDING TO JONES-NELSON EQUATION

materials. Thus, the extended mechanical property versus strain energy curve approach cannot be used as an extrapolation for strain energies as large as $\bar{U}$, but must be restricted to strain energies less than $\tilde{U}$ where

$$\tilde{U} = 1/2\ \tilde{\sigma}\ \tilde{\epsilon} \qquad (\tilde{U} < \bar{U}) \tag{2.13}$$

2.3.3 EXTENDED STRESS-STRAIN CURVE APPROACH

An extension of the mechanical property versus strain energy curve by the use of the mechanical property equation is indirectly an extension of the actual stress-strain curve; i.e., the measured stress-strain curve is extended past its defined range with an implied stress-strain curve similar to the one in Fig. 2-18. However, for strain energies greater than $\tilde{U}$, the stress-strain behavior must be extrapolated with some procedure other than the extended mechanical property versus strain energy curve approach. A reasonable extrapolation is to extend the measured stress-strain curve directly, then convert the extrapolated stress-strain data into extrapolated mechanical property versus strain energy data, and finally develop an expression for the extrapolated mechanical property data in terms of the strain energy. Several extensions of the stress-strain data are discussed in this section. Linear extensions of the stress-strain behavior with zero slope and with nonzero slope are discussed in Section 2.3.3.1 and 2.3.3.2, respectively.

2.3.3.1 Linear Stress-Strain Curve Extensions with Zero Slope

One linear extension of the defined stress-strain curve involves estimating the stress level at which the nonlinear curve has zero slope. The stress-strain curve in Fig. 2-19a is defined up to point P. The trend of the defined stress-strain curve is followed, and the curve is arbitrarily extended until the slope becomes zero at point Q. The stress

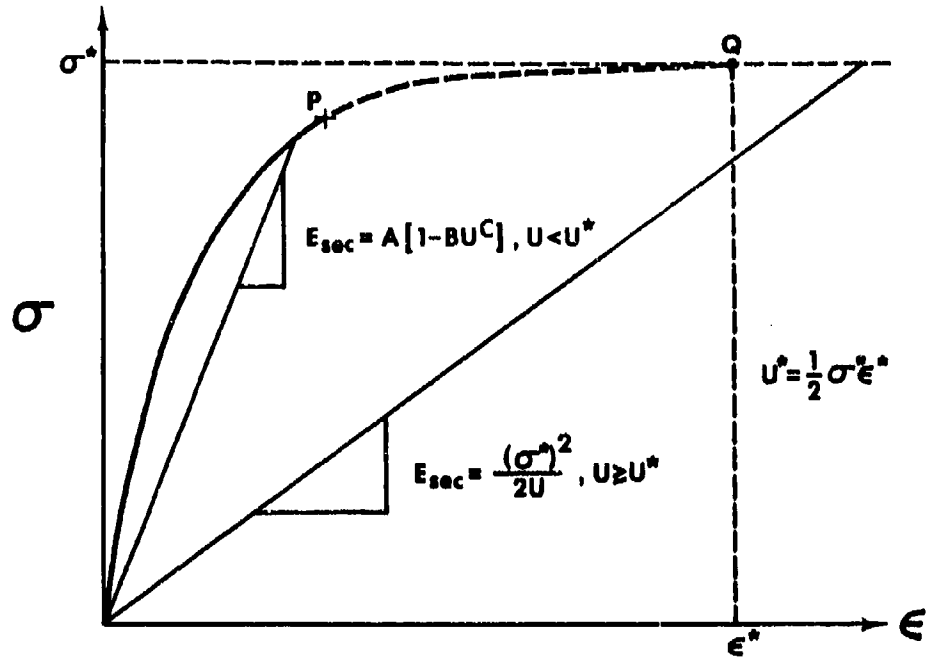

(a) STRESS-STRAIN CURVE EXTRAPOLATION

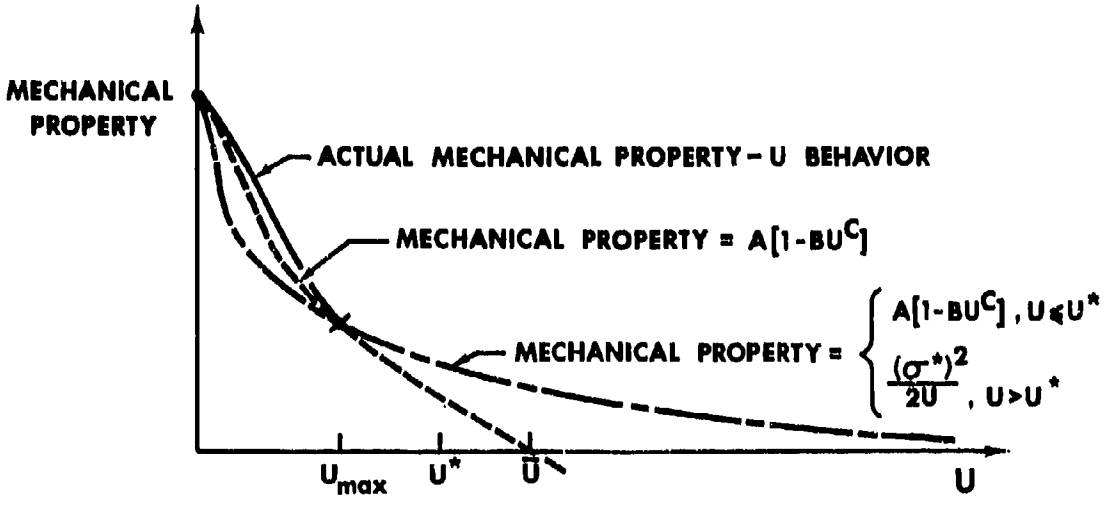

(b) MECHANICAL PROPERTY VERSUS STRAIN ENERGY CURVE EXTRAPOLATION

FIGURE 2-19 LINEAR STRESS-STRAIN CURVE EXTRAPOLATION WITH ZERO SLOPE BY ARBITRARY EXTENSION OF STRESS-STRAIN DATA

and strain associated with point Q are σ^* and ε^*, respectively. For strain energies less than ε^* ($U < U^* = 1/2\ \sigma^*\varepsilon^*$), the mechanical property is expressed as a function of the strain energy with the Jones-Nelson mechanical property expression in Eq. (2.3). The constants B and C are determined from data at points P and Q. For strains greater than ε^*, the stress-strain curve is considered to be linear with zero slope, and the mechanical property and strain energy can be expressed as:

$$\text{Mechanical Property} = \frac{\sigma^*}{\varepsilon} \qquad \varepsilon > \varepsilon^* \tag{2.14}$$

$$U = \sigma^*\varepsilon/2 \qquad \varepsilon > \varepsilon^* \tag{2.15}$$

Equations (2.14) and (2.15) are combined to obtain an expression for the mechanical property as a function of U:

$$\text{Mechanical Property} = \frac{(\sigma^*)^2}{2U} \qquad U > U^* \tag{2.16}$$

Thus, when the stress-strain curve is extended horizontally from the point of zero slope, the expression for the mechanical property for all strain energies is:

$$\text{Mechanical Property} = \begin{cases} A\left[1 - B\left(\dfrac{U}{U_0}\right)^C\right]; & 0 \leq U \leq U^* \\ \dfrac{(\sigma^*)^2}{2U}\ ; & U > U^* \end{cases} \tag{2.17}$$

The mechanical property versus strain energy curve in Fig. 2-19b corresponding to Eq. (2.17) approaches the U-axis asymptotically so the mechanical property is always positive. Hence, the horizontal stress-strain curve extension is a definite improvement over the extended me-

chanical property curve which crosses the U-axis as a strain energy of $\overline{U}$.

The major problem in extending the stress-strain curve horizontally in the foregoing manner is the determination of the point Q in Fig. 2-19a. The stress σ^* associated with point Q is determined by using engineering judgment to estimate the stress level at which the extended stress-strain curve becomes horizontal. Obviously, the exact stress level at which the curve becomes horizontal is ambiguous and depends on how the curve is extended. Many different choices of σ^* could be made. After σ^* is chosen, a complicated trial and error procedure based on mathematical constraints on the mechanical property expressions in Eq. (2.17) is used to determine ε^*. The objective of this procedure is to determine the strain (ε^*) at which the slope of the implied stress-strain curve is zero. A value of ε^* is chosen, and then the constants B and C are determined from data at point P and the point (σ^*, ε^*). Associated with each mechanical property equation is an implied stress-strain curve which is obtained by substitution of the definitions of the mechanical property and strain energy in Eq. (2.3) as

$$\frac{\sigma}{\varepsilon} = A\left[1 - B\left(\frac{\sigma\varepsilon}{2U_o}\right)^C\right] \tag{2.18}$$

For a specific value of strain, the corresponding stress is the root of the nonlinear equation:

$$\frac{\sigma}{\varepsilon} - A\left[1 - B\left(\frac{\sigma\varepsilon}{2U_o}\right)^C\right] = 0 \tag{2.19}$$

The slope of the implied stress-strain curve, obtained by differentiation of Eq. (2.18) and given by

$$\frac{d\sigma}{d\varepsilon} = \frac{A\left[(2U_o)^C - B(C+1)(\sigma^*\varepsilon^*)^C\right]}{(2U_o)^C + ABC\ (\sigma^*)^{C-1}(\varepsilon^*)^{C+1}} \tag{2.20}$$

is then evaluated at $(\sigma^*, \varepsilon^*)$. Then, the strain ε^* is adjusted and the constants B and C are recalculated until the slope in Eq. (2.20) is zero. The numerical technique of interval halving described in the Appendix is used in adjusting ε^* so that the search for the point of zero slope is orderly and converges rapidly.

The procedure for finding point Q is ambiguous and quite complicated. In addition, this horizontal extension of the stress-strain curve may lead to a poor representation of the measured stress-strain data. As a result, this method of extending the stress-strain curve horizontally is used only when very little stress-strain data are available and when the trend of the stress-strain data is such that any of the other extensions to be discussed subsequently is not valid.

The mechanical property expression in Eq. (2.17) is also valid for another linear stress-strain curve extension with zero slope which is less complicated than the one just described. Moreover, this extension is more representative of the measured stress-strain data for fiber-reinforced composite materials. This extrapolation involves adding a linear extension with zero slope to the implied stress-strain curve which is the best representation of the defined stress-strain data as shown in Fig. 2-20a. The constants A, B, and C in Eq. (2.17) are chosen so that the best approximation of the mechanical property versus strain energy data is obtained. Then, the implied stress-strain curve corresponding to this approximation is used not only as a representation of the stress-strain data but also as an extension of the stress-strain data from the last data point to the point $(\sigma^*, \varepsilon^*)$ in Fig. 2-20a. The point $(\sigma^*, \varepsilon^*)$

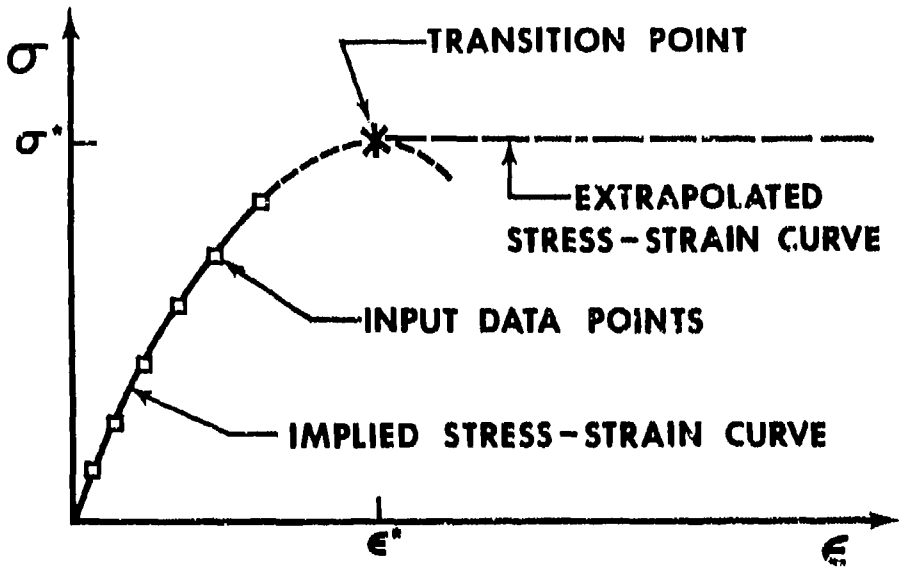

(a) STRESS-STRAIN CURVE EXTRAPOLATION

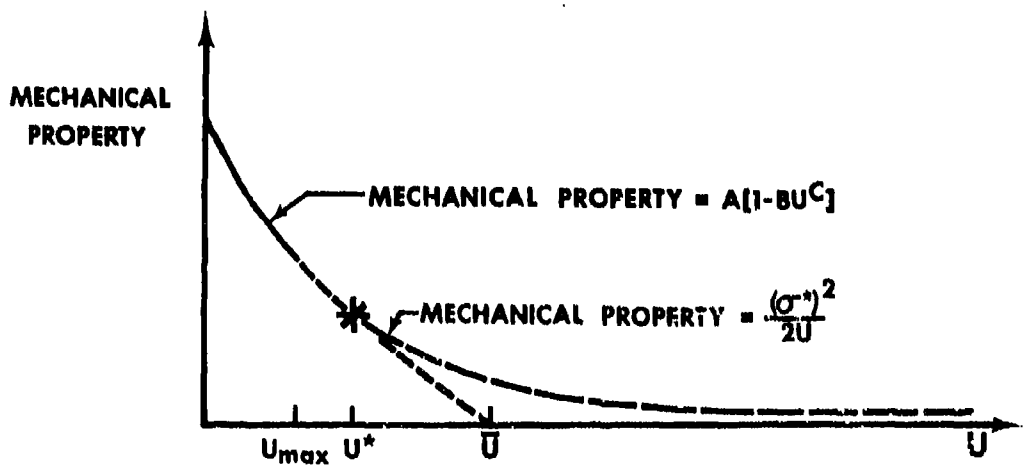

(b) MECHANICAL PROPERTY VERSUS STRAIN ENERGY CURVE EXTRAPOLATION

FIGURE 2-20 LINEAR STRESS-STRAIN CURVE EXTRAPOLATION WITH ZERO SLOPE WITH BEST FIT EXTENSION OF STRESS-STRAIN DATA

is the point on the extended stress-strain curve at which a change in the extrapolated stress-strain behavior occurs. For this extrapolation, $(\sigma^*, \varepsilon^*)$ in Fig. 2-20a corresponds to the point $(\tilde{\sigma},\tilde{\varepsilon})$ in Fig. 2-18; i.e., the slope of the implied stress-strain curve in Fig. 2-20a is zero at $(\sigma^*, \varepsilon^*)$. The implied stress-strain curve is not a reasonable extension of fiber-reinforced composite material behavior for strains greater than ε^*; so the stress-strain curve is extended as the horizontal line $\sigma = \sigma^*$ in Fig. 2-20a.

This method of extending the stress-strain curve with a straight line of zero slope is reasonable and simple because the constants A, B, and C in Eq. (2.17) are determined by fitting only the defined data and because the point $(\sigma^*, \varepsilon^*)$ is easily determined. The point $(\sigma^*, \varepsilon^*)$ is the point at which $\frac{d\sigma}{d\varepsilon}$ in Eq. (2.20) is zero and is determined with an interval halving technique which is described in the Appendix.

The mechanical property versus strain energy curve in Fig. 2-20b corresponding to the zero slope linear extension of the implied stress-strain curve is similar to the mechanical property versus strain energy curve corresponding to the horizontal extension in which σ^* is estimated from the trend of the data. Both mechanical property curves approach the U-axis asymptotically at large strain energies. However, the curve in Fig. 2-20b is a good representation of the defined data, whereas the curve in Fig. 2-19 is not.

The linear stress-strain curve extensions with zero slope discussed in this section are reasonable, but their use is limited. The mechanical property approaches zero for large strain energies although it is never zero nor negative. This behavior leads to problems when the mechanical property expression is used in stress analysis problems. The iteration

procedure designed for use in the solution of stress analysis problems diverges at large strain energies when the zero slope linear extension of the stress-strain data is used. The limit of validity for the horizontal extensions depends on the particular loading condition under investigation. Thus, an extrapolation which can be used regardless of the value of the strain energy is not obtained with the linear extension of zero slope approaches.

2.3.3.2 Linear Stress-Strain Curve Extensions with Nonzero Slope

The stress-strain data can be extrapolated by using a linear extension with nonzero slope. This extension can be used for all strain energies and can be accomplished in several ways. One approach is to approximate the stress-strain data (mechanical property - U data) with the Jones-Nelson mechanical property expression in Eq. (2.3) and to arbitrarily specify the slope that the linear extension should have. The implied stress-strain curve as shown in Fig. 2-21a is initially used as the extension of the measured stress-strain data. When the slope of the implied curve reaches the prescribed value, the stress-strain behavior is represented by a straight line with the prescribed slope. This linear stress-strain curve extension is expressed as:

$$\sigma = \left(\frac{d\sigma}{d\varepsilon}\right)^{*} \varepsilon + \sigma_0 \qquad \varepsilon > \varepsilon^{*} \tag{2.21}$$

where $\left(\frac{d\sigma}{d\varepsilon}\right)^{*}$ is the prescribed slope and σ_0 is the stress at which the linear extension intersects the stress axis. The constant σ_0 is easily determined once the point (σ^{*}, ε^{*}) in Fig. 2-21a is found. The point (σ^{*}, ε^{*}) at which the linear extension begins is calculated from the slope expression in Eq. (2.20).

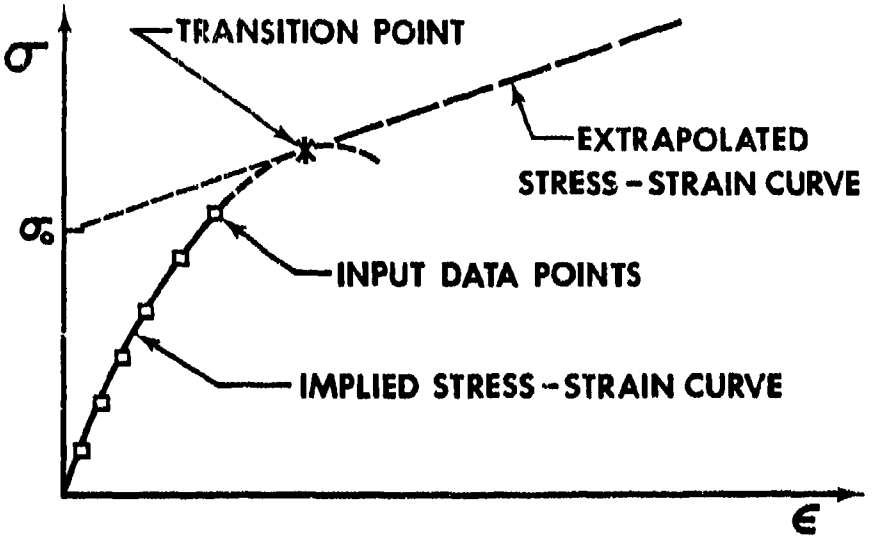

(a) STRESS-STRAIN CURVE EXTRAPOLATION

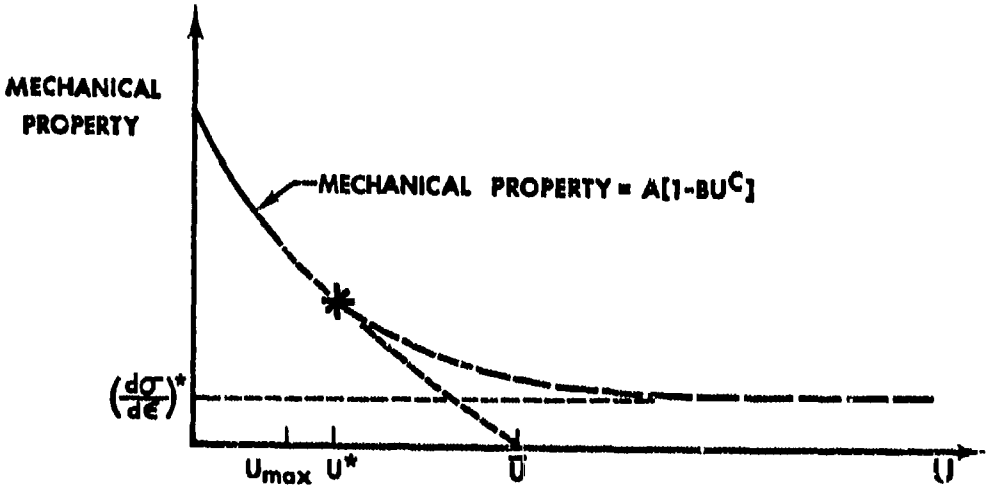

(b) MECHANICAL PROPERTY VERSUS STRAIN ENERGY CURVE EXTRAPOLATION

FIGURE 2-21 LINEAR STRESS-STRAIN CURVE EXTRAPOLATION WITH NONZERO SLOPE WITH BEST FIT OF STRESS-STRAIN DATA

The constants A, B, and C in the mechanical property expression are chosen so that a good representation of the measured stress-strain data is obtained. This representation of the data is not altered by the addition of the linear extension. In addition, the secant mechanical property in Fig. 2-21b approaches the slope $\left(\frac{d\sigma}{d\varepsilon}\right)^*$ of the linear extension for large strain energies; i.e.,

$$\lim_{U \to \omega} E_{sec} = \left(\frac{d\sigma}{d\varepsilon}\right)^* \tag{2.22}$$

The slope $\left(\frac{d\sigma}{d\varepsilon}\right)^*$ is nonzero so the extrapolation procedure of using the linear extension with nonzero slope can be used for all strain energies greater than U*. Actually, the linear extension with zero slope described in the preceding section is analogous to this linear extension with $\left(\frac{d\sigma}{d\varepsilon}\right)^* = 0$.

Another approach very similar to the one just described is to use the Jones-Nelson mechanical property expression to fit the stress-strain behavior only over the defined range. At the last data point in Fig. 2-22a, the stress-strain behavior is extended as a straight line with slope equal to the slope of the implied stress-strain curve at the last data point. For continuity between the implied stress-strain curve and the linear extension of the stress-strain behavior, the implied stress-strain curve must pass through the last measured data point. Thus, this data point is used in calculating the constants B and C in Eq. (2.3). For this extrapolation approach, the strain energies U_{max} and U* in Fig. 2-22b coincide. This approach of using a linear extension from the last defined data point is somewhat questionable in that the material may be represented as stiffer than it actually is at high strain energies.

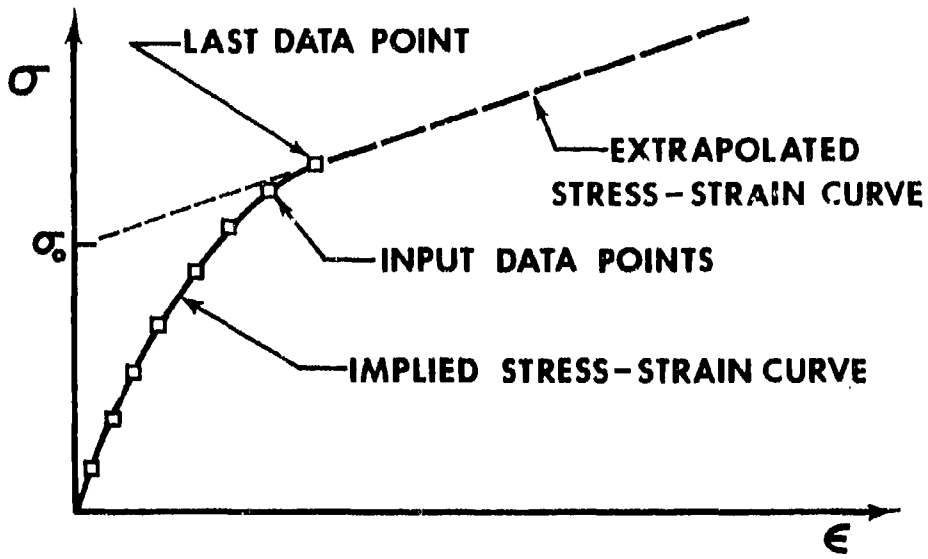

(a) STRESS-STRAIN CURVE EXTRAPOLATION

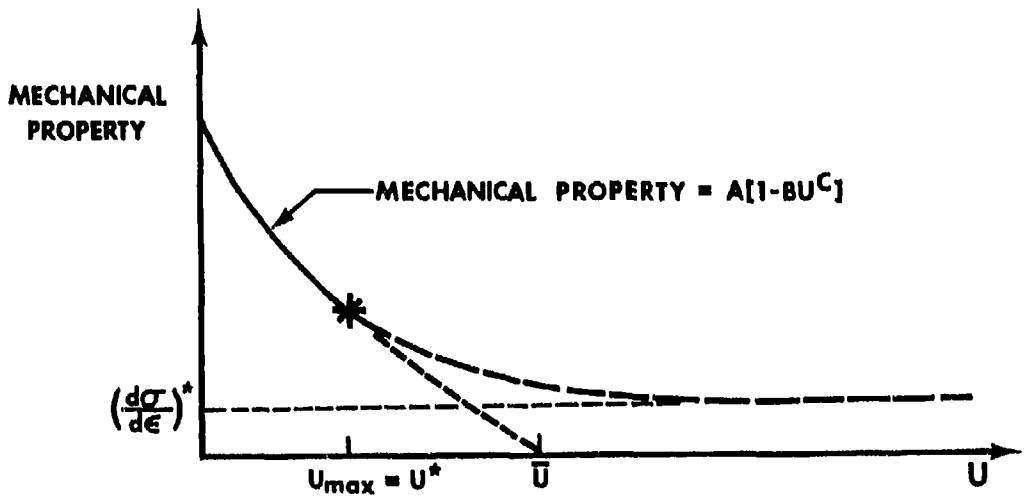

(b) MECHANICAL PROPERTY VERSUS STRAIN ENERGY CURVE EXTRAPOLATION

FIGURE 2-22 LINEAR STRESS-STRAIN CURVE EXTRAPOLATION WITH NONZERO SLOPE EQUAL TO SLOPE AT LAST DATA POINT

The mathematical technique of extrapolation is of course inexact. The best of the linear extensions with nonzero slope cannot be determined because comparison with measured stress-strain data is obviously not available or else the extrapolation would not be necessary. However, a choice between the two approaches is best made on an individual material basis. Both approaches should be used in the material model to predict material behavior under multiaxial or uniaxial loading conditions for which extrapolation is needed and for which measured data are available. The approach which leads to the best correlation between predicted and measured behavior should be used in the model for that particular material. The various material models in Section 2.2 and 2.3 are collectively referred to hereafter as the Jones-Nelson-Morgan nonlinear material model.

2.4 THE JNMDATA COMPUTER PROGRAM

The basic objective of the JNMDATA computer program is to automate the use of the Jones-Nelson-Morgan nonlinear material model. In particular, the Jones-Nelson-Morgan material model parameters are calculated from input measured stress-strain curve data points, the associated mechanical property versus strain energy curves are plotted, and the implied stress-strain curves are plotted. In both types of plots, the actual input data are also plotted so that a vivid comparison of the material model approximation to the data is available.

The actual stress-strain curve data points in Fig. 2-23a are converted in the JNMDATA program to mechanical property versus strain energy data points and are plotted in the form of Fig. 2-23b. However, these two types of data are tedious to plot by hand. Thus, the plotting feature of the program for these two types of information is quite attractive. Moreover, different Jones-Nelson-Morgan model fits to the data can

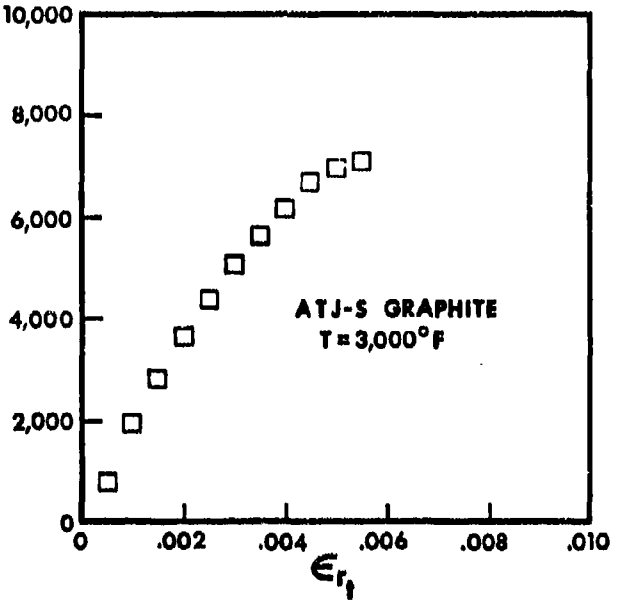

(a) STRESS-STRAIN DATA

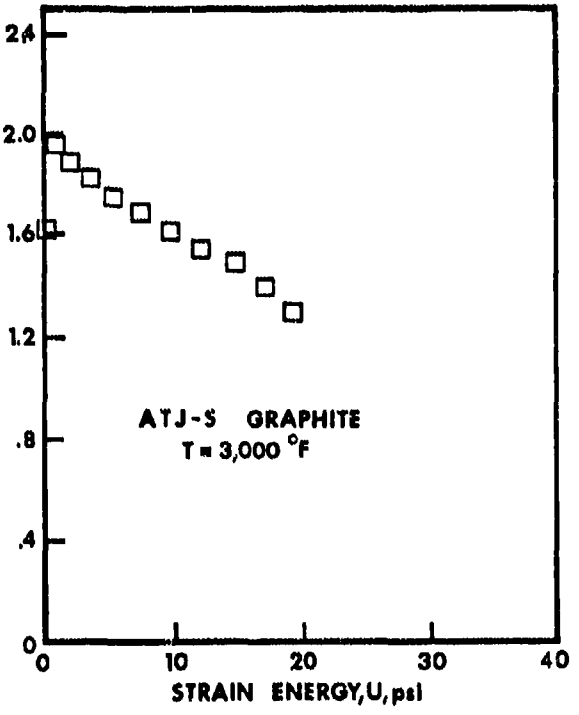

(b) MECHANICAL PROPERTY VERSUS ENERGY DATA

FIGURE 2-23 PLOTS OF ACTUAL STRESS-STRAIN DATA AND CORRESPONDING MECHANICAL PROPERTY VERSUS ENERGY DATA

be obtained as in Fig. 2-5 depending on the specific data points used to calculate the Jones-Nelson-Morgan parameters. The Jones-Nelson-Morgan model parameters are calculated in the program after the data points to be used are specified in the input data. Thus, the many model fits to the data with many combinations of points can be calculated and plotted as, for example, in Fig. 2-24. The best fit of all the possible fits is the one for which both the stress-strain data and the mechanical property versus strain energy data are simultaneously best approximated with the respective curves.

Generally, the problem is to obtain the best fit to the material property data for a single material. That material is usually more complicated than an isotropic material and has different stress-strain behavior at different temperatures. Thus, the process of obtaining these best fits for all properties at all temperatures involves a lot of work even with the JNMDATA program (and would be almost unthinkable without such an automating tool). Many successive computer runs are necessary in order to achieve the best fits. The two specified data points for each property at each temperature as in Figs. 2-4 and 2-5 are changed in each computer run along with the specified initial slope of the stress-strain curve until both the mechanical property versus strain energy curves and the associated implied stress-strain curves fit the data by passing through them as in Fig. 2-24.

The basic steps in the JNMDATA computer program are shown schematically in the simple flow chart of Fig. 2-25 and are described as:

(1) Read input stress-strain curve data as individual pairs of stress and corresponding strain values along with the identification of the points to be used in the model.

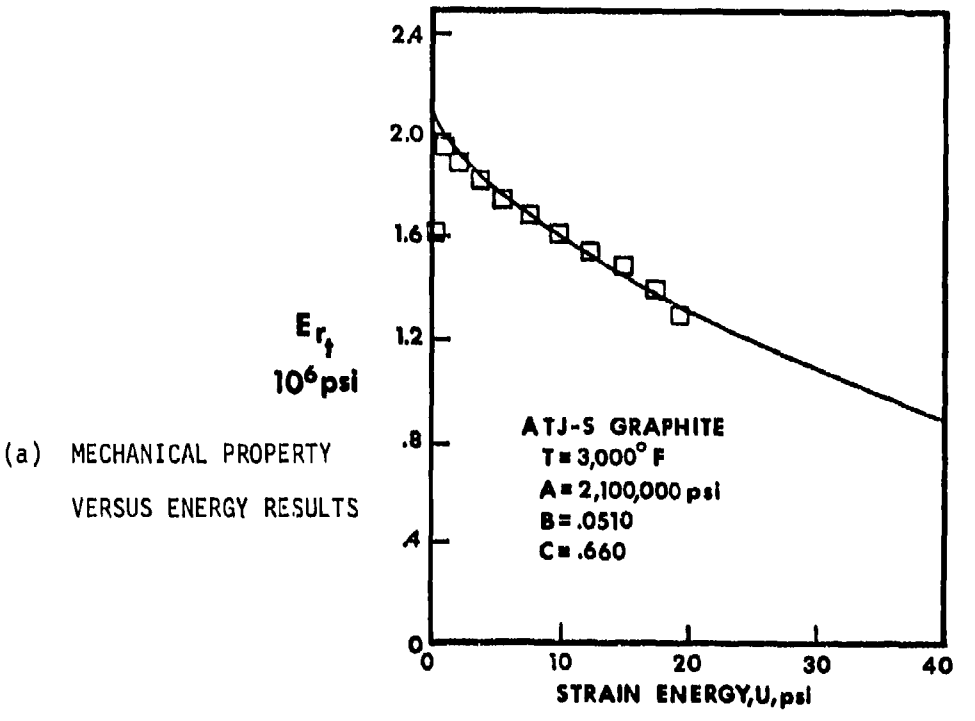

(a) MECHANICAL PROPERTY VERSUS ENERGY RESULTS

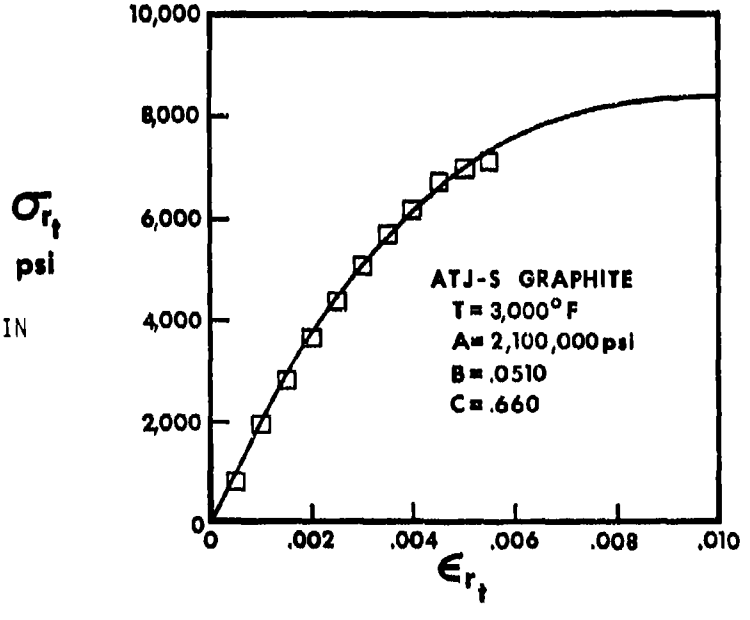

(b) STRESS-STRAIN RESULTS

FIGURE 2-24 JONES-NELSON NONLINEAR MATERIAL MODEL FOR DATA OF FIGURE 2-23

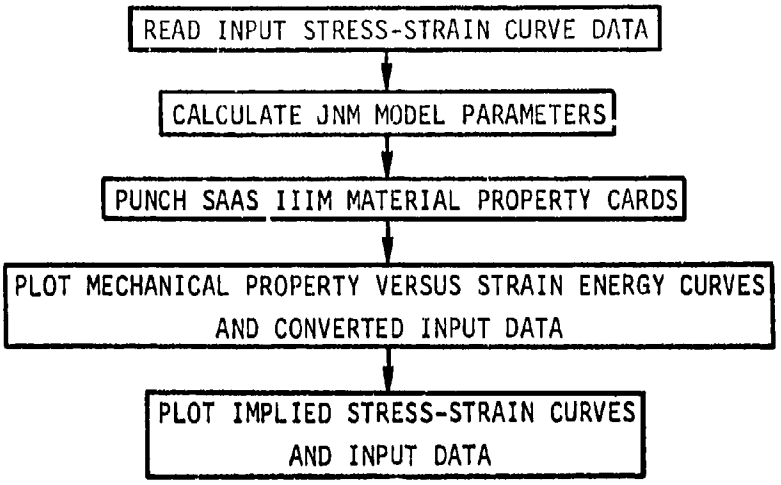

FIGURE 2-25 JNMDATA COMPUTER PROGRAM FLOW CHART

(2) Calculate the Jones-Nelson-Morgan model parameters from the data at the specified points.

(3) Punch material property cards for the Jones-Nelson-Morgan model in the SAAS IIIM format for direct use.

(4) Plot all the mechanical property versus strain energy curves for each mechanical property along with all the associated input data.

(5) Plot all the implied stress-strain curves for each mechanical property approximation along with the associated input stress-strain data.

The program output in the form of plots is inspected to see if the model fits for the specified set of data points to be used are good fits of the input data. If not, then the set of data points is revised based on experience and reinput to another run of the program. When one property is satisfactorily fit, then that property can be omitted from sub-

sequent computer runs. That is, for most materials, many properties are approximated - some better and sooner than others. For example, a transversely isotropic material with different moduli in tension and compression under axisymmetric load has five independent mechanical properties in tension (E_{r_t}, E_{z_t}, $\nu_{r\theta_t}$, $\nu_{z\theta_t}$, and $E^{45}_{rz_t}$) and five independent properties in compression (E_{r_c}, E_{z_c}, $\nu_{r\theta_c}$, $\nu_{z\theta_c}$, and $E^{45}_{rz_c}$). Each of these properties is plotted as in Fig. 2-24 except for the Poisson's ratios which are plotted as ν versus strain energy, $\varepsilon_{transverse}$ versus ε_{normal}, and σ_{normal} versus $\varepsilon_{transverse}$ as in Fig. 2-26. Plots of individual mechanical properties can be made as long as sufficient data are available, e.g., if $\nu_{r\theta_t}$ is desired, the corresponding direct modulus E_{r_t} must also be calculated and plotted. Thus, the satisfactorily approximated mechanical properties can be omitted from the subsequent computer runs so less time and money is expended. The computer charges are very low per run (typically about $10 on the SMU CDC CYBER 72), but the elapsed time to generate the plots is significant. At SMU, the mechanical prop-

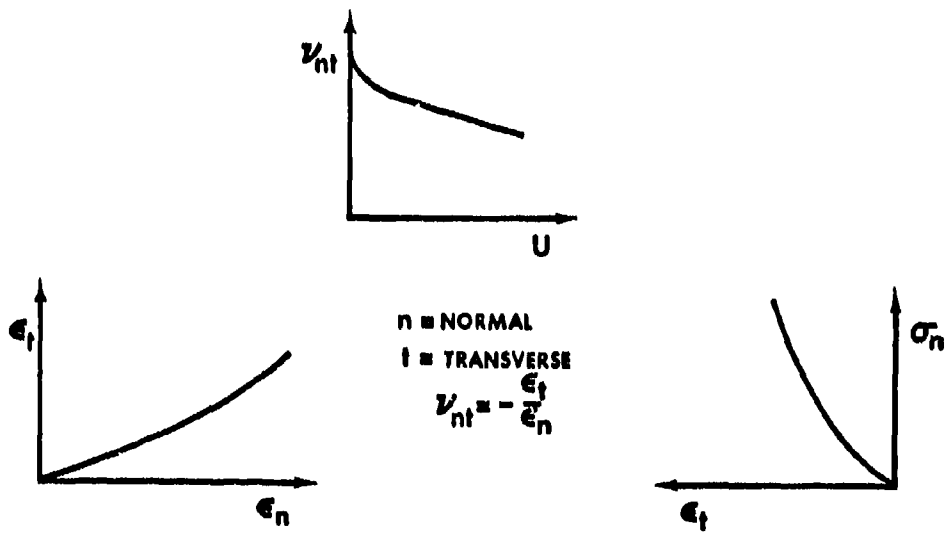

FIGURE 2-26 POISSON'S RATIO CURVES

erty versus strain energy curve and its associated stress-strain curve are plotted in five minutes. Thus, a full set of curves for a transversely isotropic multimodulus material is plotted in sixty minutes (5 minutes each for E_{r_t}, E_{z_t}, $E^{45}_{rz_t}$, E_{r_c}, E_{z_c}, and $E^{45}_{rz_c}$ and 7 1/2 minutes each for $\nu_{r\theta_t}$, $\nu_{z\theta_t}$, $\nu_{r\theta_c}$, and $\nu_{z\theta_c}$). Accordingly, any needed changes are made more quickly (less elapsed calendar time) if only the affected curves are replotted. This time constraint would be much less important for an oscilliscope-type plotter than for SMU's pen on paper (Zeta) plotter. Moreover, an interactive graphics terminal would be even more effective because changes could be made, their effects observed, and new changes made - all in rapid sequence.

In all calculations from input data, the potential data pitfalls discussed in Section 2.2.2, Implementation of the Material Model, are taken into account. That is, the program has "trapdoors" or "fixes" as appropriate for each of the pitfalls mentioned. In fact, several of the pitfalls were discovered during the development of the JNMDATA program. One such pitfall, a "low" first stress-strain curve data point is seen in Fig. 2-24 which is the with grain tensile stress-strain curve at 3000°F for ATJ-S(WS) Graphite from Fig. 5 of the SoRI Graphite Data Book [2-8]. Similar low first points are seen in Figs. 3, 4, 6, 7, 8, 9, and 10 of the SoRI Reference. We avoid these pitfalls by inputing an appropriate initial slope which is higher than the slope to the low first point and in fact higher than the slope to the second data point.

An interesting result from the JNMDATA program is that we now realize that the actual initial slope of a stress-strain curve is usually higher than the slope we graphically "pick off" the plotted stress-strain curve. For example, the slope we would pick off the σ_{r_c} versus ε_{r_c} curve at 70°

(Fig. 12 in the SoRI Graphite Data Book [2-8]) is

$$\text{SLOPE} = \frac{\sigma}{\varepsilon} = \frac{7010\text{psi}}{.004} = 1.752\text{x}10^{6}\text{psi}$$

The slope from the properly fit mechanical property versus energy data is $3.6\text{x}10^{6}$psi! Thus, our eyes deceive us when we attempt to visualize slope in the form of secant modulus to a stress-strain curve. The JNMDATA program is useful in remedying this situation because of the ability to plot the mechanical property (slope) directly.

In summary, the JNMDATA computer program is an exceptionally useful adjunct to the Jones-Nelson-Morgan nonlinear material model. The tedious calculations for the model are automated and the associated mechanical property versus strain energy curves and implied stress-strain curves are plotted. With this tool, rapid and highly visible material modeling can be performed.

3. MODELING OF GRAPHITIC MATERIALS

The use of the Jones-Nelson and Jones-Nelson-Morgan nonlinear material models for analysis of the behavior of graphitic materials is divided in three major parts. First, the Jones-Nelson model is applied to analysis of the Southern Research Institute thermal stress disk test. There, the model is used to predict the disk deformations which are then compared with the measured deformations. Second, the Jones-Nelson-Morgan model is applied to analysis of a nosetip subjected to the Air Force Flight Dynamics Laboratory 50 MW test environment. Finally, the application of Jones-Nelson and Jones-Nelson-Morgan modeling to graphitic materials is summarized.

3.1 THERMAL STRESS DISK TEST CORRELATION

3.1.1 INTRODUCTION

ATJ-S graphite is a transversely isotropic granular composite material which is made in cylindrical billet form as shown in Fig. 3-1 along

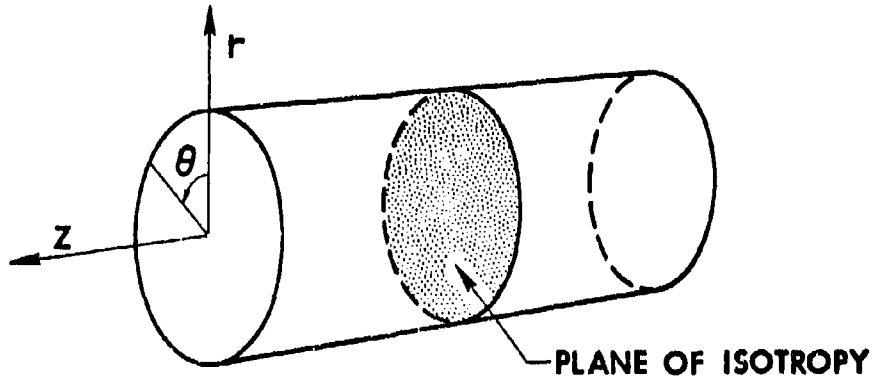

FIGURE 3-1 GRAPHITE BILLET COORDINATE SYSTEM

with the coordinates used in this section. The flake-like graphite particles are aligned in planes of isotropy during billet compaction in the z-direction. The resulting material stress-strain behavior is highly temperature-dependent as displayed for the r-θ plane in Fig. 3-2. There, the boxes are actual experimental data reported by Starrett and Pears [3-1] and the curves are the Jones-Nelson nonlinear material model [3-2 thru 3-6] fits to the data. In Fig. 3-2, the tension behavior becomes stiffer as the temperature approaches 2000°F and even stiffer at 3000°F. However, the stress-strain curve at 3000°F is slightly lower for high strains than at 2000°F. The compression behavior for the r-θ plane monotonically becomes more flexible as the temperature increases from 3000°F to 5000°F. Moreover, at every temperature, the stress-strain behavior is different under tension loading than under compression loading.

The objective of this section is to extend the qualification of the Jones-Nelson nonlinear material model [3-2 thru 3-6] from mechanical loading problems for homogeneous bodies to thermal loading problems for nonhomogeneous bodies. The previous level of qualification of the model is to uniaxial off-axis mechanical loading problems [3-3 and 3-6] and to biaxial mechanical loading problems in principal material directions for ATJ-S graphite [3-2 and 3-6]. The multimodulus character (different moduli or stiffnesses in tension than in compression) is treated by Jones and Nelson [3-5 and 3-6], but nonhomogeneous bodies due to temperature-dependent behavior have not been addressed with this model. Part of the motivation for this extension of the model is the use of ATJ-S graphite in reentry vehicle nosetips where substantial temperature gradients exist. These temperature gradients lead to thermal stresses for which the associated nonlinear deformations must be predicted in order to rationally

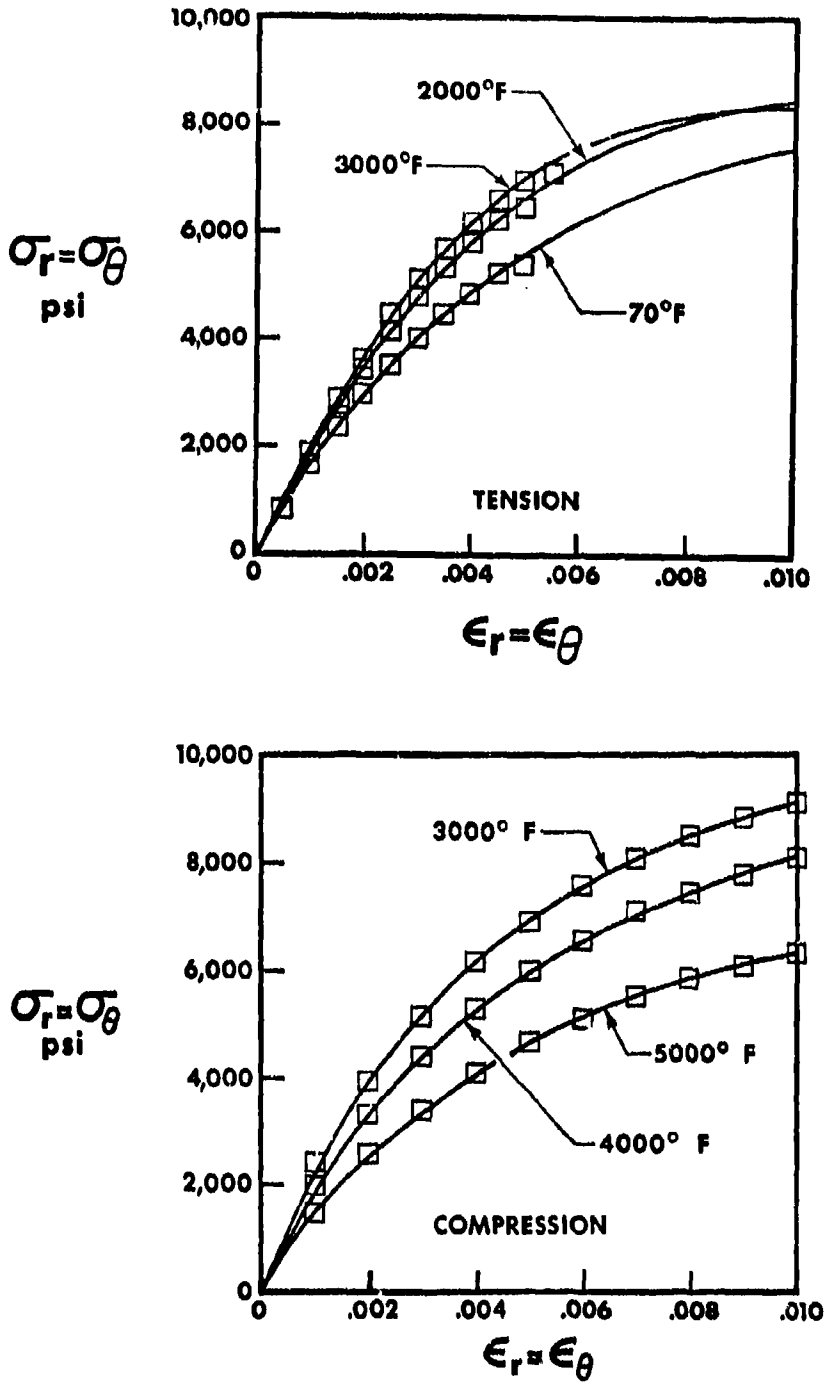

FIGURE 3-2 TEMPERATURE-DEPENDENT NONLINEAR MULTIMODULUS STRESS-STRAIN BEHAVIOR OF ATJ-S GRAPHITE

and accurately design nosetips and other structural elements.

The simplest vehicle to accomplish the objective of qualifying the model for thermal loading problems is the Southern Research Institute (SoRI) thermal stress disk test [3-7]. In this test, an annular disk is rapidly heated at its outer diameter resulting in an outside to inside diameter temperature gradient. The outside portion of the disk tends to expand more than the inside so thermal stresses are generated. In the circumferential direction, the stresses are compressive near the outer diameter and tensile near the inner diameter. The level of both the compressive and tensile stresses is important because the original purpose of the SoRI thermal stress disk test was to quickly and easily fail disks of many different graphites so their relative merits can be assessed. The failures almost invariably occur in the region of tensile stress. Accordingly, the compressive stresses must be high enough to generate (self-equilibrating) tensile stresses which will cause failure. The tensile stresses are too low for the simple flat annular disk and the rim disk in Fig. 3-3. That is, not enough disk material is in compression

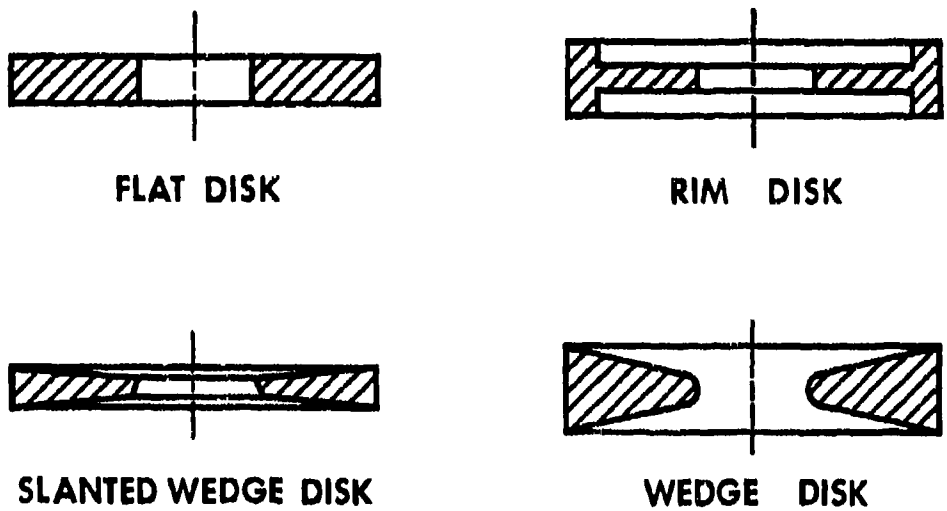

FIGURE 3-3 ANNULAR DISK CROSS SECTIONS

to force high enough tensile stresses for fracture to occur. However, the disks with a wedge-shaped cross section in Fig. 3-3 do have high enough tensile stresses to cause fracture. The slanted wedge disk has an inclined inner diameter surface to provide a well-defined target for the laser diameter measuring device which will be discussed later. The inner diameter of the wedge disk in Fig. 3-3 is, however, sufficiently well-defined to provide a good target. Thus, the simple wedge disk is used in the theoretical-experimental correlation studies.

This section is divided in two major subsections: (1) measurement of temperatures and deformations and (2) predicted deformations, stresses, and strains. In the measurements section (Section 3.1.2), the overall test setup is described along with the character of the individual measurements which are made. In the predictions section (Section 3.1.3), the Jones-Nelson nonlinear material model and its extensions for the present problem are described along with the modeling of ATJ-S graphite. Moreover, the predicted diameter changes are compared with the measured values. Finally, the stress state in the disk is displayed and discussed.

3.1.2 MEASUREMENTS OF TEMPERATURES AND DEFORMATIONS

3.1.2.1 Overall Test Setup

The SoRI thermal stress disk test [3-7] is basically a tension test in which the loads are induced solely by thermal deformation. Radial temperature gradients are generated in the disk by induction heating as shown in Fig. 3-4. The power from the induction heating coils is concentrated in the outer periphery of the disk (about 85% in the outer .10 inch) while the inside remains relatively cool. Many factors enter in the proper matching of the power supply to the test specimen, but the major considerations include coil design, specimen material, specimen

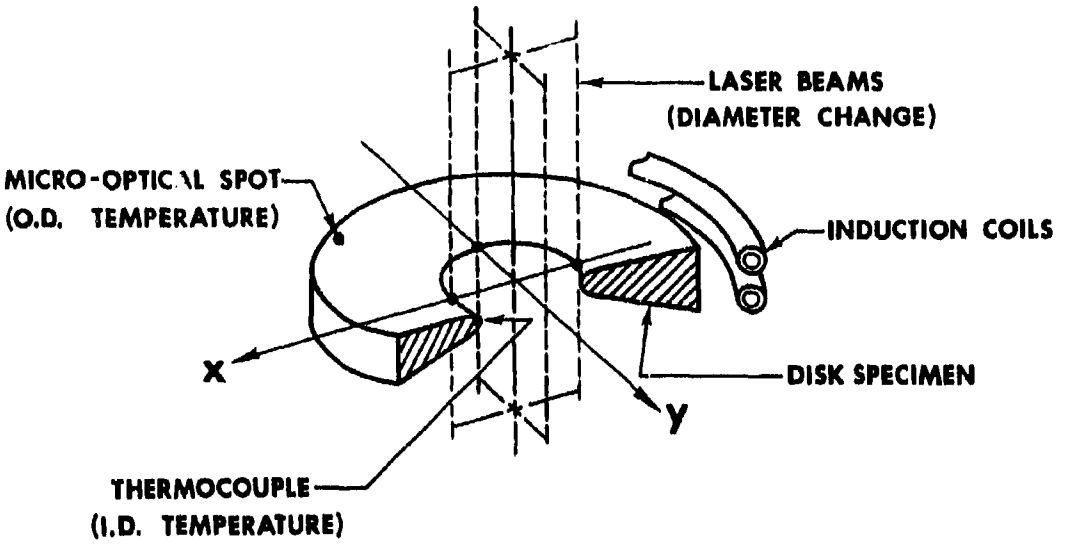

FIGURE 3-4 SCHEMATIC OF SoRI THERMAL STRESS DISK TEST

design, and specimen-to-coil proximity. The disk is made with its diameter in the graphite plane of isotropy shown in Fig. 3-1. The disk is not fastened to the test fixture, but is positioned horizontally as in Fig. 3-4 and rests on a smooth surface.

Several measurements are made during a single test run for an individual specimen. These measurements are (1) a temperature measurement at the inner diameter, (2) a temperature measurement at a point near the outer diameter, and (3) measurements of the diametral deformations along two orthogonal axes of the internal hole. Each of these measurements is discussed in the following subsections.

3.1.2.2 Inner Diameter Temperature Measurement

The temperature at the disk inner diameter is measured with a thermocouple probe. The fine thermocouple wires (10×10^{-3} inches) are not welded together but instead are spring pressed on the disk so the graphite makes the junction. This procedure is used to avoid a weld bead which

invariably leads to distortion of the parent material thermal characteristics and to errors of several hundred degrees at the heating rates used in this test.

The thermocouple probe is calibrated by obtaining a steady state reading between 1200°F and 2000°F for a graphite specimen and comparing that reading with the reading from an optical pyrometer which is corrected for emittance. The error due to the graphite junction is on the order of 70°F at 1500°F. Then, typical rapid heating runs are made and the thermocouple probe reading is compared to a micro-optical reading which is calibrated to a hand-held optical pyrometer. Thus, the basic calibration is for a range from the upper bound at the steady state reference to the lower bound at the calibration to the hand optical pyrometer through the micro-optical recorder. The temperature at the inside diameter is known to within 5°F on any run.

3.1.2.3 Outer Diameter Temperature Measurement

The temperature at the disk outer diameter is measured with a micro-optical recorder as a function of time. Thus, the temperature reading is subject to the errors normally associated with optically measuring the temperature of a gray body plus the errors peculiar to the particular specimen and to this system. The latter errors include those peculiar to transient measurements plus those resulting from the existence of a 200°F temperature gradient over the field of view of the recorder. That is, the recorder is focused on a spot as in Fig. 3-4 on the top surface of the disk since the outer diameter surface is covered by the induction coils. Since the spot is necessarily of finite width (about 45×10^{-3} inches) and is located in a region of high radial thermal gradient (about 4°F per 10^{-3} inch), inaccuracies in temperature measurement inevitably

occur.

Various calibration efforts for this measurement are discussed by Pears and Starrett [3-7]. They conclude that the micro-optical recorder can be used to measure temperatures up to about 5500°F on the disk outer surface and could be extended to even higher temperatures. The inherent accuracy of the readings is about ± 50°F up to 5000°F. However, the recorder slewing speed is approximately the same as the temperature rise in many tests so the final outer diameter temperature measurements are often ignored.

3.1.2.4 Diametral Deformation Measurements

The changes in the disk inner diameter are measured along x- and y-axes in Fig. 3-4 by use of a laser tracking device. The laser beams are focused and located with a complex prism system described by Pears and Starrett [3-7]. Basically, the two orthogonal diameter change measurements are different because the electronic circuitry is slightly different (each corresponding component of the two circuits is different within the manufacturers' tolerances). The output of the x- and y-measurements is recorded on the same recorder with offset initial points. These initial points are located by use of a tick mark placed on the recorder when the induction coils are turned on. The tick mark is not, however, recorded precisely when the coils are turned on. Pears and Starrett [3-7] conclude that the maximum diameter change error for a single experiment is 72×10^{-6} inches plus the timer error which in these correlations is eliminated by adjustment of the zero time mark.

3.1.2.5 Summary

The inner diameter temperature measurements are used to determine the approximate temperature distribution in the disk. That is, the the-

oretical temperature distributions at various times are shifted in time until the measured time when the predicted inner diameter temperature agrees with the measured inner diameter temperature. The outer diameter temperature is recorded at such a speed that the results are not meaningful. Otherwise, they could be used to further adjust the temperature distributions in the manner discussed for the inner diameter temperature measurements. The diametral deformation measurements are the primary measurements and are half of the basis for comparison of measured and predicted deformations.

3.1.3 PREDICTED DEFORMATIONS, STRESSES, AND STRAINS

The predicted deformations, stresses, and strains of the wedge-shaped annular disk are obtained with the Jones-Nelson nonlinear material model which is described in the next subsection. Then, the Jones-Nelson model of ATJ-S graphite is displayed and discussed. Next, the predicted inner diameter changes are compared with measured values. Finally, the stresses and strains in the disk are described.

3.1.3.1 Jones-Nelson Nonlinear Material Model

The Jones-Nelson nonlinear material model is described in References 3-2 thru 3-6. Here, we merely reiterate the details essential to our use of the model. Basically, the various secant moduli and Poisson's ratios, all of which are called mechanical properties, in the orthotropic stress-strain relations are approximated with

$$\text{Mechanical Property}_i = A_i \left[1 - B_i (U/U_{o_i})^{C_i} \right] \qquad (3.1)$$

where the A_i are the elastic values of the i^{th} mechanical property, the B_i and C_i are related to the initial curvature and initial change of curvature, respectively, of the stress-strain curve [3-3] (slightly different

interpretations exist for Poisson's ratios), and U is the strain energy density of an equivalent elastic system at each stage of nonlinear deformation:

$$U = (\sigma_r \varepsilon_r + \sigma_z \varepsilon_z + \sigma_\theta \varepsilon_\theta + \tau_{rz} \gamma_{rz})/2 \tag{3.2}$$

The strain energy density U in Eq. (3.1) is normalized by U_{o_i} so that B_i and C_i are dimensionless.

The Jones-Nelson model is actually much more complicated than Eq. (3.1). For example, in states of mixed tension and compression, the strain energy could be the total strain energy; the tension strain energy, U_t, for some properties and the compression strain energy, U_c, for other properties, or some weighted combination of the tension energy and the compression energy. The strain energy density used in this section is

$$U_W = (U_t^2 + U_c^2)/U \tag{3.3}$$

where U_W is the weighted strain energy. Moreover, all coefficients in Eq. (3.1) have different values in tension than in compression. The final combination of mechanical properties is determined in an iteration procedure wherein the stresses in principal stress directions are a key factor [3.5].

3.1.3.2 ATJ-S Graphite Mechanical Properties

The nonlinear stress-strain behavior in the plane of isotropy is depicted in Fig. 3-2. Since the disk is stressed primarily in the r-θ plane, we are concerned mainly with the properties in that plane. However, many other properties are necessary to perform an analysis. The values of A_i, B_i, and C_i are given as a function of temperature for all pertinent mechanical properties in Table 3-1 (the value of U_{o_i} is 1 psi for all properties). Also, the coefficients of thermal expansion are

TABLE 3-1

JONES-NELSON NONLINEAR MATERIAL MODEL PARAMETERS

FOR ATJ-S(WS) GRAPHITE AS A FUNCTION OF TEMPERATURE

TEMPERATURE	MECHANICAL PROPERTY	A	B	C
70°F	E_{r_t}	2.00×10^6 psi	.182	.337
	E_{z_t}	1.50×10^6 psi	.226	.322
	$\nu_{r\theta_t}$	.110	0.	1.
	$\nu_{z\theta_t}$	.090	0.	1.
	$E^{45}_{rz_t}$	1.55×10^6 psi	.200	.330
	E_{r_c}	3.00×10^6 psi	.477	.125
	E_{z_c}	2.10×10^6 psi	.451	.134
	$\nu_{r\theta_c}$	.065	0.	1.
	$\nu_{z\theta_c}$	.065	0.	1.
	$E^{45}_{rz_c}$	2.40×10^6 psi	.470	.130
2000°F	E_{r_t}	2.00×10^6 psi	.0651	.583
	E_{z_t}	1.60×10^6 psi	.165	.336
	$\nu_{r\theta_t}$	.130	0.	1.
	$\nu_{z\theta_t}$	.107	0.	1.
	$E^{45}_{rz_t}$	1.83×10^6 psi	.120	.460
	E_{r_c}	3.00×10^6 psi	.333	.203
	E_{z_c}	1.90×10^6 psi	.281	.221
	$\nu_{r\theta_c}$	.082	0.	1.
	$\nu_{z\theta_c}$	.082	0.	1.
	$E^{45}_{rz_c}$	2.84×10^6 psi	.350	.210

TABLE 3-1, continued

TEMPERATURE	MECHANICAL PROPERTY	A	B	C
3000°F	E_{r_t}	2.10×10^6 psi	.0510	.660
	E_{z_t}	1.45×10^6 psi	.0254	.921
	$\nu_{r\theta_t}$	.140	0.	1.
	$\nu_{z\theta_t}$	.116	0.	1.
	$E^{45}_{rz_t}$	2.11×10^6 psi	.0380	.790
	E_{r_c}	3.60×10^6 psi	.350	.198
	E_{z_c}	1.80×10^6 psi	.194	.291
	$\nu_{r\theta_c}$	.090	0.	1.
	$\nu_{z\theta_c}$	.090	0.	1.
	$E^{45}_{rz_c}$	3.27×10^6 psi	.310	.240
3500°F	E_{r_t}	2.40×10^6 psi	.277	.212
	E_{z_t}	1.40×10^6 psi	.133	.395
	$\nu_{r\theta_t}$	.145	0.	1.
	$\nu_{z\theta_t}$	.120	0.	1.
	$E^{45}_{rz_t}$	2.04×10^6 psi	.158	.388
	E_{r_c}	3.60×10^6 psi	.316	.220
	E_{z_c}	2.00×10^6 psi	.158	.347
	$\nu_{r\theta_c}$	.0950	0.	1.
	$\nu_{z\theta_c}$	.0950	0.	1.
	$E^{45}_{rz_c}$	3.27×10^6 psi	.270	.290

TABLE 3-1, concluded

TEMPERATURE	MECHANICAL PROPERTY	A	B	C
4000°F	E_{r_t}	2.70×10^6 psi	.282	.237
	E_{z_t}	1.40×10^6 psi	.107	.477
	$\nu_{r\theta_t}$	.150	0.	1.
	$\nu_{z\theta_t}$	.125	0.	1.
	$E^{45}_{rz_t}$	1.97×10^6 psi	.200	.360
	E_{r_c}	2.80×10^6 psi	.323	.212
	E_{z_c}	1.80×10^6 psi	.153	.377
	$\nu_{r\theta_c}$	.100	0.	1.
	$\nu_{z\theta_c}$	.100	0.	1.
	$E^{45}_{rz_c}$	3.06×10^6 psi	.270	.300
4500°F	E_{r_t}	2.50×10^6 psi	.300	.250
	E_{z_t}	1.30×10^6 psi	.100	.500
	$\nu_{r\theta_t}$	.170	0.	1.
	$\nu_{z\theta_t}$	.150	0.	1.
	$E^{45}_{rz_t}$	1.50×10^6 psi	.200	.400
	E_{r_c}	2.40×10^6 psi	.275	.250
	E_{z_c}	1.80×10^6 psi	.244	.267
	$\nu_{r\theta_c}$	.150	0.	1.
	$\nu_{z\theta_c}$	.150	0.	1.
	$E^{45}_{rz_c}$	2.40×10^6 psi	.300	.270

given in Table 3-2. Both sets of data are obtained from Ref. 3-1. The direct moduli E_r and E_z are shown in stress-strain curve form in Ref. 3-1 along with tables of (constant) Poisson's ratios and coefficients of thermal expansion. The values for E_{rz}^{45} are obtained by observing the relation between the coefficients in Eq. (3.1) for E_{rz}^{45}, E_r, and E_z measured for ATJ-S graphite at room temperature by Jortner [3-8] and applying that relation to the measured data for E_r and E_z at elevated temperatures.

The boxes in Fig. 3-2 are actual data from Ref. 3-1, and the curves are Jones-Nelson curves through the data. The curves are obtained by use of the JNMDATA computer program in which all the stress-strain curve data are input along with instructions for which points to use in the calculation of A_i, B_i, and C_i. Obviously, very good fits to the data can be generated with the JNMDATA computer program. Moreover, all stress-

TABLE 3-2

COEFFICIENTS OF THERMAL EXPANSION FOR ATJ-S(WS) GRAPHITE AS A FUNCTION OF TEMPERATURE

TEMPERATURE ^{o}F	α_r 10^{-5} per ^{o}F	α_z 10^{-5} per ^{o}F
70	.1200	.1720
2000	.1915	.2471
3000	.2194	.2727
3500	.2315	.2864
4000	.2414	.2997
4500	.2547	.3174

strain curves and mechanical property versus strain energy curves can be plotted easily.

The data in Tables 3-1 and 3-2 are input to a version of the SAAS III finite element stress analysis computer program [3-9] which has been modified to use the Jones-Nelson material model. In the use of the new version called SAAS IIIM, stress-strain data at temperatures between the values listed in Tables 3-1 and 3-2 must be generated. If the Jones-Nelson parameters A_i, B_i, and C_i for T = 70°F and T = 2000°F are interpolated for a specific temperature, say 1403°F which is the inner diameter temperature at t = 1.9 seconds, then the stress-strain curve labeled "PARAMETER INTERPOLATION FOR 1403°F" in Fig. 3-5 results. However, this stress-strain curve doesn't lie between the two curves from which it is interpolated. On the other hand, if the nonlinear mechanical properties calculated from Eq. (3.1) for T = 70°F and T = 2000°F are interpolated (i.e., E_{r_t} at 70°F and at 2000°F), then the curve labeled "PROPERTY INTERPOLATION" in Fig. 3-5 results. Finally, if the points at the same strain energy on the two stress-strain curves are interpolated, then the curve labeled "STRESS-STRAIN CURVE INTERPOLATION" in Fig. 3-5 results. Obviously, the latter two approaches coincide for all practical purposes. The property interpolation approach is used in SAAS IIIM because it is simpler to program and cheaper to execute than the stress-strain curve interpolation approach.

3.1.3.3 Inner Diameter Change Predictions

Times late in the test run are selected for correlation of predicted and measured results. Then, the disk should be deforming nonlinearly, i.e., the stresses should be inelastic. The power in the induction coils does not reach the nominal levels used to predict the temperature distri-

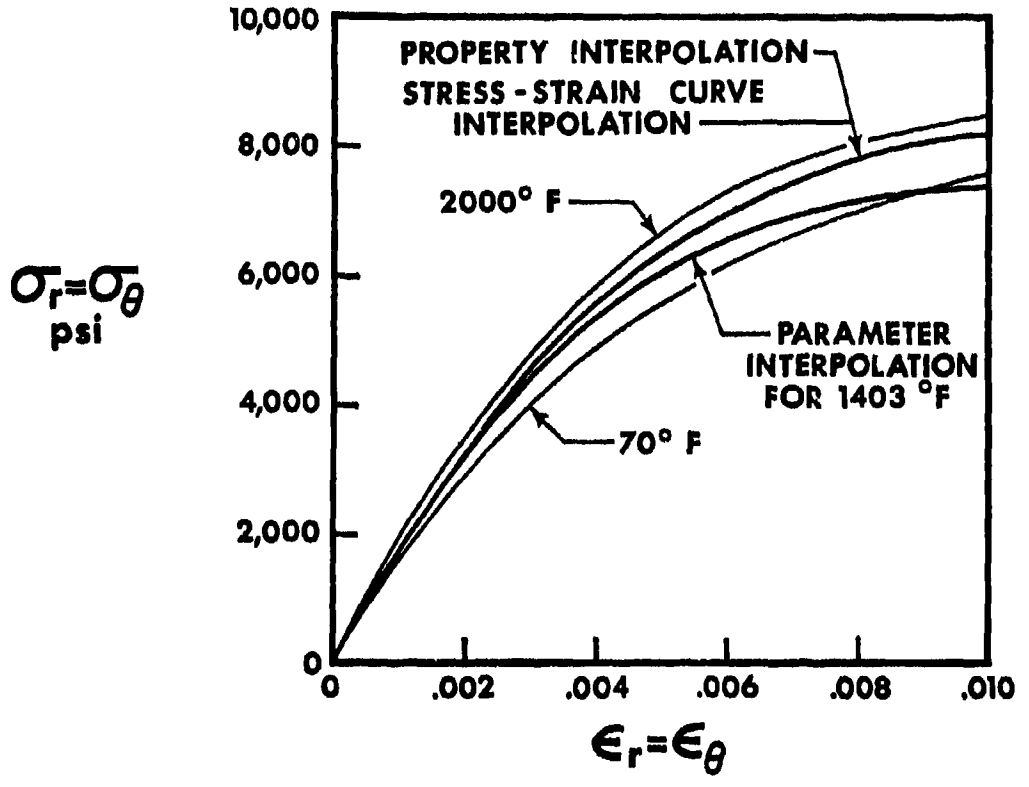

FIGURE 3-5 TEMPERATURE INTERPOLATION OF STRESS-STRAIN BEHAVIOR

butions at various times with the MOATS heat transfer computer program [3-10] (in which convection is not considered). Hence, the temperature gradients are lower at all times than predicted. We account for this discrepancy by assuming that a predicted temperature distribution at one time with a specific inner diameter temperature is the actual temperature distribution at another time when the predicted inner diameter temperature is the same as the measured temperature. The validity of this time-power shift hypothesis would be even more plausible if we could also match predicted and measured outer diameter temperatures. However, the outer diameter temperature measurement with a micro-optical recorder is not sufficiently accurate to be relied upon because the temperature rise is too fast for the recording device speed used for all measurements. Thus, we depend on the inner diameter temperature correlation to determine the times at which the predicted temperature distributions are applicable. These times, t = 1.2, 1.55, and 1.9 seconds, correspond to measured inner diameter temperatures of 889^{o}F, 1135^{o}F, and 1410^{o}F whereas the predicted temperatures are 886^{o}F, 1130^{o}F, and 1402^{o}F, respectively. Revision of these times to force the predicted temperatures to correspond more closely to the measured temperatures is regarded as unnecessary. The actual calibrated inner diameter temperatures are plotted as a function of time in Fig. 3-6. There, dots are used to denote the times and corresponding temperatures at which the deformations, stresses, and strain are predicted. The predicted deformations should be slightly too low because the temperature gradient increases with time and the predicted temperatures are lower than the measured temperatures.

The measured inner diameter changes are shown in Fig. 3-7 for two orthogonal directions as a function of time. The change of diameter in

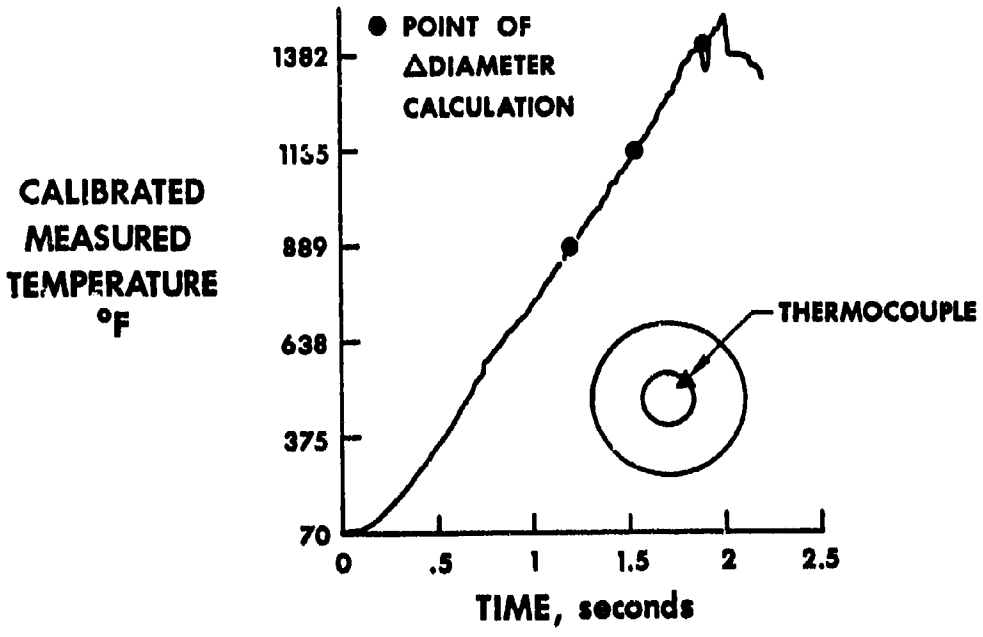

FIGURE 3-6 INNER DIAMETER TEMPERATURE VERSUS TIME

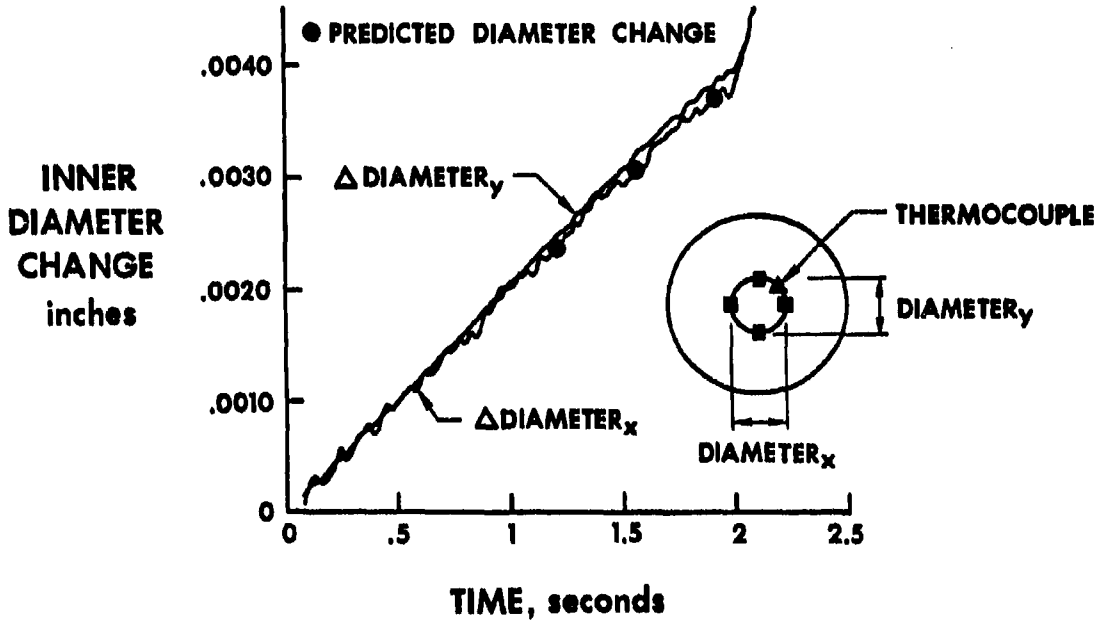

FIGURE 3-7 INNER DIAMETER CHANGE VERSUS TIME

the two directions is measured with two electronically equivalent but not identical circuits. The measurement in the y-direction is much less noisy than in the x-direction. However, both measurements are sufficiently accurate for the present correlation effort without calibration. The difference in measured deformations in the x- and y-directions can also be attributed to the disk hole not remaining perfectly circular. Of course, the hole should remain circular since the material is nominally isotropic in the plane of the hole and the temperature distribution is axisymmetric about the z-axis perpendicular to the plane of the disk. However, the material does not have perfect transverse isotropy nor is the temperature distribution perfectly axisymmetric.

The predicted inner diameter changes are plotted in Fig. 3-7 for t = 1.2, 1.55, and 1.9 seconds. These predictions are obtained with the SAAS IIIM finite element computer program for which the disk finite element mesh is shown in Fig. 3-8. The SAAS IIIM program is the SAAS III

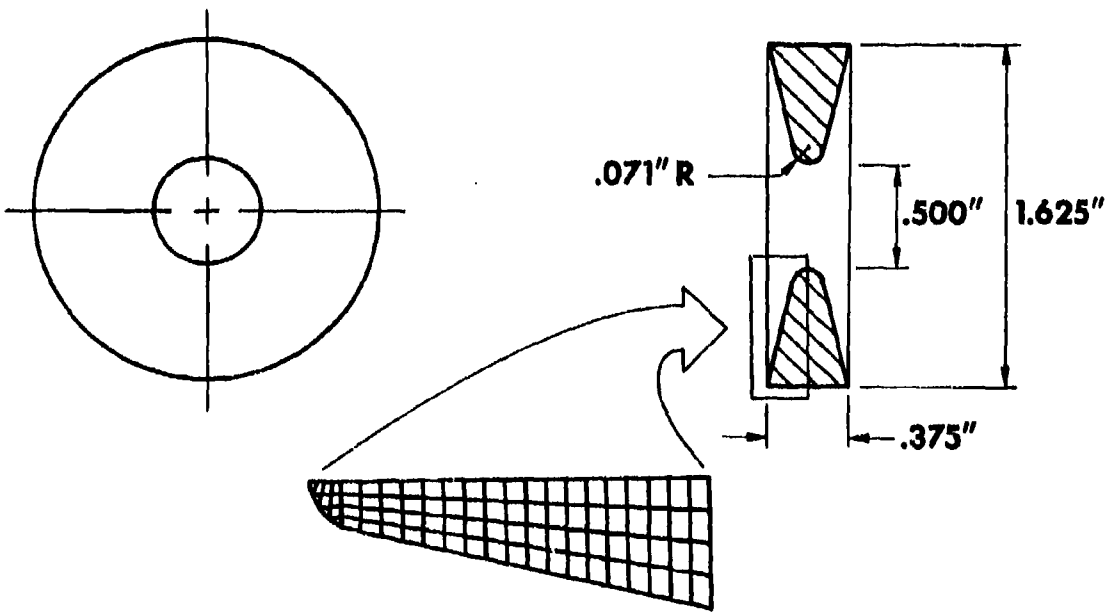

FIGURE 3-8 WEDGE-SHAPED ANNULAR DISK AND FINITE ELEMENT IDEALIZATION

program [3-9] with the Jones-Nelson nonlinear material model incorporated. As is obvious from Fig. 3-7, the predicted deformations are quite close to the measured values. The actual numerical values are listed in Table 3-3 wherein we observe that the predicted deformations are within 2.2 to 3.3% of the average of the two measured diameter changes.

TABLE 3-3

MEASURED AND PREDICTED INNER DIAMETER CHANGES

TIME seconds	I.D. TEMPERATURE °F		CHANGE IN INTERNAL DIAMETER, inches				
			MEASURED			PREDICTED	% ERROR
	MEASURED	USED IN CALCULATION	X-CHANNEL	Y-CHANNEL	AVERAGE		
1.2	889	886	.00230	.00250	.00240	.00232	3.3
1.55	1135	1130	.00300	.00320	.00310	.00303	2.2
1.9	1410	1402	.00365	.00390	.00378	.00367	2.9

3.1.3.4 Stress and Strain Predictions

The predicted stresses σ_r and σ_θ are shown along with the corresponding temperature distribution at t = 1.9 seconds in Fig. 3-9. Although we expect σ_θ to predominate, substantial values of σ_r exist. These radial stresses are always tensile and can be explained with the aid of the free body diagrams in Fig. 3-10. There, the view is down the z-axis of the disk perpendicular to the plane of the disk. The shear stress $\tau_{r\theta}$ is zero by virtue of axial symmetry of the loading and geometry. The free bodies extend through the (variable) thickness of the disk so the shearing stress τ_{rz} is zero. In the body next to the outer diameter, the circumferential

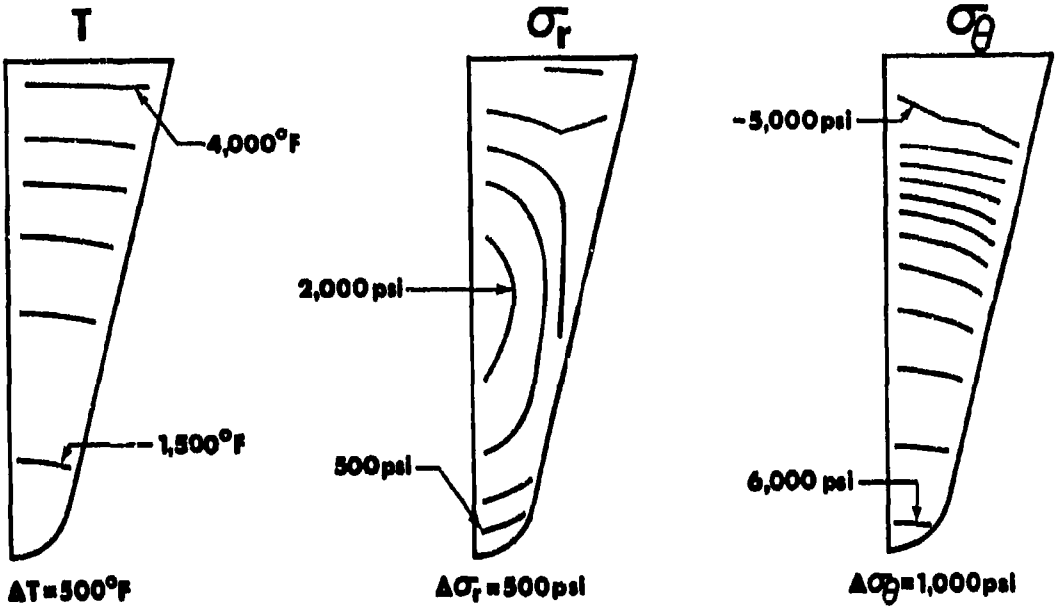

FIGURE 3-9 TEMPERATURE AND STRESS DISTRIBUTIONS AT t = 1.9 second

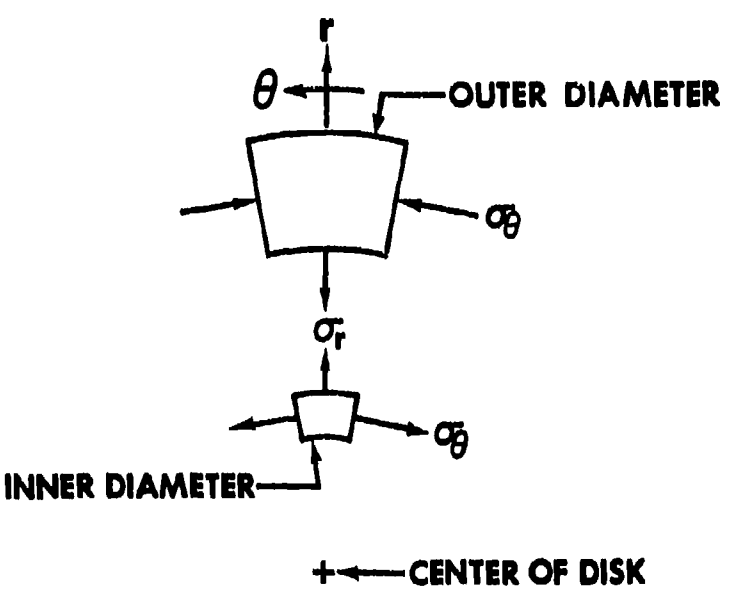

FIGURE 3-10 FREE BODY DIAGRAMS OF INNER DIAMETER AND OUTER DIAMETER ELEMENTS

stress is compressive. Thus, the radial stress must be tensile to achieve equilibrium, i.e., to balance the component of σ_θ in the negative r-direction. At the radial location where the circumferential stress is zero, the radial stress is also zero. Of course, the radial stress is zero on the unloaded inner and outer surfaces. Despite these surfaces of zero radial stress, σ_r can have substantial values elsewhere because of the small disk inner diameter and the high circumferential stresses to which σ_r is inversely proportional and proportional, respectively.

The stress-strain behavior becomes more and more nonlinear when the test time increases as we see from the increasing disparity between elastic and nonlinear stresses in Table 3-4. The disparity increases to nearly a factor of two at t = 1.9 seconds. This disparity is depicted

TABLE 3-4

PREDICTED CIRCUMFERENTIAL STRESSES AND STRAINS

TIME seconds	ELEMENT	TEMPERATURE °F	σ_θ, psi		ε_θ		$\Delta\sigma$	$\Delta\varepsilon$
			ELASTIC	NONLINEAR	ELASTIC	NONLINEAR		
1.2	1(I.D.)	887	6,295	4,717	.00313	.00336	-25%	+7%
	82(O.D.)	2,890	-5,339	-4,515	-.00252	-.00248	-16%	-2%
1.55	1(I.D.)	1,131	8,233	5,671	.00409	.00429	-31%	+5%
	82(O.D.)	3,457	-7,442	-5,501	-.00308	-.00307	-26%	0%
1.9	1(I.D.)	1,403	10,608	6,380	.00527	.00500	-40%	-5%
	82(O.D.)	4,057	-9,806	-5,071	-.00360	-.00379	-48%	+5%

graphically for circumferential stresses and strains in Fig. 3-11. There, the elastic stresses are too high by nearly a factor of two. However, the elastic strains are not as different from the nonlinear strains as the corresponding stresses. Moreover, the elastic strains are not always higher than the nonlinear strains. In fact, the nonlinear inner diameter strain decreases by only 5% and the nonlinear outer diameter strain increases by about 5% from the respective elastic strains! Thus, a failure criterion based on elastic strains is much more accurate than a failure criterion based on elastic stresses. However, even an elastic strain failure criterion is inaccurate because of the 5% error in predicting elastic strains and the fact that the error is sometimes positive and sometimes negative.

The stresses, strains and displacements converge to the final results in 5, 5, and 6 iterations at t = 1.2, 1.55, and 1.9 seconds, respectively.

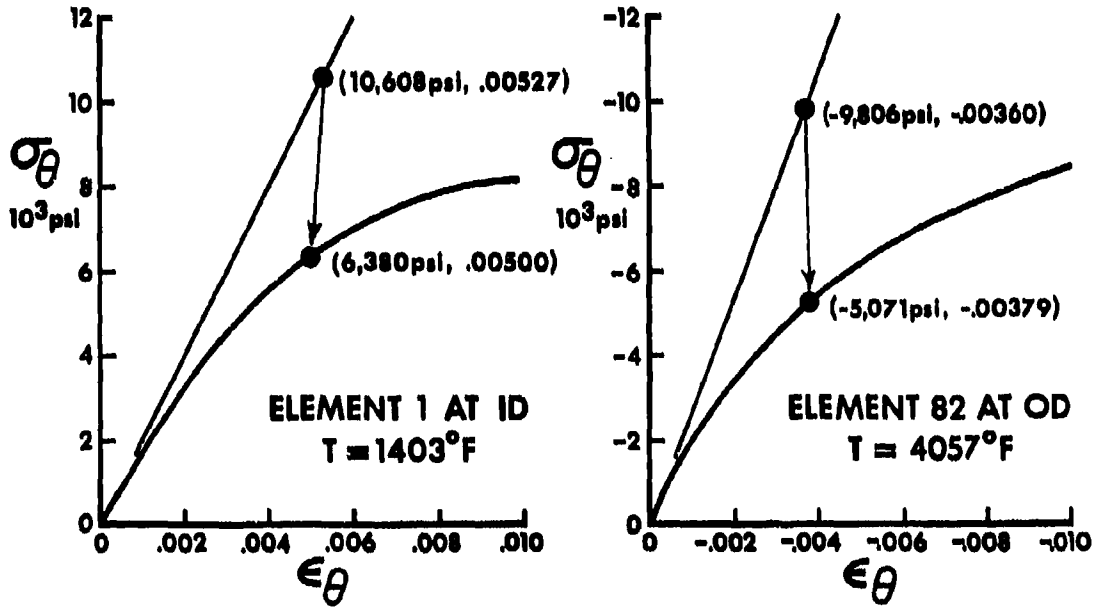

FIGURE 3-11 DEGREE OF NONLINEAR STRESS-STRAIN BEHAVIOR

Thus, the rapidity of convergence depends on the degree of nonlinearity which increases with test time. The inner diameter stresses at t = 1.9 seconds in Table 3-5 oscillate with decreasing amplitude about the final results. However, the inner diameter strains and displacements monotonically decrease to the final values.

The energies in the elastic state are well above the energies in the actual nonlinear states. Thus, the energies in the iteration procedure must decrease as the number of iterations increases. Conceivably, the elastic energy could be so much higher than the actual nonlinear energy that the Jones-Nelson model would not converge because of unfavorable numerical characteristics of the various stress-strain curves (first rising, then falling as for 3000°F in tension in Fig. 3-2). However, that unfortunate numerical behavior is not found in this problem. If such a difficulty arises, it can be remedied by use of the extended stress-strain

TABLE 3-5

PREDICTED CIRCUMFERENTIAL STRESSES AND STRAINS AT I.D. ELEMENT 1 AND RADIAL DISPLACEMENTS AT I.D. NODAL POINT 2 AT t = 1.9 seconds

ITERATION	σ_θ, psi	ε_θ	u_r, inches
1	10,608	.00527	.001903
2	5,722	.00503	.001841
3	6,543	.00500	.001834
4	6,345	.00500	.001834
5	6,390	.00500	.001833
6	6,380	.00500	.001833

curve approaches due to Jones and Morgan [3-11].

3.1.4 SUMMARY

The Jones-Nelson nonlinear material model is extended from mechanical loading problems for homogeneous bodies to thermal loading problems for nonhomogeneous bodies. The nonhomogeneity results from a temperature gradient over a body with temperature-dependent mechanical properties. Moreover, the model is shown to be valid for materials which have highly nonlinear stress-strain behavior which is different under tension loading than under compression loading.

The vehicle for the verification of the model extension is the SoRI thermal stress disk test. The inner diameter changes of this annular wedge-shaped disk made of ATJ-S graphite are predicted with the model to within about 3%. The mechanical properties of ATJ-S graphite are a strong function of temperature and stress level. Thus, the present results are a severe test of the model and are an important step in the qualification of the model for general use in nonlinear material deformation problems.

3.2 50 MW NOSETIP STRESS ANALYSIS

3.2.1 INTRODUCTION

The stress and strain field is analyzed in an ATJ-S graphite nosetip subjected to the Air Force Flight Dynamics Laboratory 50 MW arc jet facility environment. The nosetip design is supposedly representative of stress states that exist during reentry. Moreover, the nosetip model is supposed to fail during the test. The specific test condition analyzed is 50 MW Run R41-016 at t = 1.60 seconds. The nosetip is of the shell type (as opposed to the plug type) and has a .75" nose radius, 1" overhang, 10° half cone angle, and .15" wall thickness as shown in Fig. 3-12.

The temperature distribution at t = 1.60 seconds displayed in Fig. 3-13 was calculated with the ASTHMA, ARGEIBL, and BLIMP computer programs at Aerotherm Division of Acurex Corporation and provided to Southern Methodist University by AFML. The corresponding surface pressure distribution in Fig. 3-14 was also provided to SMU.

The stresses and strains predicted with the Jones-Nelson-Morgan nonlinear material model are displayed in contour plot form in Section 3.2.2 along with the specific ATJ-S graphite mechanical properties which are used. These stresses and strains are compared in Section 3.2.3 with those predicted by Baker, Jackson, Starrett, and Budde [3-12] who used the DOASIS computer program [3-13]. The basic efforts of this study are summarized in Section 3.2.4.

3.2.2 JONES-NELSON-MORGAN NONLINEAR MATERIAL MODEL PREDICTIONS

The Jones-Nelson-Morgan model predictions are based on the mechanical properties of ATJ-S graphite given in Section 3.2.2.1. Then, in Section 3.2.2.2, the predicted elastic stresses and strains are displayed. Finally, the predicted nonlinear stresses and strains are presented in Section 3.2.2.3.

3.2.2.1 ATJ-S Graphite Mechanical Properties

The basic source of information for ATJ-S graphite mechanical properties is the SoRI ATJ-S data book [3-1]. However, those data are modeled with the Jones-Nelson-Morgan nonlinear material model instead of with the Jones-Nelson nonlinear material model as in the Thermal Stress Disk Test Correlation in Section 3.1. The reason for this new approach is that the stresses and consequently the energy in the nosetip is too high for convergence of the basic Jones-Nelson model. That is, the ener-

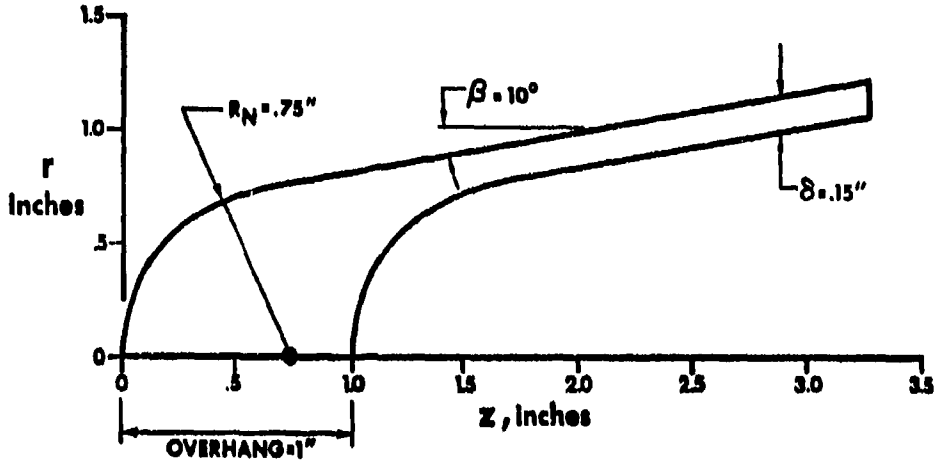

FIGURE 3-12 SHELL NOSETIP GEOMETRY

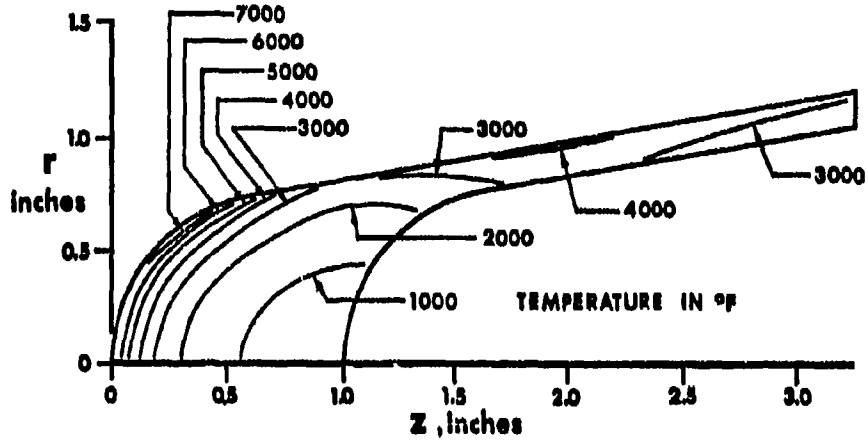

FIGURE 3-13 NOSETIP TEMPERATURE DISTRIBUTION AT t = 1.60 SECONDS

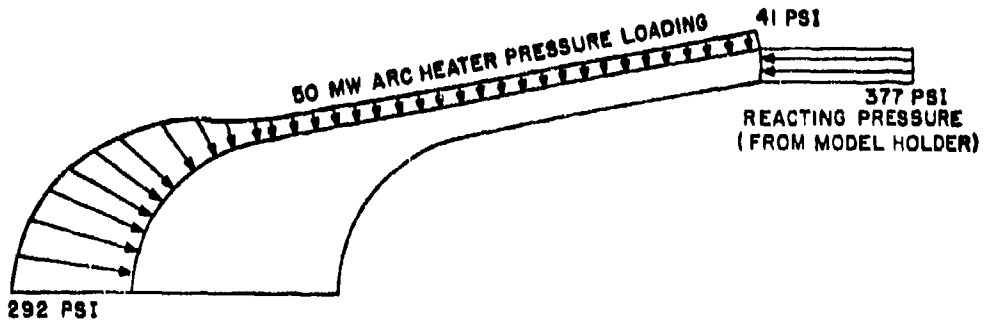

FIGURE 3-14 NOSETIP PRESSURE DISTRIBUTION

gies are high enough that the hump of the stress-strain curve in Fig. 2-18 is passed so the model is unstable. Accordingly, we must use a Jones-Nelson-Morgan model with an extended stress-strain curve that doesn't have a hump and always has positive slope as in Fig. 2-22. A typical stress-strain curve and mechanical property versus energy curve are shown along with experimental data from the SoRI ATJ-S data book [3-1] in Fig. 3-15 and 3-16 for behavior in the radial direction (σ_{r_t} versus ϵ_{r_t} and E_{r_t} versus U) at 70°F under tension loading. The Jones-Nelson-Morgan nonlinear material model parameters are given for all available temperatures in Table 3-6. The associated coefficients of thermal expansion are given in Table 3-7.

The implied slope version of the Jones-Nelson-Morgan model seems to be the most appropriate of those available although the Jones-Nelson-Crose model might be equally applicable. In the implied slope model, the slope at the last data point is arbitrarily used as the subsequent slope of the stress-strain curve. In contrast, the subsequent slope of the Jones-Nelson-Crose model is determined by fitting a straight line through the stress and strain points corresponding to 5% probability of failure and 50% probability of failure. Not having suitable failure data to work with, we chose the simpler Jones-Nelson-Morgan implied slope model. However, the available data are insufficient to apply the implied slope model without approximation. Specifically, the data are available for E_r and E_z in tension and compression for all temperatures but not for E_{rz}^{45}! Thus, we fit the implied slope model to E_r and E_z and observe the corresponding values of A, B, C, U_o, U*, E*, and σ_o for each case. Then, we estimate corresponding values for E_{rz}^{45} based on the relation of E_{rz}^{45} to E_r and E_z at room temperature for Jortner's data [3-8]. Simulta-

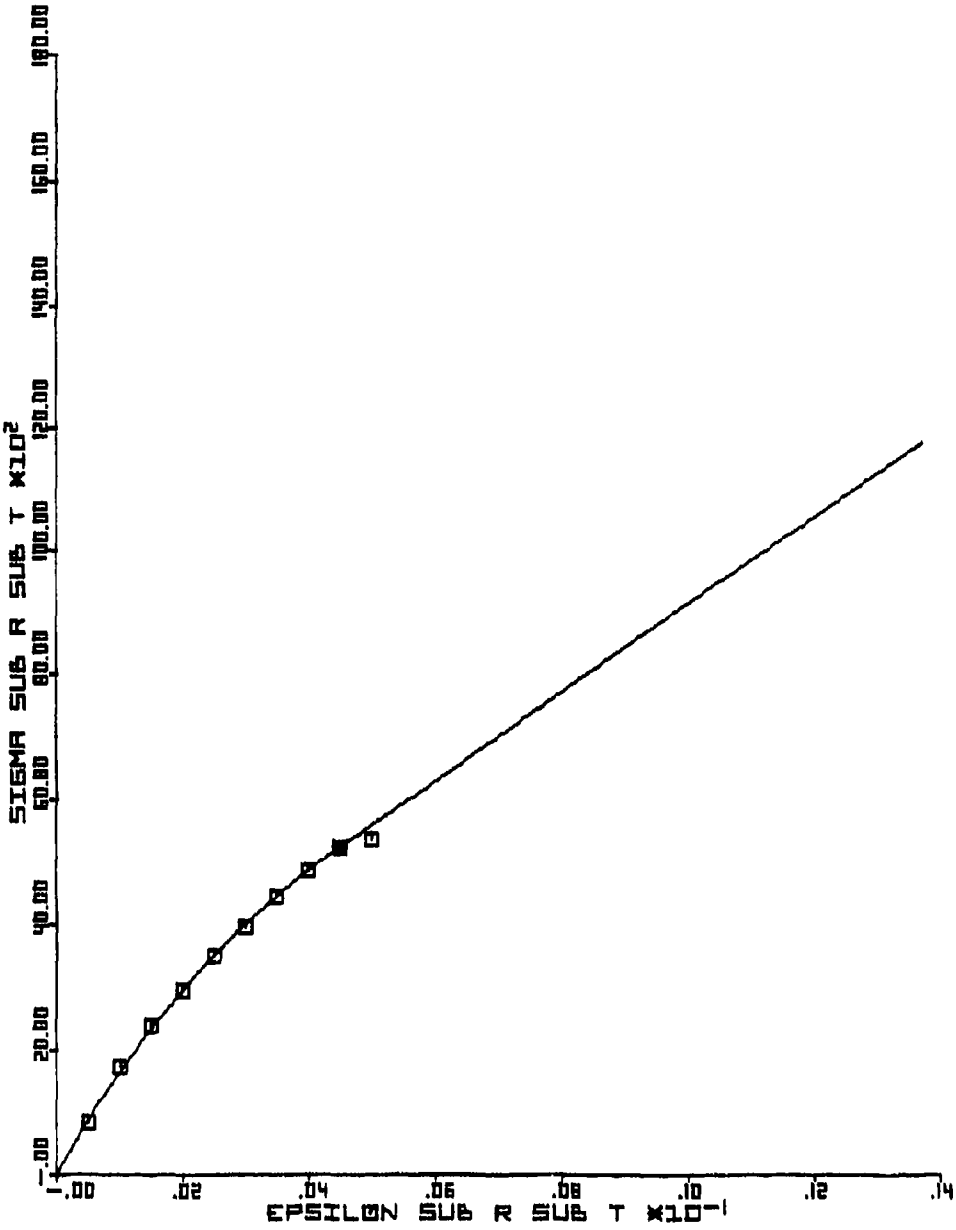

FIGURE 3-15 LINEAR STRESS-STRAIN CURVE EXTRAPOLATION WITH NONZERO SLOPE EQUAL TO SLOPE AT LAST DATA POINT FOR RADIAL DIRECTION BEHAVIOR AT 70°F IN TENSION

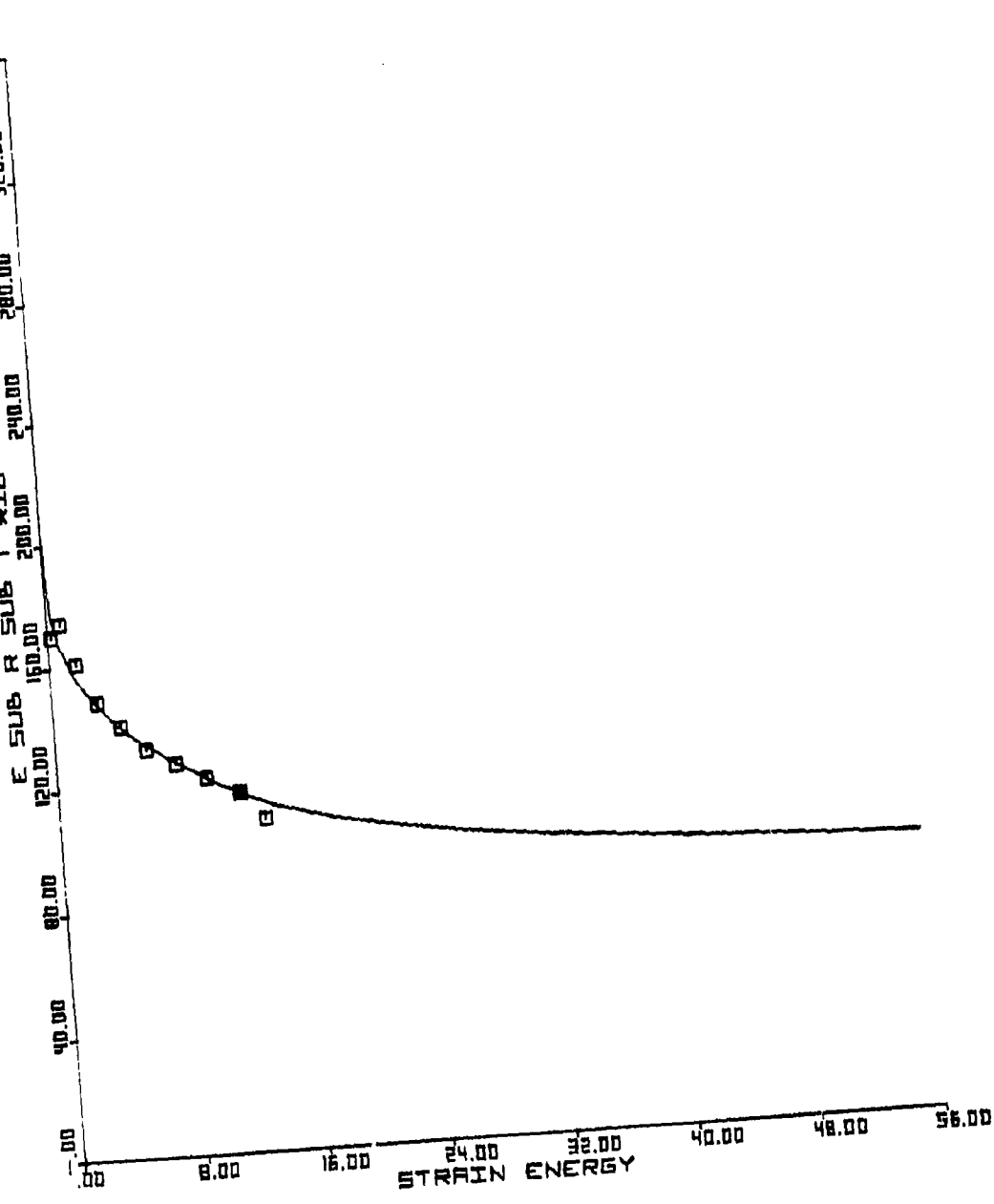

FIGURE 3-16 MECHANICAL PROPERTY VERSUS ENERGY CURVE CORRESPONDING TO THE LINEAR STRESS-STRAIN CURVE EXTRAPOLATION IN FIGURE 3-15 FOR RADIAL DIRECTION BEHAVIOR AT 70° IN TENSION

TABLE 3-6

JONES-NELSON-MORGAN NONLINEAR MATERIAL MODEL PARAMETERS

FOR ATJ-S(WS) GRAPHITE AS A FUNCTION OF TEMPERATURE

TEMPERATURE	MECHANICAL PROPERTY	A	B	C	U* psi	E* 10^6psi	σ_o psi
70°F	E_{r_t}	2.00x10^6psi	.182	.337	11.8	.708	2050
	E_{z_t}	1.50x10^6psi	.226	.322	13.1	.354	2230
	$\nu_{r\theta_t}$	.110	0.	1.	0.	0.	0.
	$\nu_{z\theta_t}$	.090	0.	1.	0.	0.	0.
	$E^{45}_{rz_t}$	1.55x10^6psi	.200	.330	12.1	.480	1950
	E_{r_c}	3.00x10^6psi	.477	.125	37.3	.336	4100
	E_{z_c}	2.10x10^6psi	.451	.134	30.3	.304	3010
	$\nu_{r\theta_c}$	.065	0.	1.	0.	0.	0.
	$\nu_{z\theta_c}$	.065	0.	1.	0.	0.	0.
	$E^{45}_{rz_c}$	2.40x10^6psi	.470	.130	29.7	.310	3230
2000°F	E_{r_t}	2.00x10^6psi	.0651	.583	14.1	.825	2550
	E_{z_t}	1.60x10^6psi	.165	.336	12.3	.645	1710
	$\nu_{r\theta_t}$	.130	0.	1.	0.	0.	0.
	$\nu_{z\theta_t}$	.107	0.	1.	0.	0.	0.
	$E^{45}_{rz_t}$	1.83x10^6psi	.120	.460	11.6	.660	2210
	E_{r_c}	3.00x10^6psi	.333	.203	37.1	.338	5210
	E_{z_c}	1.90x10^6psi	.281	.221	36.0	.337	3830
	$\nu_{r\theta_c}$	.082	0.	1.	0.	0.	0.
	$\nu_{z\theta_c}$	.082	0.	1.	0.	0.	0.
	$E^{45}_{rz_c}$	2.84x10^6psi	.350	.210	24.3	.337	4120

TABLE 3-6, continued

TEMPERATURE	MECHANICAL PROPERTY	A	B	C	U* psi	E* 10^6psi	σ_o psi
3000°F	E_{r_t}	2.10×10^6psi	.0510	.660	19.7	.600	3990
	E_{z_t}	1.45×10^6psi	.0254	.921	16.5	.350	3590
	$\nu_{r\theta_t}$	.140	0.	1.	0.	0.	0.
	$\nu_{z\theta_t}$	.116	0.	1.	0.	0.	0.
	$E^{45}_{rz_t}$	2.11×10^6psi	.0380	.790	19.5	.400	4830
	E_{r_c}	3.60×10^6psi	.350	.198	45.8	.243	6730
	E_{z_c}	1.80×10^6psi	.194	.291	40.2	.350	4360
	$\nu_{r\theta_c}$	.090	0.	1.	0.	0.	0.
	$\nu_{z\theta_c}$	.090	0.	1.	0.	0.	0.
	$E^{45}_{rz_c}$	3.27×10^6psi	.310	.240	29.9	.275	5500
3500°F	E_{r_t}	2.40×10^6psi	.277	.212	70.0	.293	6430
	E_{z_t}	1.40×10^6psi	.133	.395	36.1	.226	4360
	$\nu_{r\theta_t}$	.145	0.	1.	0.	0.	0.
	$\nu_{z\theta_t}$	.120	0.	1.	0.	0.	0.
	$E^{45}_{rz_t}$	2.04×10^6psi	.158	.388	30.0	.232	5090
	E_{r_c}	3.60×10^6psi	.316	.220	41.4	.293	6560
	E_{z_c}	2.00×10^6psi	.158	.347	42.2	.300	5440
	$\nu_{r\theta_c}$	.0950	0.	1.	0.	0.	0.
	$\nu_{z\theta_c}$	.0950	0.	1.	0.	0.	0.
	$E^{45}_{rz_c}$	3.27×10^6psi	.270	.290	24.5	.240	5480

TABLE 3-6, continued

TEMPERATURE	MECHANICAL PROPERTY	A	B	C	U* psi	E* 10^6psi	σ_o psi
4000°F	E_{r_t}	2.70x10^6psi	.282	.237	69.5	.069	8230
	E_{z_t}	1.40x10^6psi	.107	.477	35.2	.115	5140
	$\nu_{r\theta_t}$	.150	0.	1.	0.	0.	0.
	$\nu_{z\theta_t}$	.125	0.	1.	0.	0.	0.
	$E^{45}_{rz_t}$	1.97x10^6psi	.200	.360	30.0	.083	5340
	E_{r_c}	2.80x10^6psi	.323	.212	42.5	.240	5730
	E_{z_c}	1.80x10^6psi	.153	.377	31.7	.267	4640
	$\nu_{r\theta_c}$	.100	0.	1.	0.	0.	0.
	$\nu_{z\theta_c}$	.100	0.	1.	0.	0.	0.
	$E^{45}_{rz_c}$	3.06x10^6psi	.270	.300	20.5	.250	4860
4500°F	E_{r_t}	2.50x10^6psi	.300	.250	46.1	.030	6700
	E_{z_t}	1.30x10^6psi	.100	.500	37.4	.060	5420
	$\nu_{r\theta_t}$	.170	0.	1.	0.	0.	0.
	$\nu_{z\theta_t}$	.150	0.	1.	0.	0.	0.
	$E^{45}_{rz_t}$	1.50x10^6psi	.200	.400	21.6	.035	4190
	E_{r_c}	2.40x10^6psi	.275	.250	38.0	.227	5330
	E_{z_c}	1.80x10^6psi	.244	.267	33.8	.260	4160
	$\nu_{r\theta_c}$	.150	0.	1.	0.	0.	0.
	$\nu_{z\theta_c}$	.150	0.	1.	0.	0.	0.
	$E^{45}_{rz_c}$	2.40x10^6psi	.300	.270	20.1	.220	4030

TABLE 3-6, concluded

TEMPERATURE	MECHANICAL PROPERTY	A	B	C	U* psi	E* 10^6psi	σ_o psi
5000°F	E_{r_t}	2.00x10^6psi	.300	.250	46.8	.020	6050
	E_{z_t}	1.20x10^6psi	.100	.500	39.2	.040	5400
	$\nu_{r\theta_t}$	.200	0.	1.	0.	0.	0.
	$\nu_{z\theta_t}$	.170	0.	1.	0.	0.	0.
	$E^{45}_{rz_t}$	1.40x10^6psi	.200	.400	22.1	.025	4130
	E_{r_c}	2.00x10^6psi	.301	.237	31.8	.208	4280
	E_{z_c}	1.80x10^6psi	.408	.170	26.1	.214	3070
	$\nu_{r\theta_c}$	.200	0.	1.	0.	0.	0.
	$\nu_{z\theta_c}$	.200	0.	1.	0.	0.	0.
	$E^{45}_{rz_c}$	1.74x10^6psi	.410	.210	11.3	.210	2190

TABLE 3-7

COEFFICIENTS OF THERMAL EXPANSION FOR ATJ-S(WS) GRAPHITE

AS A FUNCTION OF TEMPERATURE

TEMPERATURE °F	α_r 10^{-5} per °F	α_z 10^{-5} per °F
70	.1200	.1720
2000	.1915	.2471
3000	.2194	.2727
3500	.2315	.2864
4000	.2414	.2997
4500	.2547	.3174
5000	.2685	.3384

neously, we use the constant values for the Poisson's ratios given in the SoRI ATJ-S graphite data book [3-1]. All of the foregoing modeling is performed with the invaluable aid of the JNMDATA program described in Section 2.4.

3.2.2.2 Elastic Stress and Strain Predictions

The elastic stresses and strains are predicted with the SAAS IIIM finite element stress analysis computer program which is a Jones-Nelson-Morgan model version of the SAAS III program [3-9]. Elastic predictions are obtained in the first iteration of the Jones-Nelson-Morgan model. Specifically, the stresses and strains are predicted with the elastic mechanical properties, i.e., the values of A in Eq. (2.3) and Table 3-6. The finite element mesh is composed of 398 elements with 454 nodal points as shown in Fig. 3-17. Some element numbers of special interest in subsequent discussions are labeled.

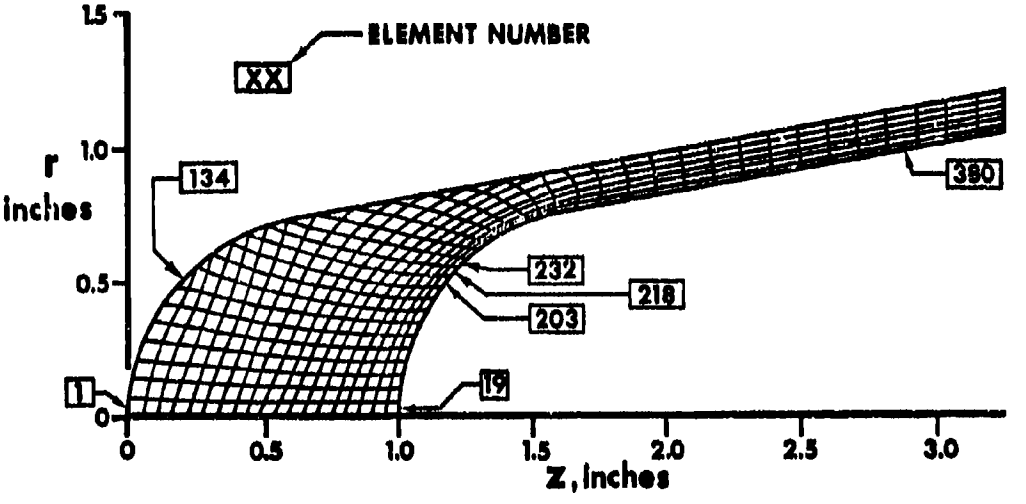

FIGURE 3-17 NOSETIP FINITE ELEMENT MESH

The elastic predictions with the Jones-Nelson-Morgan model are different from elastic predictions with any other commonly used material model. This situation occurs because the actual high initial slopes are more closely approximated with the Jones-Nelson-Morgan model than by "eye-ball" from a stress-strain curve. Thus, comparison of predicted elastic stresses and strains with other results may not be fruitful. At any rate, the elastic strains ε_r, ε_θ, ε_z, γ_{rz}, and ε_{max} are displayed in contour plot form in Figs. 3-18 through 3-22.

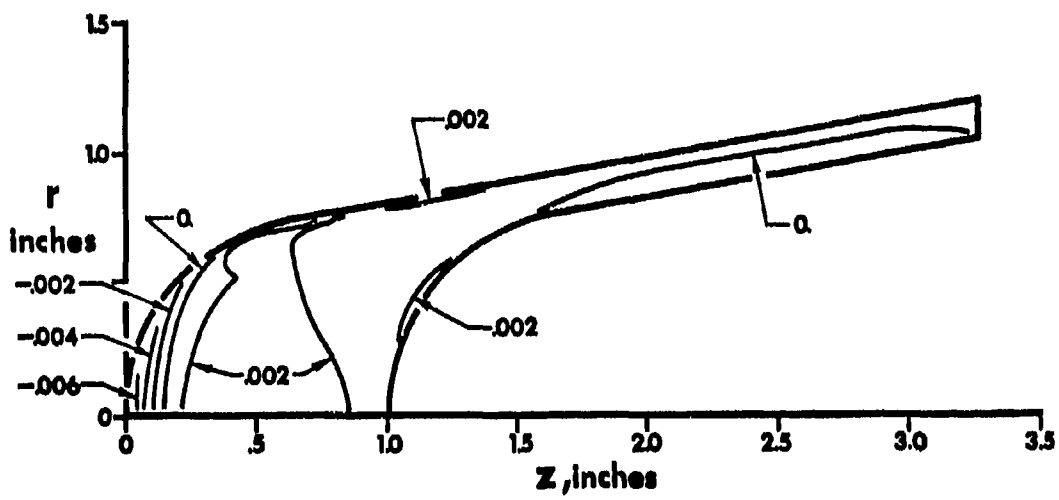

FIGURE 3-18 ε_r — ELASTIC

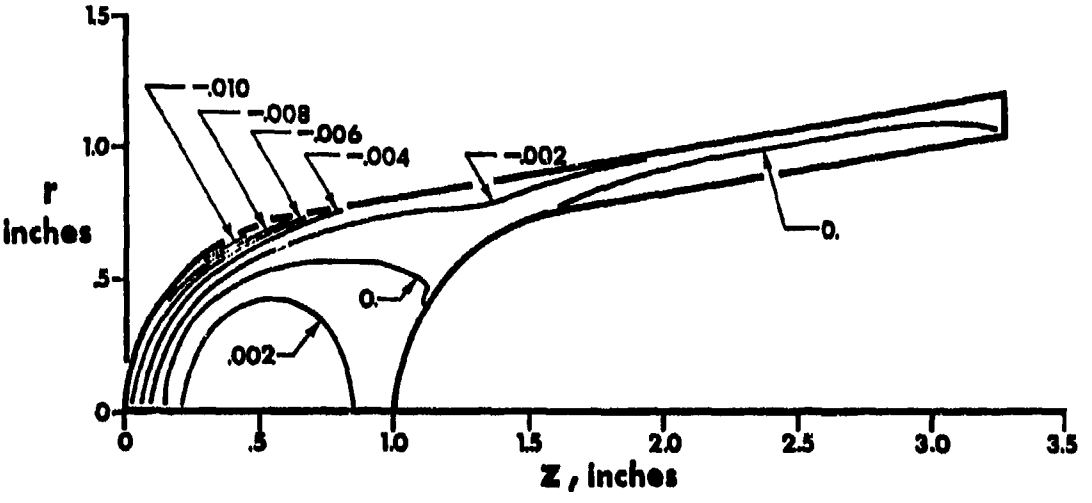

FIGURE 3-19 ε_θ — ELASTIC

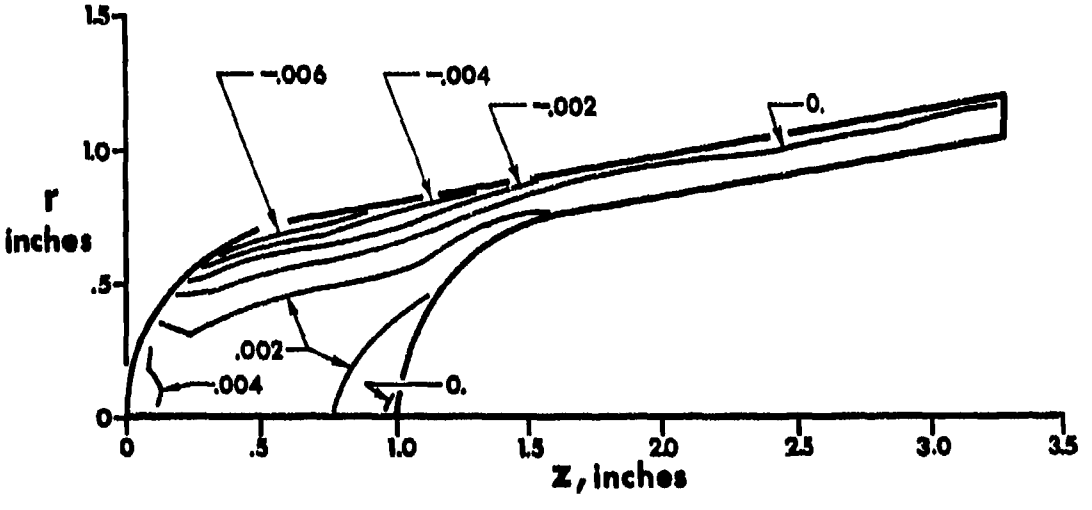

FIGURE 3-20 ε_z — ELASTIC

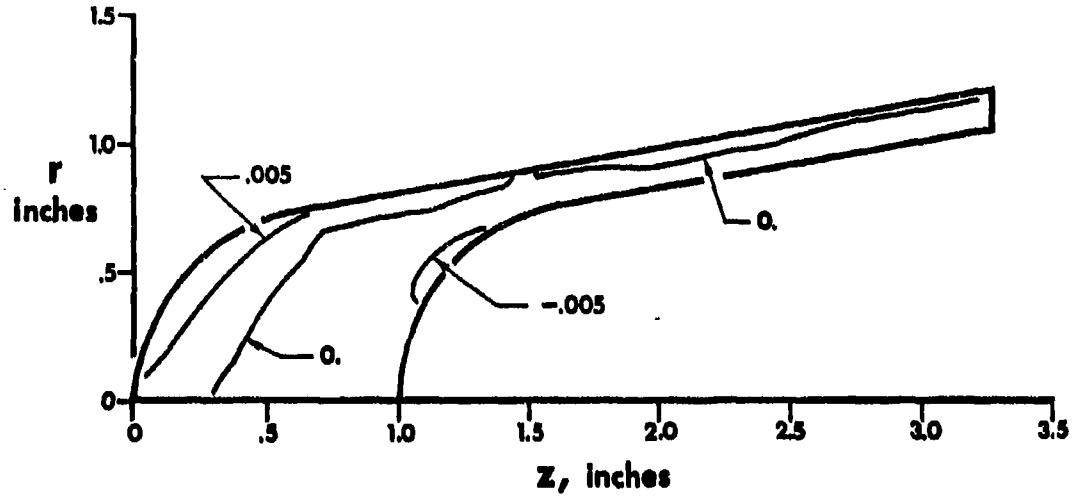

FIGURE 3-21 γ_{rz} — ELASTIC

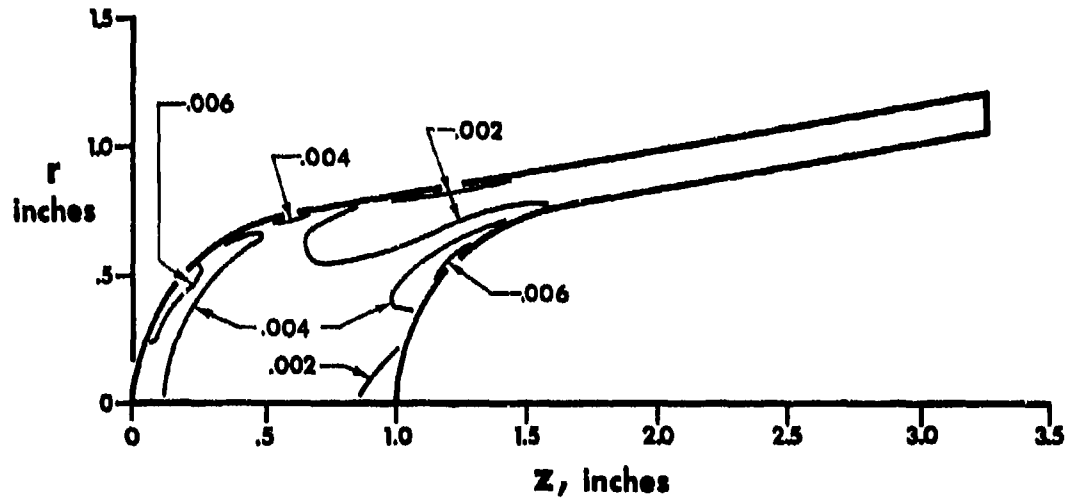

FIGURE 3-22 ε_{max} — ELASTIC

3.2.2.3 Nonlinear Stress and Strain Predictions

The nonlinear stresses and strains are obtained by iteration of the SAAS IIIM program until the energies in all finite elements do not change more than a specified small percentage (in this case $\frac{1}{2}\%$). These stresses and strains are what is predicted to actually exist in the nosetip under the prescribed environment. Thus, they are the values which will be compared with the DOASIS predictions in Section 3.2.3. At this point, we only display contour plots of the nonlinear strains ε_r, ε_θ, ε_z, γ_{rz}, and ε_{max} in Figs. 3-23 through 3-27.

The results depicted in Figs. 3-23 through 3-27 are obtained after nine iterations of the SAAS IIIM computer program. The rate of convergence is studied for two specific finite elements: element 232 along the inner contour of the nosetip in Fig. 3-17 and element 134 in the hottest region on the outside contour of the nosetip. Values of repre-

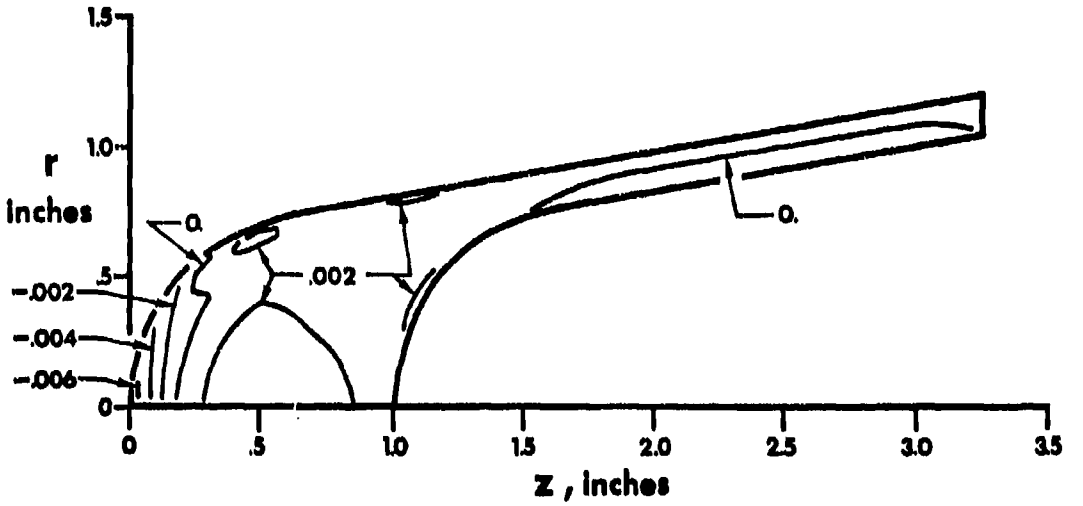

FIGURE 3-23 ε_r — NONLINEAR

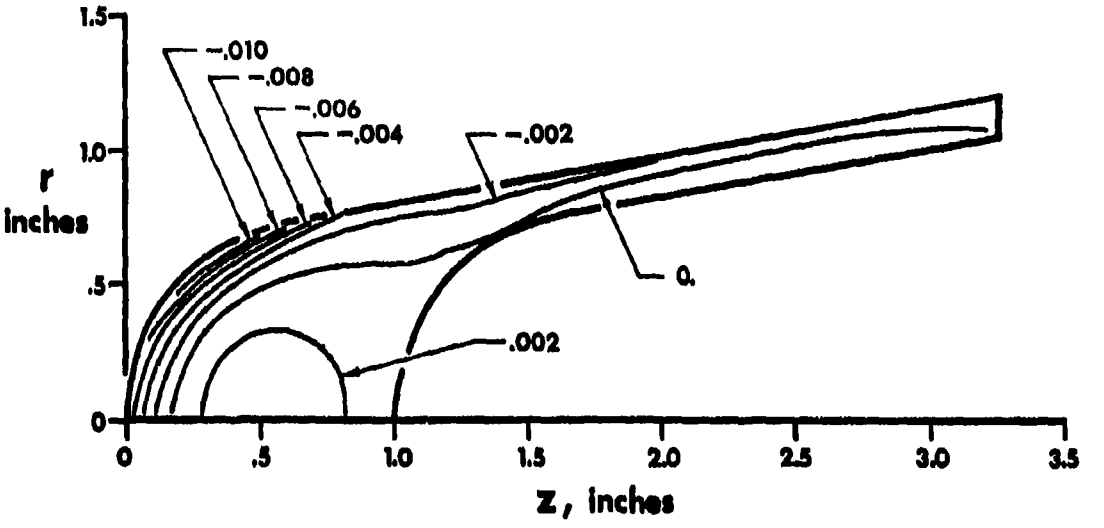

FIGURE 3-24 ε_θ — NONLINEAR

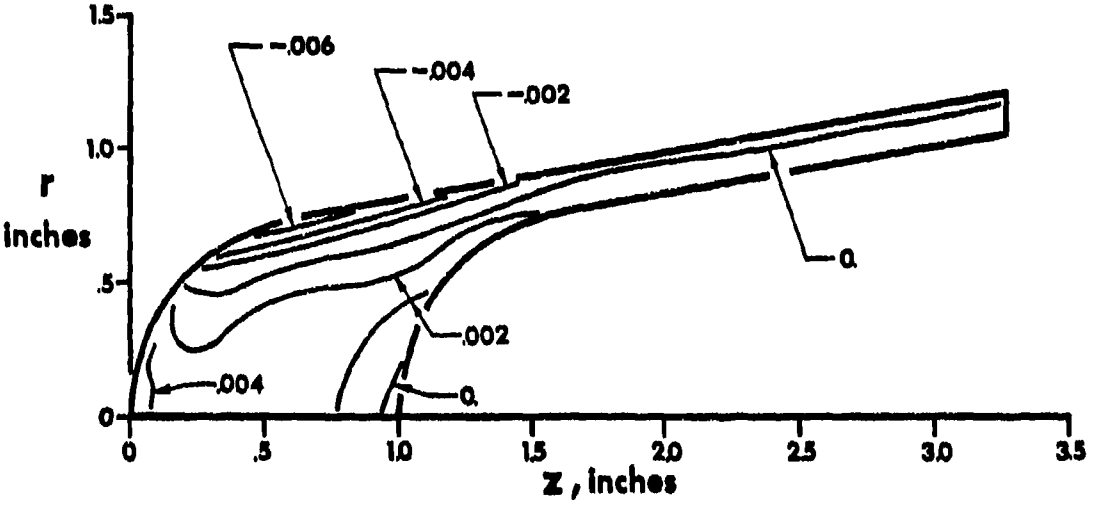

FIGURE 3-25 ε_z — NONLINEAR

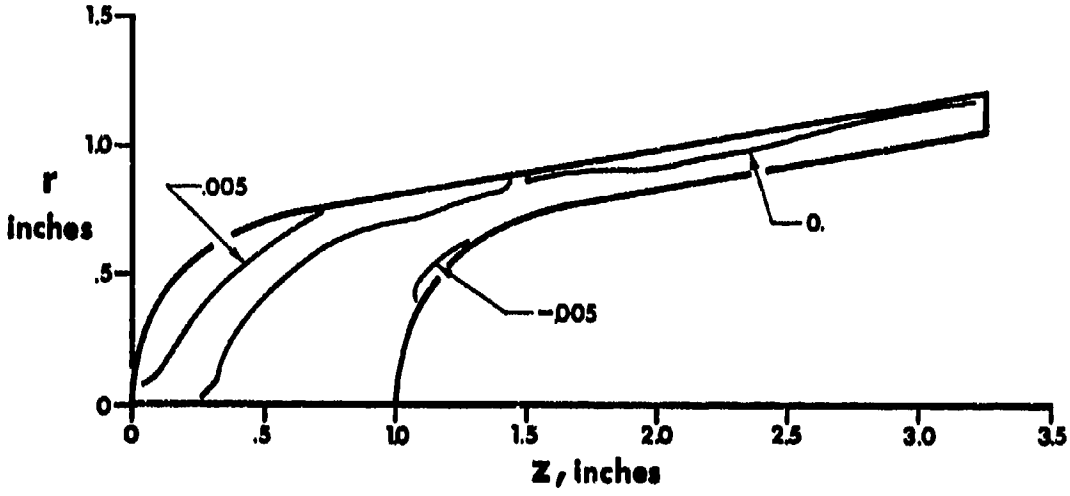

FIGURE 3-26 γ_{rz} — NONLINEAR

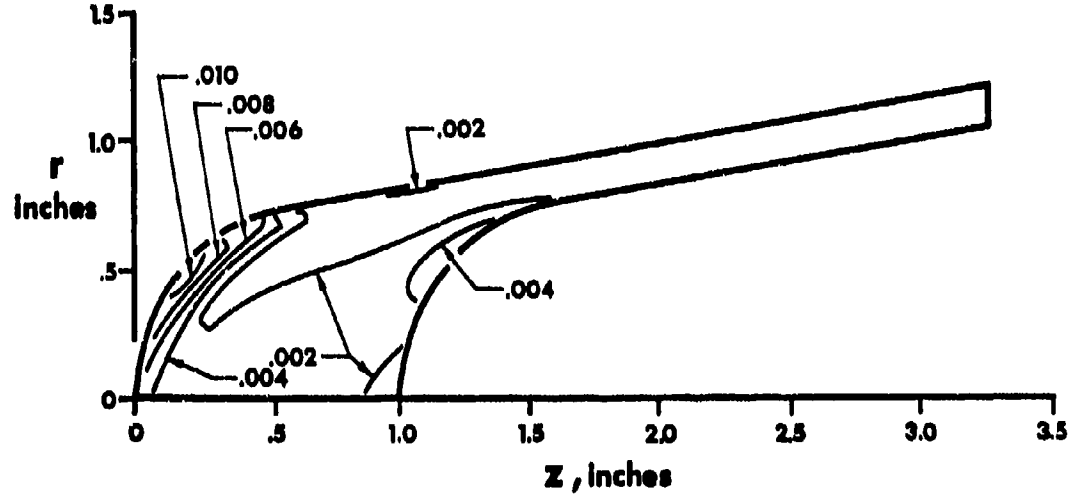

FIGURE 3-27 ε_{max} — NONLINEAR

sentative stresses and strains are listed in Tables 3-8 and 3-9 for the two elements.

The stresses and strains for element 232 in Table 3-8 appear to have converged in five iterations for all practical purposes. This rapid convergence occurs because the stress-strain behavior at a temperature of 1397°F is not highly nonlinear. A reasonable question is why are results obtained for nine iterations instead of stopping at five (or six) iterations? The answer is related to the fact that convergence is achieved in the SAAS IIIM program only when every single element has a strain energy change of less than 1/2% from the energy in the previous iteration. Thus, we would expect to find other finite elements for which the convergence is slower than it is for element 232. Brute force of tediously examining the convergence in all elements is presently the only way to determine the elements for which convergence is slowest. However, some good estimates can be made as to which elements might have slower convergence than element 232. For example, consider element 134 on the outer nosetip contour in Fig. 3-17. The temperature there is very high (7768°F), and hence the stress-strain behavior is very nonlinear. In fact, we can only approximate the stress-strain behavior for such high temperatures. The convergence of the stresses and strains for element 134 in Table 3-9 is much slower than for element 232. The stresses and strains are not quite different enough in the last few iterations to be the governing factors in the overall nosetip iteration procedure. However, we need only be assured that elements exist for which convergence is slower than for element 232 to justify having more than five or six iterations in a nosetip stress analysis.

TABLE 3-8

PREDICTED STRESSES AND STRAINS IN ELEMENT 232

ITERATION	σ_r,psi	σ_z,psi	ε_r	ε_z	ε_{max}
1	4950	5879	.00203	.00335	.00611
2	2359	2775	.00163	.00321	.00590
3	2798	3300	.00166	.00331	.00601
4	2674	3149	.00166	.00329	.00599
5	2705	3188	.00166	.00330	.00600
6	2697	3177	.00166	.00329	.00600
7	2699	3180	.00166	.00330	.00600
8	2699	3179	.00166	.00330	.00600
9	2699	3180	.00166	.00330	.00600

TABLE 3-9

PREDICTED STRESSES AND STRAINS IN ELEMENT 134

ITERATION	σ_r,psi	σ_z,psi	σ_θ,psi	σ_{min},psi	ε_{min}
1	-11363	-9235	-25737	-19857	-.01071
2	-1780	-1549	-4305	-3900	-.01275
3	-2842	-2728	-7225	-5698	-.01370
4	-2460	-2251	-5916	-4966	-.01349
5	-2580	-2402	-6321	-5199	-.01358
6	-2538	-2348	-6178	-5116	-.01355
7	-2553	-2367	-6227	-5145	-.01356
8	-2547	-2360	-6210	-5134	-.01356
9	-2549	-2362	-6216	-5138	-.01356

3.2.3 COMPARISON OF JONES-NELSON-MORGAN AND DOASIS STRESS AND STRAIN PREDICTIONS

The elastic and nonlinear strains plotted in contour form in Figs. 3-18 through 3-27 are quite similar in appearance to corresponding DOASIS results obtained by Baker, Starrett, and Budde [3-12]. The only apparent differences are somewhat higher strains for SAAS IIIM than for DOASIS and a difference in sign for γ_{rz}.

The SAAS IIIM sign convention for shear stress and shear strain is opposite to that in DOASIS. This difference was noted after the rather expensive computer runs were made so the wrong contours were requested for SAAS IIIM. That is, a request for the same contours as plotted from DOASIS resulted in only those contours which were common to both sign conventions. For example, γ_{rz} contours .005, 0., -.005, -.010, and -.015 were requested, but in the SAAS IIIM sign convention only .015, .010, .005, 0., and -.005 exist in the results. Thus, only results for .005, 0., and -.005 are plotted. Contours for .010 and .015 do exist as is easily verified by inspection of the computer output listings, but simply are not plotted. These comments apply to both the elastic γ_{rz} in Fig. 3-21 and to the nonlinear γ_{rz} in Fig. 3-26.

The higher SAAS IIIM strains in Figs 3-18 through 3-27 than DOASIS strains [3-12] are more easily quantified if we examine the strains for a specific element. We choose element number 232 on the inside surface in Fig. 3-17. This element has the highest predicted maximum strain in the cool region of the nosetip and is the element about which a clip-on extensometer is centered in the 50 MW tests. The SAAS IIIM elastic stresses for element 232 are seen in Table 3-10 to be nearly 50% higher than the DOASIS stresses. Moreover, the SAAS IIIM strains in Table 3-11

TABLE 3-10

ELASTIC STRESSES IN ELEMENT 232

CALCULATED WITH DOASIS AND SAAS IIIM

STRESS	DOASIS psi	SAAS IIIM psi	Δ
σ_r	3,429	4,950	+44%
σ_θ	1,257	1,112	-12%
σ_z	4,023	5,879	+46%
τ_{rz}	3,579	-5,210	+46%
σ_{max}	7,316	10,645	+46%

TABLE 3-11

ELASTIC STRAINS IN ELEMENT 232

CALCULATED WITH DOASIS AND SAAS IIIM

STRAIN	DOASIS	SAAS IIIM	Δ
ε_r	.00157	.00203	+29%
ε_θ	.00014	-.00013	-7%
ε_z	.00297	.00335	+13%
γ_{rz}	.00582	-.00671	+15%
ε_{max}	.00526	.00611	+16%

are 15 to 30% higher than the DOASIS strains. However, comparison of these two elastic predictions is not entirely valid because the SAAS IIIM elastic properties are much higher than the DOASIS elastic properties (higher elastic properties than in conventional analyses is characteristic of the Jones-Nelson and Jones-Nelson-Morgan nonlinear material models as noted in Section 2.2.2). Thus, we do not make an issue of the lack of comparison of SAAS IIIM and DOASIS elastic results because they should not be the same.

However, the SAAS IIIM and DOASIS nonlinear stresses and strains are comparable. In Table 3-12, we see that the SAAS IIIM nonlinear stresses are about 13% lower than the DOASIS nonlinear stresses. At the same time, the SAAS IIIM nonlinear strains in Table 3-13 are nearly 20% higher than the DOASIS nonlinear strains in element 232. The significance of this latter conclusion will be revealed in Section 3.2.4.

The linear and nonlinear σ_r-ε_r and σ_z-ε_z results are shown for element 232 from both the DOASIS program and the SAAS IIIM program with the Jones-Nelson-Morgan (JNM) material model in Fig. 3-28. There, the DOASIS uniaxial bilinear stress-strain curves are plotted with a medium solid line (and the extension of the elastic slope is shown with a long dash - short dash line). Also, the actual nonlinear stress-strain curves are shown with a heavy line along with the elastic slope (the tangent to the stress-strain curve at σ=0) as a dashed line. The DOASIS elastic results are plotted as a circle which lies to the left of the elastic uniaxial stress-strain curve because of Poisson effects in the multiaxial stress state. The DOASIS nonlinear results are plotted as a dot which is similarly to the left of the uniaxial stress-strain curve. The JNM elastic multiaxial results are shown as open squares and are to the left

TABLE 3-12

NONLINEAR STRESSES IN ELEMENT 232

CALCULATED WITH DOASIS AND SAAS IIIM

STRESS	DOASIS psi	SAAS IIIM psi	Δ
σ_r	3,133	2,699	-14%
σ_θ	1,647	1,327	-19%
σ_z	3,666	3,180	-13%
τ_{rz}	3,257	-2,821	-13%
σ_{max}	6,667	5,771	-13%

TABLE 3-13

NONLINEAR STRAINS IN ELEMENT 232

CALCULATED WITH DOASIS AND SAAS IIIM

STRAIN	DOASIS	SAAS IIIM	Δ
ε_r	.00140	.00166	+19%
ε_θ	.00026	.00042	+62%
ε_z	.00284	.00330	+16%
γ_{rz}	.00576	-.00685	+19%
ε_{max}	.00509	.00600	+18%

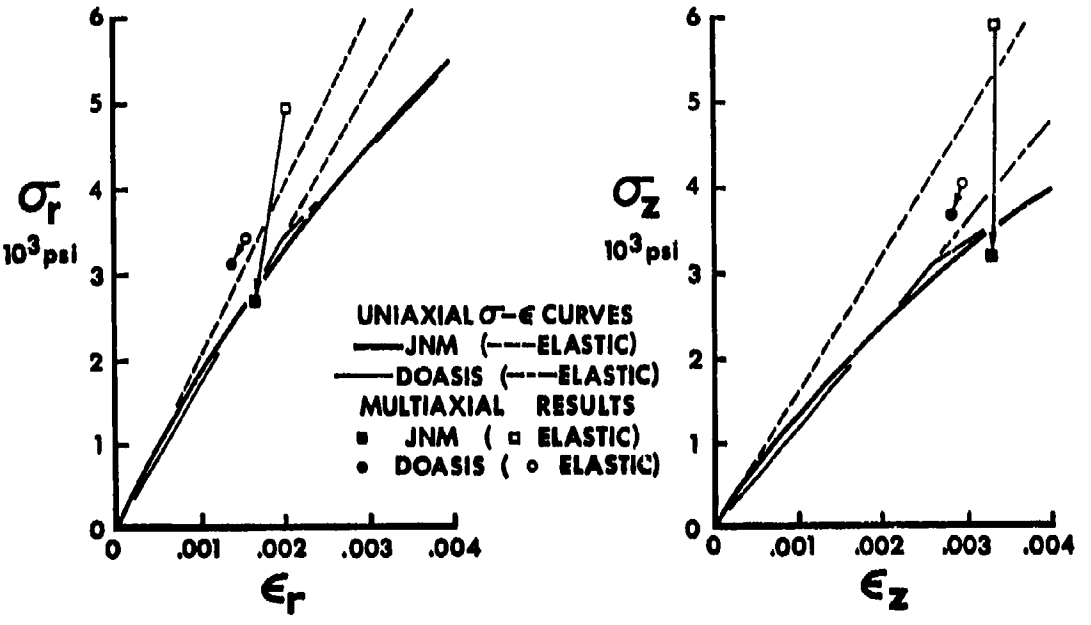

FIGURE 3-28 LINEAR VS. NONLINEAR BEHAVIOR AT NOSETIP EL. 232

of the elastic uniaxial stress-strain curve. Finally, the JNM nonlinear multiaxial results are shown as solid squares and are to the right of the actual nonlinear stress-strain curve as is typical of graphitic materials with biaxial softening. Obviously, the JNM linear and nonlinear results are drastically different from each other even for the relatively modest nonlinear behavior at this temperature. More drastic differences between linear and nonlinear results exist for elements in hotter and hence more nonlinear regions of the nosetip. Note that the elastic strains are larger than the nonlinear strains for this element. In contrast, the elastic strains are less than the nonlinear strains for element 134 in a hotter region of the nosetip. These two results are similar to the results for the inside and outside elements in the SoRI thermal stress disk test analysis. That is, sometimes the elastic strains are higher than the non-

linear strains and sometimes they are lower.

The DOASIS results were obtained in ten iterations in contrast to the nine iterations required for the same problem in SAAS IIIM. No claim is made that SAAS IIIM is "faster" than DOASIS on the basis of the observed one less iteration. As a matter of fact, DOASIS is probably faster for this nosetip problem because DOASIS is faster per iteration than SAAS IIIM. The meaningful comparative measure is the accuracy of the results, and this issue will be addressed in the next section.

3.2.4 SUMMARY OF 50 MW NOSETIP STRESS ANALYSIS

The objective of this 50 MW nosetip stress analysis is to compare the JNM model results with those obtained with the DOASIS computer program. That comparison is made in Section 3.2.3 where the JNM model strains are seen to be about 20% greater than the DOASIS nonlinear strains in element 232 about which the extensometer in the 50 MW tests is centered. The scope of this contract does not include a correlation of JNM model predictions with the actual 50 MW nosetip strain measurements. However, a cursory correlation will be performed to put the JNM model predictions into some perspective.

The elongation between two points on the nosetip inside contour was measured in the 50 MW tests in order to estimate the strain tangent to the inside contour. This elongation between nodal points 199 and 304 was measured with an extensometer centered about element 232 in Fig. 3-17. For run R41-016, the elongation was .0028 inches [3-12]. The mechanical strain is obtained by dividing the elongation by the gage length of .36 inches and subtracting $\alpha\Delta T$ = .0031. The resulting mechanical strain is .0047. The maximum mechanical strain in element 232 is predicted to be .0051 (Baker, Starrett and Budde report .0038, but .0051 appears in the

DOASIS output provided to SMU by Captain Budde) with DOASIS and .0060 with SAAS IIIM. However, the maximum mechanical strain in element 232 is not tangent to the inner contour of the nosetip. This fact is readily observed when we realize that, although principal stress direction is tangent to the inner contour because the shear stress is zero at the inner contour, the principal strain direction (ε_{max}) is not necessarily in the same direction. That is, for orthotropic materials in nonprincipal material directions (i.e., not in the present r-θ-z principal material coordinates), principal stress directions do <u>not</u> coincide with principal strain directions! The tangent to the inner contour is at 47.7° to the r-direction. Also, the angle to the maximum principal stress is 47.4° (47.3° in DOASIS), but the angle to the maximum principal strain is 51.7° (52.0° in DOASIS). A strain transformation relation for the correct angle could be used, but a more direct comparison is available - compare the predicted elongations themselves.

The elongation between elements 199 and 304 is predicted with the SAAS IIIM program to be .0033 inches and with DOASIS to be .0030 inches. Both values are obtained from the equation

$$\Delta L = L_{final} - L_{initial}$$

where

$$L_{final} = \left\{[(R + u_r)_{304} - (R + u_r)_{199}]^2 + [Z + u_z)_{304} - (Z + u_z)_{199}]^2\right\}^{1/2}$$

$$L_{initial} = [(R_{304} - R_{199})^2 + (Z_{304} - Z_{199})^2]^{1/2}$$

Both the DOASIS and JNM model elongation predictions are higher than the measured value. On the other hand, the DOASIS ε_{max} prediction reported

by Baker, Starrett, and Budde [3-12] is less than the estimated measured ε_{max} whereas the JNM model ε_{max} prediction is greater than the estimated measured value. One reason for the strain differences might be the fact that the temperature of 1600°F used by Baker, Starrett, and Budde is higher than the element temperature of 1397°F used in the analysis. The extensometer is exposed only to the temperature at the inner contour of the nosetip. Thus, the extensometer temperature should be less than the adjacent element temperature. A lower temperature would lead to a lower $\alpha\Delta T$ in the estimated measured ε_{max} calculation and hence to a higher ε_{max}. These kinds of speculations and questions can be cleared up only with a detailed correlation study (which, as mentioned before, is not the objective of the current contract).

Basically, the Jones-Nelson-Morgan model nosetip predictions are higher in strains and lower in stresses than the DOASIS predictions. The key elements of difference are the manner of representation of uniaxial stress-strain curve behavior and the manner in which uniaxial stress-strain curves are used to obtain stresses and strains under multiaxial loading. The correctness of approximation for both models can be measured only by meaningful comparison with experimental results. How the Jones-Nelson-Morgan material model has been applied in such a comparison with experiment is described in the next section.

3.3 SUMMARY OF GRAPHITIC MATERIAL MODELING

The Jones-Nelson-Morgan nonlinear material model has been validated in a meaningful hierarchy of comparisons with experimental results. First, the basic mechanical property versus energy equations are curve-fit to data from uniaxial tests in principal material directions. In this fashion, the basic model is defined. The model is then validated by compari-

son of predicted and measured strains under the following loading conditions:

(1) uniaxial mechanical loading in other than principal material directions [3-3, 3-6, 3-14].

(2) biaxial mechanical loading in principal material directions [3-2, 3-6, 3-14].

(3) biaxial thermal loading in principal material directions (Section 3.1).

(4) multiaxial thermal and mechanical loading in other than principal material directions (Section 3.2).

The predicted and measured strains or deformations were in very good to excellent agreement in the first three loading conditions. The agreement was not particularly good for the nosetip problem in condition four, but a meaningful correlation of the data was out of scope of the contract so only cursory results are available. A more complete effort to correlate the nosetip results should be made. Then, the graphite thermal and mechanical stress analysis problem for nosetips would be well under control because of this modeling work and the failure stress and failure strain work of Crose [3-15] and Batdorf [3-16]. The latter efforts depend on the present modeling efforts because of the need for accurate nonlinear stresses and/or strains.

4. MODELING OF CARBON-CARBON MATERIALS

4.1 INTRODUCTION

The nonlinear modeling work for carbon-carbon materials was initiated with this contract. However, only a few solid accomplishments were achieved within the time and funding constraints. These results are reported in this section in the following order. First, the basic characteristics of carbon-carbon are reviewed and examined relative to their importance for nonlinear material modeling in Section 4.2. Then, the flexural modulus and strength studies for multimodulus materials are discussed in Section 4.3. Finally, the essential future modeling work is described in Section 4.4.

4.2 CHARACTERISTICS OF CARBON-CARBON

Carbon-carbon is not a single material, but is instead a broad class of materials. Many types of carbon-carbon are manufactured including various kinds of woven fibers or felt materials both of which are coated or impregnated with a matrix material in a vapor deposition process or a pressure impregnation process.

The steps in a typical pressure impregnation process are illustrated in Fig. 4-1. In the first step, woven graphite fabric in the horizontal plane is pierced with metal rods in the vertical direction while being built up layer by layer in the vertical direction. Next, the metal rods are replaced with graphite yarn or graphite fibers. This somewhat loose assembly of layers is impregnated with phenolic resin in step three. The impregnation process takes place first by evacuation of the chamber in which the material is located and then by pressurization to force the phenolic resin into the voids of the woven and pierced fabric. Then, in

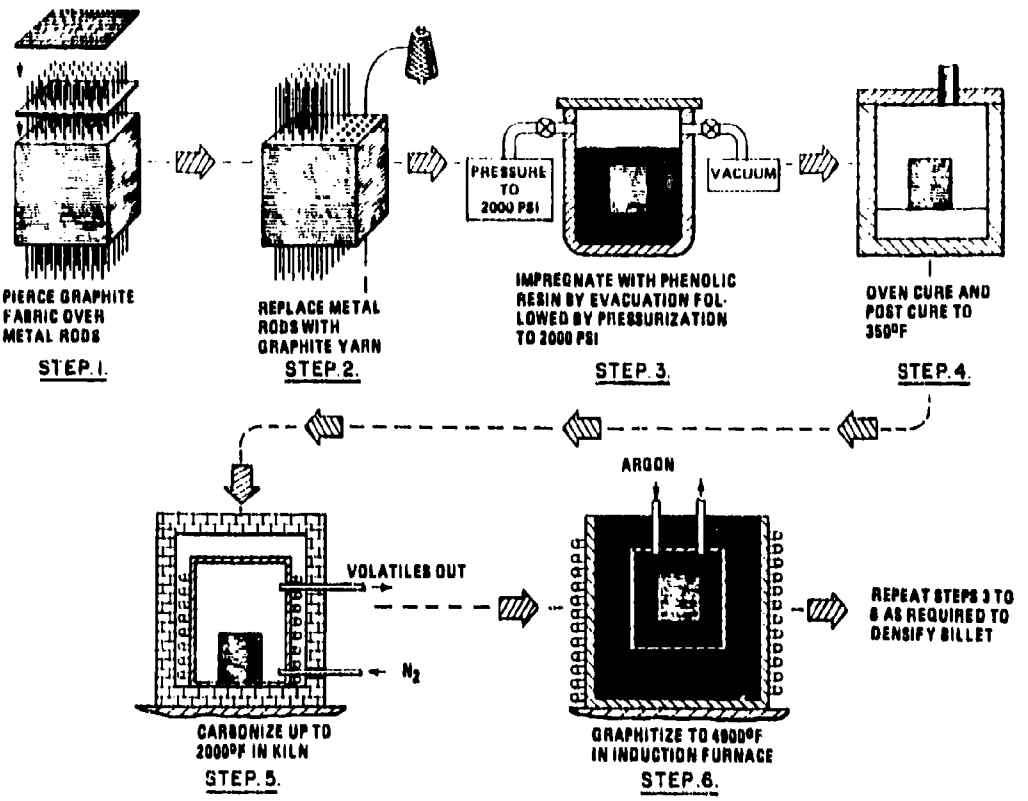

FIGURE 4-1 MOD-3 FABRICATION PROCESS

step four, the material is cured in an oven at 350°F. Next, the material is carbonized at 2000°F in a kiln in step five. Finally, the material is graphitized to 4900°F in an induction furnace in step six. At this stage, the billet of carbon-carbon does not have the degree of density possible, i.e., not all the voids are filled with a graphitized form of the phenolic resin. Accordingly, steps three through six are repeated until the desired density is attained.

Carbon-carbon is made with several different geometries. Each of the layers in Fig. 4-1 can be either woven in the horizontal (x-y) plane as in Fig. 4-2a or made of parallel fibers as in Fig. 4-2b. Avco 3D is of parallel fiber construction and is shown schematically in Fig. 4-3.

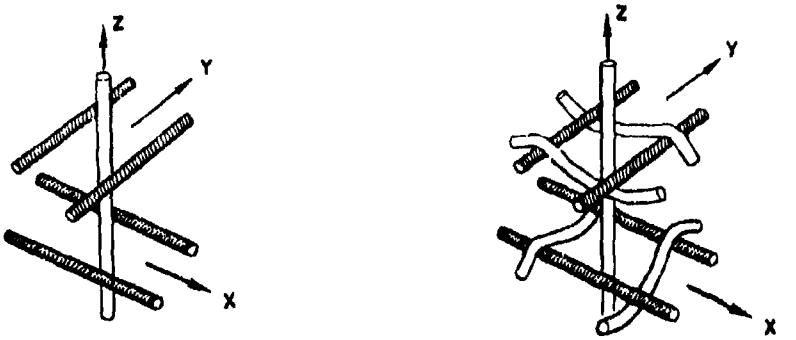

a. ORTHOGONALLY REINFORCED PARALLEL YARNS

b. ORTHOGONALLY REINFORCED WOVEN FABRIC

FIGURE 4-2 GEOMETRY OF LAYERS IN x-y PLANE

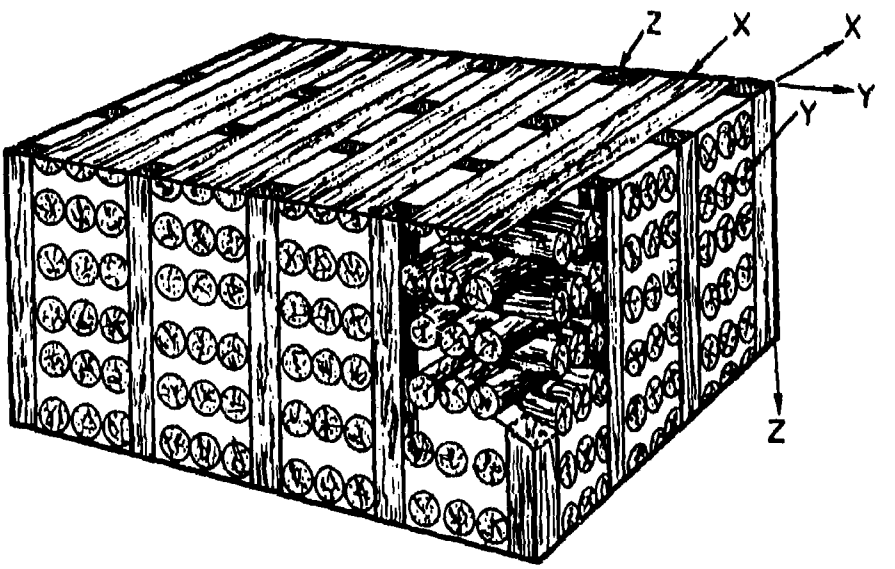

FIGURE 4-3 AVCO 3D CONSTRUCTION

One variation on a three-dimensional weave or three-dimensional construction of orthogonal fibers is to add fibers at 45° angles to the x-, y-, and z-directions. The resulting "7D" construction is shown schematically in Fig. 4-4 for fibers with prismatic cross sections. A much simpler

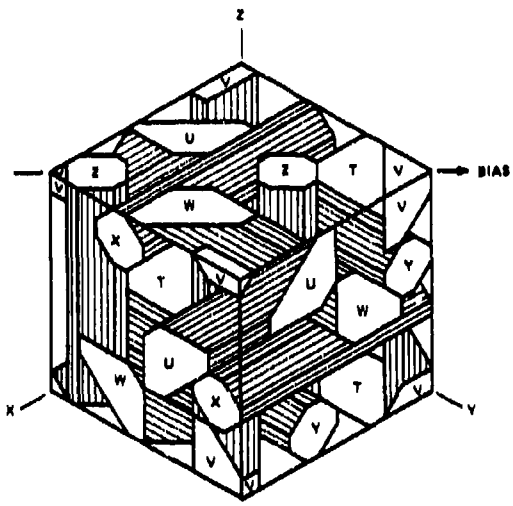

FIGURE 4-4 PACKING MODEL OF PRISMS HAVING EQUAL CROSS SECTIONAL AREA IN 7-D CUBIC GEOMETRY

carbon-carbon structure is obtained after carbon vapor deposition on carbonized felt. The fibers of uncarbonized felt are shown in the scanning electron photomicrograph in Fig. 4-5 where obviously the fibers have no preferred orientation. The scale of all these possible carbon-carbon constructions is revealed in Fig. 4-6 where the approximate fiber spacings in 7-D carbon-carbon are shown in a nosetip. Obviously, the microscale of carbon-carbon materials is not negligible in comparison to the nosetip dimensions. Generally, the microscale dimensions of graphite, namely the particle size, etc., are negligible for nosetip stress analysis problems. However, the characteristic material dimensions of carbon-

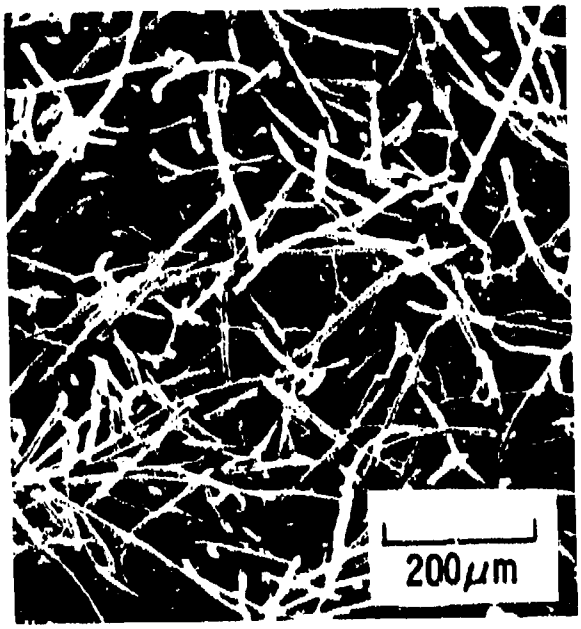

FIGURE 4-5 UNCARBONIZED VISCOSE-RAYON FELT

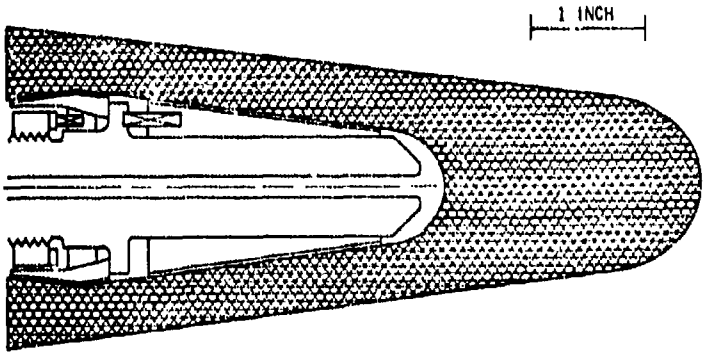

FIGURE 4-6 7-U CARBON-CARBON NOSETIP WITH REPRESENTATIVE FIBER SPACINGS

carbon are not clearly negligible for nosetip problems although perhaps the answer to this question is dependent on the specific carbon-carbon material to be considered.

The anisotropy of the various carbon-carbon materials depends primarily on the geometry of the fiber construction and secondarily on the manner of incorporating a carbon matrix. For example, the orthogonally reinforced carbon-carbons with parallel fibers such as AVCO 3D (Figs. 4-2a and 4-3) and with woven fabric such as AVCO MOD-3 (Fig. 4-2b) are orthotropic with principal material directions in the three fiber directions. In contrast, GE 7-D is not only orthogonally reinforced, but also has fibers at 45° to the x-, y-, and z-directions in which the orthogonal fibers are placed. Accordingly, GE 7-D is anisotropic (although with so many fiber directions, the degree of anisotropy for GE 7-D is lower than the degree of orthotropy for AVCO 3D, i.e., GE 7-D is more like an isotropic material than is AVCO 3D). The manner of incorporating a carbon matrix in carbon-carbon can be an influencing factor for anisotropy only when the process of constructing or depositing the matrix has some directional dependence. For example, a matrix formed by chemical vapor deposition in a shell structural element can have a directional dependence of mechanical properties because of vapor penetration perpendicular to the shell surface and no penetration parallel to the surface. This effect is similar to effects obtained with pyrolytic graphite because of alignment of particles due to direction preferential deposition of material. In summary, the most obvious clue to the degree of anisotropy remains the fiber geometry, but anisotropy is also influenced by the matrix construction.

At least two difficulties arise in analysis of carbon-carbon materials. The first obvious difficulty is the analytical complication due to the many more mechanical properties necessary to characterize carbon-carbons as compared to simpler materials. This analytical complication is handled with relative ease in comparison to the more troublesome problem of measuring the additional mechanical properties. Basically, the problem is that simple strain states do not result from simple imposed stress states. For example, a uniaxial stress at 45° to the fiber directions in Fig. 4-7 leads to both extension in the direction of the load (and the usual Poisson contraction perpendicular to the load) and in-plane shearing if the ends of the specimen are not restrained in any way. On the other hand, if the specimen ends are restrained to remain perpendicular to the load, then a complicated nonuniform shearing and extensional response results. The complicated response occurs if the test specimen is short and wide whereas the simpler response occurs if the test specimen is long and narrow. In fact, if the specimen is relatively short and wide, the stiffness being measured is not the Young's modulus

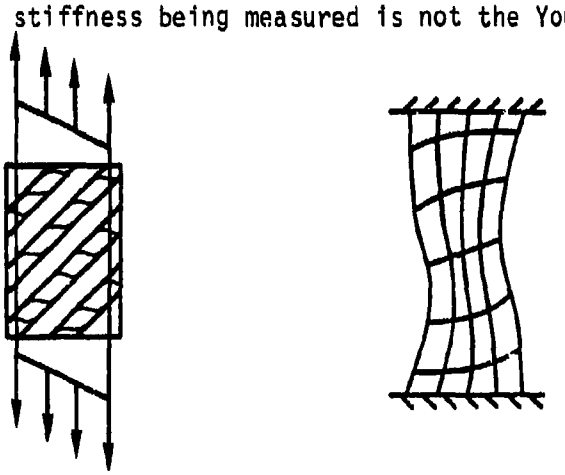

NO END EFFECT **RESTRAINED ENDS**

FIGURE 4-7 DEFORMATION OF A UNIDIRECTIONALLY REINFORCED LAMINA LOADED AT 45° TO THE FIBER DIRECTION

in the x-direction of the sketch in Fig. 4-8, but the two-dimensional (transformed reduced) stiffness $\bar{Q}_{11}$. The reason for this discrepancy is that the geometrically admissible state of strain in the specimen depends strongly on the geometry. If the specimen is long and slender, then the boundary conditions at the specimen end grips are of no consequence à la Saint Venant. Accordingly, a pure uniaxial strain is obtained and

$$\sigma_x = E_x \, \varepsilon_x \tag{4.1}$$

However, for a short, wide specimen, the end restraint of $\sigma_x \neq 0$, $\varepsilon_y = \gamma_{xy} = 0$ leads to the stress-strain relation

$$\sigma_x = \bar{Q}_{11} \, \varepsilon_x \tag{4.2}$$

Similar results are shown in Fig. 4-8 for an applied shear stress resulting in either G_{xy} as desired or $\bar{Q}_{66}$ if the test specimen geometry is not properly chosen.

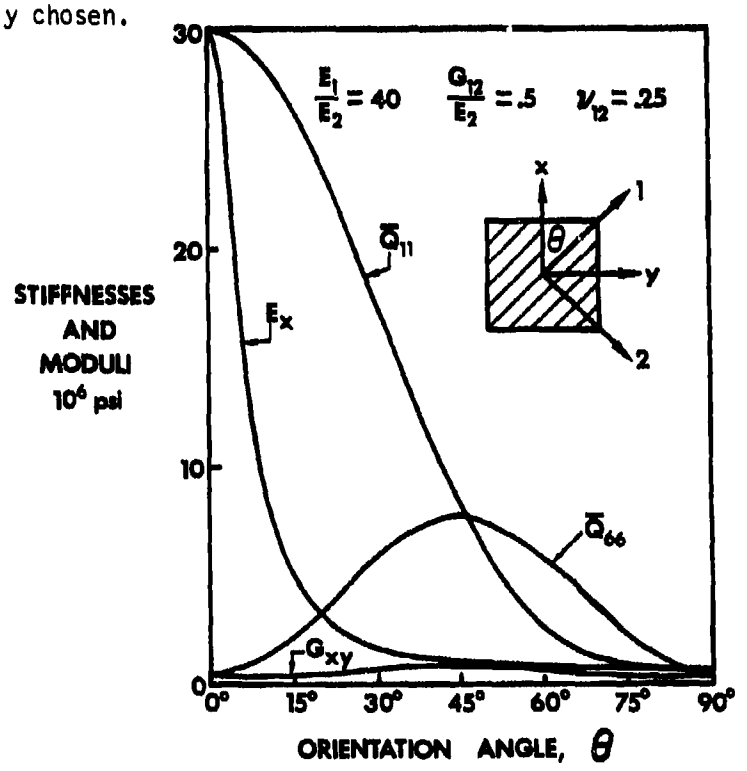

FIGURE 4-8 STIFFNESSES $\bar{Q}_{11}$ AND $\bar{Q}_{66}$ VERSUS MODULI E_x AND G_{xy}

The foregoing situation is but one example of many complicated mechanics problems which arise in the design of "proper" test specimens. By "proper" test specimens is meant specimens for which the desired response can be measured without undue influence of some unwanted response. For example, even with end restraint in Fig. 4-7, a specimen can be made long enough that the resulting deformation looks like the unrestrained end response. From a practical standpoint, if the response can be made predominantly simple by suitable choice of specimen geometry, then the goal of a proper test specimen is attained. Analysis of specimen response for various geometries to determine the geometry for which simple response occurs is the objective in many mechanics efforts. However, to date, little has been done to apply the principles of mechanics in rational treatment of carbon-carbon materials.

Some of the difficulties in rationally analyzing the mechanical behavior of carbon-carbon materials are related to even more complicated response characteristics than just discussed for a unidirectionally reinforced lamina. For example, anisotropic carbon-carbon under shear loading in one principal material plane will also have shear deformation in the two principal material planes which are perpendicular to the stressed principal material plane. This shear coupling obviously results in very complicated strain response. Moreover, the multimodulus characteristic of carbon-carbon materials is yet another complicating factor in addition to the nonlinear stress-strain behavior in every principal material direction.

If we ignore for a moment both the multimodulus character and the nonlinear character of carbon-carbon materials, the strain-stress equations for linear elastic behavior of orthotropic materials are (in ortho-

gonal x, y, z coordinates aligned with the principal material directions):

$$\begin{Bmatrix} \varepsilon_x \\ \varepsilon_y \\ \varepsilon_z \\ \gamma_{yz} \\ \gamma_{zx} \\ \gamma_{xy} \end{Bmatrix} = \begin{bmatrix} \frac{1}{E_x} & -\frac{\nu_{xy}}{E_x} & -\frac{\nu_{xz}}{E_x} & 0 & 0 & 0 \\ -\frac{\nu_{xy}}{E_x} & \frac{1}{E_y} & -\frac{\nu_{yz}}{E_y} & 0 & 0 & 0 \\ -\frac{\nu_{xz}}{E_x} & -\frac{\nu_{yz}}{E_y} & \frac{1}{E_z} & 0 & 0 & 0 \\ 0 & 0 & 0 & \frac{1}{G_{yz}} & 0 & 0 \\ 0 & 0 & 0 & 0 & \frac{1}{G_{zx}} & 0 \\ 0 & 0 & 0 & 0 & 0 & \frac{1}{G_{xy}} \end{bmatrix} \begin{Bmatrix} \sigma_x \\ \sigma_y \\ \sigma_z \\ \tau_{yz} \\ \tau_{zx} \\ \tau_{xy} \end{Bmatrix} \quad (4.3)$$

Obviously, nine independent constants

E_x, E_y, E_z = Young's moduli in x-, y-, and z-directions, respectively

ν_{ij} = Poisson's ratio for transverse strain in the j-direction when stress exists in the i-directions, i.e.,

$$\nu_{ij} = -\frac{\varepsilon_j}{\varepsilon_i}$$

for $\sigma_i = \sigma$ and all other stresses are zero.

G_{yz}, G_{zx}, G_{xy} = shear moduli in the y-z, z-x, and x-y planes, respectively.

must be measured.

We now recognize that the strain-stress relations in Eq. (4.3) must be modified to account for multimodulus behavior. Hence, in the manner

Jones [4-1], the shear moduli are replaced with Young's moduli at 45° to principal material directions. We then have the following nine independent mechanical properties:

$$E_x,\ E_y,\ E_z,\ \nu_{yz},\ \nu_{zx},\ \nu_{xy},\ E^{45}_{yz},\ E^{45}_{zx},\ E^{45}_{xy} \qquad (4.4)$$

when the carbon-carbon composite has three orthogonal principal material directions with unequal fiber volumes or unequal fiber sizes in the three directions. If the fiber volumes or fiber sizes are equal in two directions (as in AVCO 3D shown in Fig. 4-3), the six independent mechanical properties are:

$$E_x,\ E_y = E_x,\ E_z,\ \nu_{yz},\ \nu_{zx} = \nu_{zy},\ \nu_{xy},\ E^{45}_{yz},\ E^{45}_{zx} = E^{45}_{zy},\ E^{45}_{xy} \qquad (4.5)$$

Finally, if equal fiber volumes or fiber sizes exist in all three directions, the three independent mechanical properties are:

$$E_x = E_y = E_z \qquad \nu_{yz} = \nu_{zx} = \nu_{xy} \qquad E^{45}_{yz} = E^{45}_{zx} = E^{45}_{xy} \qquad (4.6)$$

(Note, however, that because of the three fiber directions the modulus at 45° is <u>independent</u> of the direct moduli and Poisson's ratios because the shear behavior is independent.) All of the properties in Eqs. (4.4), (4.5), and (4.6) must be measured both in tension and in compression. Moreover, these properties must be measured at many stress levels to account for the nonlinear stress-strain behavior in the manner of the Jones-Nelson-Morgan material models discussed in Section 2.

At this point, we have not yet examined the equations for off-axis behavior of such orthotropic materials nor have we considered any behavior of anisotropic carbon-carbon materials. We defer treatment of these complicated questions to subsequent reports on carbon-carbon material behavior.

Instead, we examine orthotropic and anisotropic carbon-carbon mechanical behavior which is representative of that found in References 4-2 through 4-11. Those references are the primary body of information on carbon-carbon mechanical properties although other information exists in the Journal of Composite Materials and in other classified and unclassified reports. Typical stress-strain curves are shown in Figs. 4-9 and 4-10 for the materials examined in the CCAP program (Carbon-Carbon Assessment Program). All of the stress-strain curves displayed have some degree of nonlinearity ranging from mild to strong. Notice how the shapes of the actual stress-strain curves are similar to the basic shape of the Jones-Nelson-Morgan nonlinear material model stress-strain curve in Fig. 2-21a on p. 67. The Jones-Nelson-Morgan model was developed to treat carbon-carbon behavior in addition to ATJ-S graphite as well as boron/epoxy, graphite/epoxy, and boron/aluminum. However, the model has not been applied to carbon-carbon.

The multimodulus characteristic of carbon-carbon is a manufacturer-dependent phenomenon. Early materials had drastic differences in tension and compression moduli. For example, the MDAC low modulus block course weave material [4-2] has a ratio of tension modulus to compression modulus in the z-direction ranging from 4 to 5! More recent materials have closer tension and compression moduli - for example, AVCO MOD 3 [4-5] has a tension modulus greater than the compression modulus by about 60% in both the x-direction and the z-direction.

Another behavioral characteristic worthy of note is the classical viscoplastic behavior of carbon-carbon at high temperatures. For example, AVCO MOD 3a exhibits this behavior at 5000°F in Fig. 4-11. The stress rate is increased by factors of ten and the stress-strain curve rises in

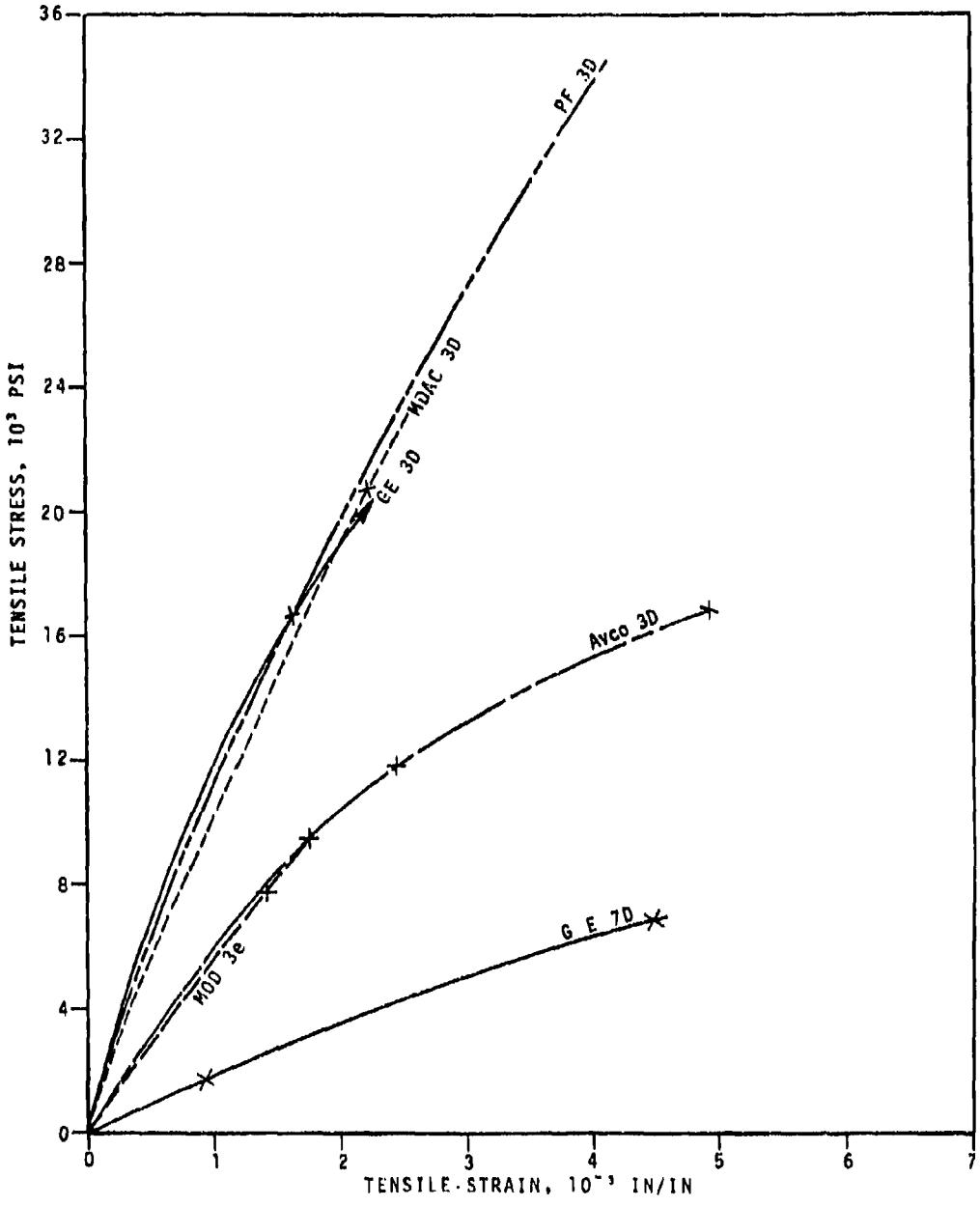

FIGURE 4-9 PROBABLE VALUE TENSION STRESS-STRAIN CURVES FOR CCAP MATERIALS AT 70°F IN THE Z-DIRECTION [4-6]

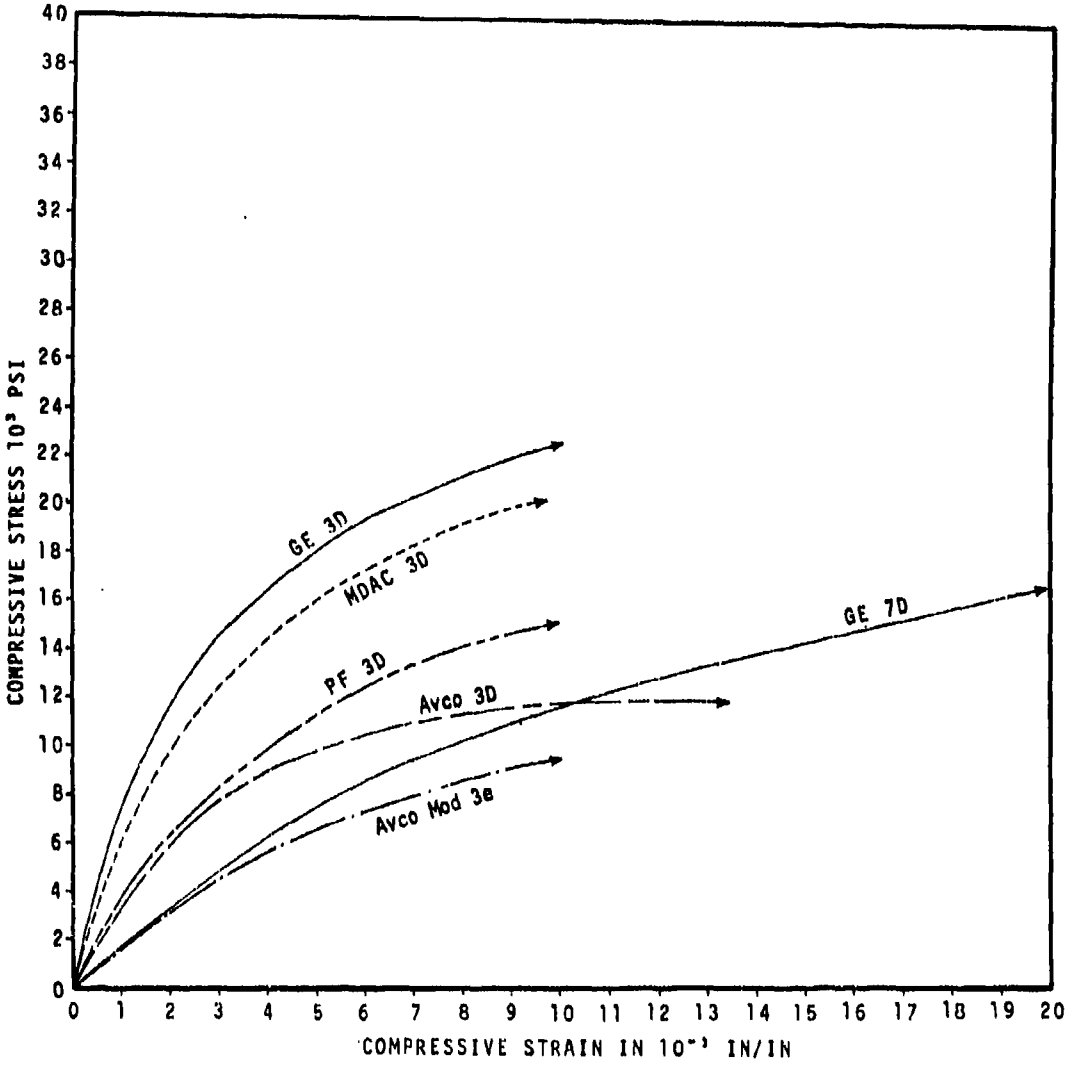

FIGURE 4-10 PROBABLE VALUE COMPRESSION STRESS-STRAIN CURVES FOR CCAP MATERIALS AT 5000°F IN THE Z-DIRECTION [4-6]

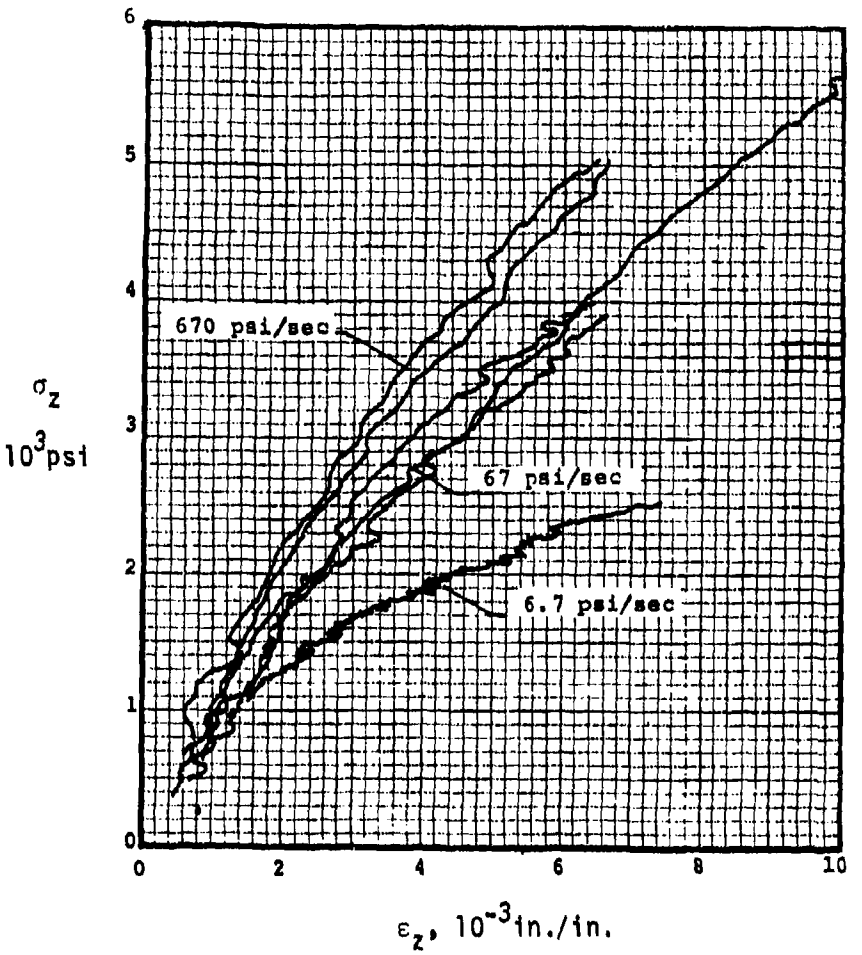

FIGURE 4-11 COMPRESSION STRESS-STRAIN CURVES FOR AVCO MOD 3a AT 5000°F IN THE Z-DIRECTION FOR VARIOUS STRESS RATES [4-5]

the usual viscoplastic manner.

Carbon-carbon has a characteristic of noncylindrical orthotropy which is quite different from the transverse isotropy of ATJ-S graphite. The practical significance of this difference is that in a reentry vehicle nosetip application, ATJ-S graphite is axisymmetric whereas carbon-carbon is not. This important distinction is significant from the point of view of the nosetip stress analyst, but will be ignored in this report.

In summary, carbon-carbon materials have mechanical behavioral characteristics which are a substantial escalation in degree of complication over the characteristics of graphite materials. The carbon-carbon analysis problem is very difficult and complex. Hence, the progress will be slow because of the many mechanics problems that must be addressed.

4.3 APPARENT FLEXURAL MODULUS AND FLEXURAL STRENGTH OF MULTIMODULUS MATERIALS

4.3.1 INTRODUCTION

The ASTM flexure test [4-12] is commonly used to measure the flexural modulus and flexural strength of materials other than the plastics for which it was originally developed. The officially designated equations for reporting the test results are applicable only to materials that are linear elastic to failure. However, the test is often used for carbon-carbon and other composite materials which have different (and sometimes nonlinear) stress-strain curves under tension loading than under compression loading.

In the ASTM flexure test for plastic materials [4-12], a rectangular cross section beam is subjected to either 3-point or 4-point transverse loading as shown in Fig. 4-12. The slope of the measured load-deflection curve is related to the apparent flexural modulus E_f which is defined

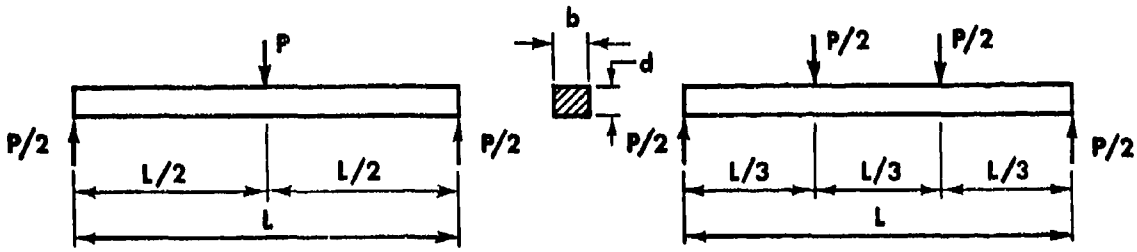

$$\sigma_{f_{max}} = \frac{3PL}{2bd^2} \qquad \sigma_{f_{max}} = \frac{PL}{bd^2}$$

FIGURE 4-12 ASTM FLEXURE TEST LOADING SETUP

with the usual moment-curvature relation:

$$M = E_f I v_o'' \tag{4.7}$$

If the tension modulus of the material is the same as the compression modulus, then the flexural modulus measurement is just a (redundant) way of measuring Young's modulus. The flexural failure stress is related to the failure load through the simple equations [4-12]:

$$\sigma_{f_{max}} = \begin{cases} \frac{3PL}{2bd^2}, & \text{3-point loading} \\ \\ \frac{PL}{bd^2}, & \text{4-point loading} \end{cases} \tag{4.8}$$

If the tension strength of the material is the same as the compression strength, then the flexural strength measurement is just a (redundant) way of measuring the strength. However, most materials have different strengths in tension than in compression even when the tension and compression moduli are the same. Accordingly, the apparent flexural strength is the lesser of the tension and compression strengths. If the moduli

are different in tension than in compression, then the flexural strength calculated with the ASTM equations, Eq. (4.8), is neither the compression strength nor the tension strength. Thus, the interpretation of the apparent flexural strength is difficult for many materials. The key limitation of the ASTM flexure test is its applicability only to linear elastic materials with the same modulus under tension loading as under compression loading.

The ASTM flexure test is, however, commonly used for materials such as fiber-reinforced composite materials which have a different modulus E_t under tension loading than the modulus E_c under compression loading. These multimodulus materials typically have the stress-strain behavior depicted in Fig. 4-13. There, the actual nonlinear stress-strain behavior is approximated with a bilinear stress-strain curve for which E_t is different from E_c. For this behavior, the axial strain in a beam under bending varies linearly through the depth of the beam as in Fig. 4-14.

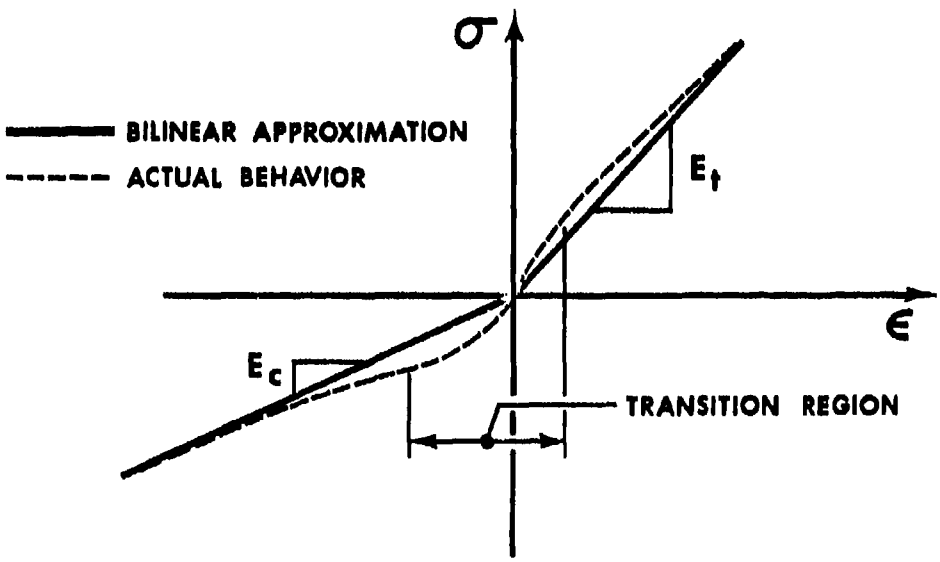

FIGURE 4-13 BILINEAR STRESS-STRAIN CURVE FOR MATERIALS WITH DIFFERENT MODULI IN TENSION AND COMPRESSION

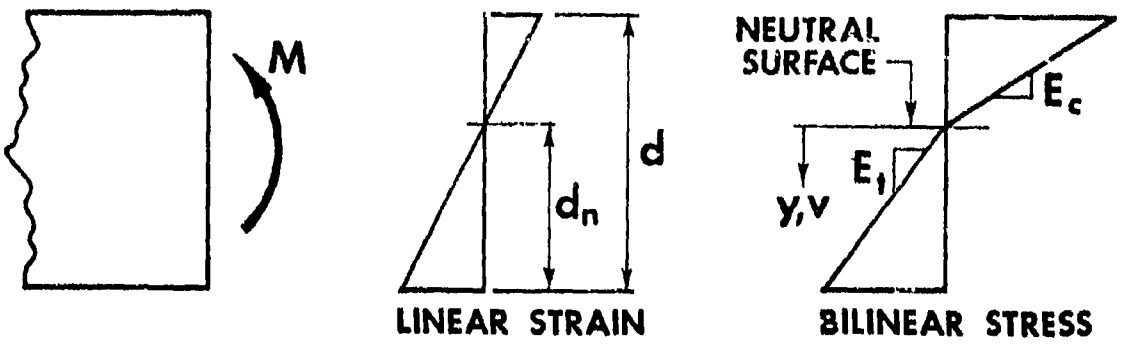

FIGURE 4-14 STRESS AND STRAIN VARIATION FOR A BEAM SUBJECTED TO MOMENT

Moreover, the stresses vary in a bilinear fashion through the depth of the beam. The significant factor is that the neutral axis, i.e., the point of zero stress and zero strain, is not at the mid-depth of the beam. Thus, because of the mixed state of tension and compression, the flexural modulus for multimodulus materials is neither E_t nor E_c, but must be interpreted differently. Also, the flexural strength is neither the tension strength or the compression strength.

The objective in this section is to assess the meaning of the ASTM flexure test when applied to multimodulus fiber-reinforced composite materials. The effect of different moduli in tension and compression on the apparent flexural modulus is predicted. The predicted flexural moduli are then compared with measured values for two carbon-carbon composite materials, Sandia CVD carbon felt and Avco 3D. Sandia CVD carbon felt [4-13] is a chemical vapor deposited (CVD) carbon matrix in carbon felt and is an orthotropic material because of the directional nature of vapor deposition. Avco 3D [4-14] has a phenolic matrix with high modulus graphite (Thornel 40 and/or Thornel 50) fibers as woven reinforcement in one plane and quartz filaments as reinforcement in an orthogonal plane.

Thus, Avco 3D is an orthotropic material. The effect of different moduli as well as different strengths in tension and compression on the apparent flexural strength is also predicted, and the results are compared with measured values for Sandia CVD carbon felt and Avco 3D.

The emphasis in this section is on proper analysis of the apparent flexural modulus and strength obtained for multimodulus materials with the ASTM flexure test. An important purpose in this section is to identify deficiencies in the current ASTM flexure test, to stimulate work to resolve these deficiencies, and to account for all pertinent behavioral aspects of multimodulus composite materials. The results of this analysis will enable a materials scientist to determine whether experimental data are consistent in the same manner that the usual reciprocal relation $\nu_{12}/E_1 = \nu_{21}/E_2$ is used to check experimental data for linear elastic orthotropic materials. The usefulness of this effort is also related to getting what we can out of present multimodulus material data and to generating appropriate data for multimodulus materials in the future.

4.3.2 APPARENT FLEXURAL MODULUS

Consider a beam of a multimodulus material subjected to pure moment as in Fig. 4-14. The axial strain is a linear function of y and depends on the curvature of the neutral surface, v_o'' (v'' evaluated at $y = 0$):

$$\varepsilon = v_o'' y \tag{4.9}$$

The uniaxial stress-strain relation is

$$\sigma = \begin{cases} E_t \varepsilon, & \sigma > 0 \\ E_c \varepsilon, & \sigma < 0 \end{cases} \tag{4.10}$$

We first locate the neutral axis since it is not, in general, at the beam mid-depth. The beam is subjected only to moment so the resultant axial force must be zero:

$$F = \int_A \sigma \, dA \tag{4.11}$$

Upon substitution of the stress-strain relation, Eq. (4.10), and the strain-displacement relation, Eq. (4.9), the force on a rectangular cross section beam is

$$\int_0^{d_n} E_t \, v_o'' \, y \, b \, dy - \int_0^{d-d_n} E_c \, v_o'' \, y \, b \, dy = 0 \tag{4.12}$$

where d_n is the distance from the bottom of the beam to the neutral axis as defined in Fig. 4-14. After integration,

$$\frac{v_o'' \, b}{2} \left[E_t d_n^2 - E_c (d-d_n)^2 \right] = 0 \tag{4.13}$$

or

$$E_t^{1/2} \, d_n = E_c^{1/2} \, (d-d_n) \tag{4.14}$$

whereupon the neutral axis is located at

$$d_n = \frac{E_c^{1/2}}{E_t^{1/2} + E_c^{1/2}} \, d \tag{4.15}$$

Next, the bending moment about the neutral axis is

$$M = \int_A \sigma \, y \, dA = \int_0^{d_n} E_t \, v_o'' \, y^2 \, b \, dy + \int_0^{d-d_n} E_c \, v_o'' \, y^2 \, b \, dy \tag{4.16}$$

which can be integrated to obtain

$$M = \frac{v_o'' b}{3}\left[E_t d_n^3 + E_c(d-d_n)^3\right] \tag{4.17}$$

Now substitute the location of the neutral axis, Eq. (4.15), to get

$$M = \frac{v_o'' bd^3}{3}\left[E_t\left(\frac{E_c^{1/2}}{E_t^{1/2} + E_c^{1/2}}\right)^3 + E_c\left(\frac{E_t^{1/2}}{E_t^{1/2} + E_c^{1/2}}\right)^3\right] \tag{4.18}$$

which can be simplified to

$$M = \frac{v_o'' bd^3}{3}\left[\frac{E_t E_c}{(E_t^{1/2} + E_c^{1/2})^2}\right] \tag{4.19}$$

Compare this moment expression with Eq. (4.7) and realize that $I = bd^3/12$ for a rectangular cross section to obtain

$$E_f = \frac{4E_t E_c}{(E_t^{1/2} + E_c^{1/2})^2} \tag{4.20}$$

This apparent flexural modulus can be normalized with respect to the compression modulus in the form

$$\frac{E_f}{E_c} = \frac{4(E_t/E_c)}{1 + 2(E_t/E_c)^{1/2} + E_t/E_c} \tag{4.21}$$

and plotted along with the normalized average modulus

$$\frac{E_{avg}}{E_c} = \frac{(E_t + E_c)/2}{E_c} = (E_t/E_c + 1)/2 \tag{4.22}$$

and the normalized tension and compression moduli versus the multimodulus ratio E_t/E_c in Fig. 4-15. There, we see that

(1) E_f is always less than E_{avg} and

(2) E_f is always closer to the smaller of E_t and E_c.

These observations can be used to test the quality of experimental flexural modulus data. That is, if the experimental data do not exhibit those characteristics, then we would have to be suspicious of their validity. This test is analogous to applying the reciprocal relation $\nu_{12}/E_1 = \nu_{21}/E_2$ to test experimental modulus and Poisson's ratios data for orthotropic materials.

Experimental results for materials with substantially different moduli in tension and compression are plotted in Fig. 4-16 which is an expansion of Fig. 4-15 near the region where $E_t/E_c = 1$. For Sandia CVD carbon felt [4-13], an orthotropic material, the tension modulus is as much as 42% higher than the compression modulus depending on the vapor deposition pressure in Table 4-1. For Avco 3D [4-14], the tension moduli are up to 25% lower than the compression moduli as shown in Table 4-2. Although Avco 3D is an orthotropic material, the orthotropy is excited only in the form of G_{xy} since the material in the beam is oriented such that $E_x = E_y$ (i.e., the x- and y-coordinates of the beam coincide with the principal material directions in the plane of the graphite fibers). The flexural moduli are calculated from Eq.(4.20) with the known tension and compression moduli and are also shown in Tables 4-1 and 4-2. There, the calculated moduli are 5% and 7% too high and 3% too low for Sandia CVD carbon felt and 2% and 5% too high for Avco 3D. This agreement between theory and experiment is rather good considering the inherent accuracy of the experiments and the bilinear stress-strain curve approximation. Thus,

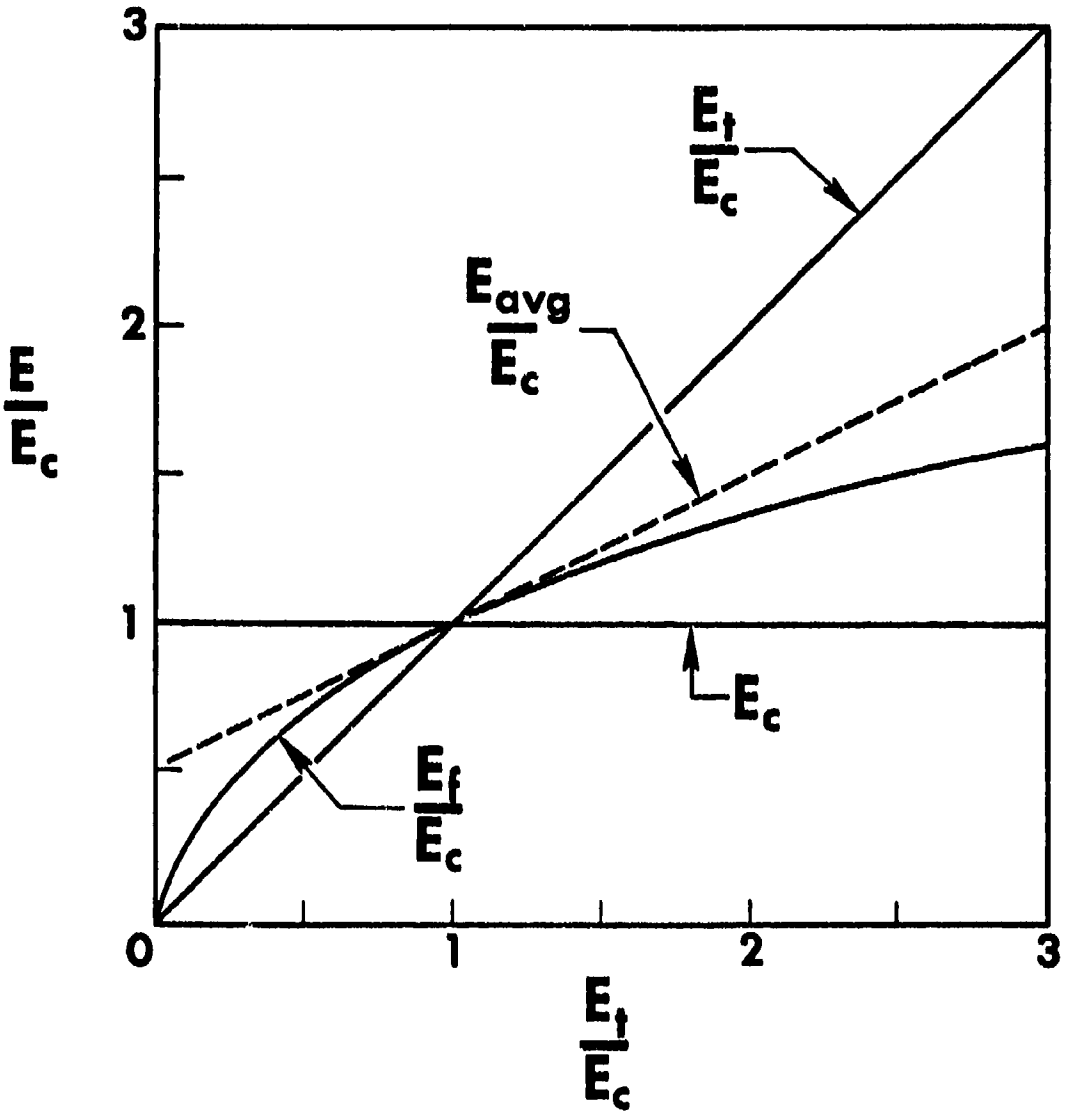

FIGURE 4-15 NORMALIZED FLEXURE, AVERAGE, AND TENSION MODULI VERSUS E_t/E_c

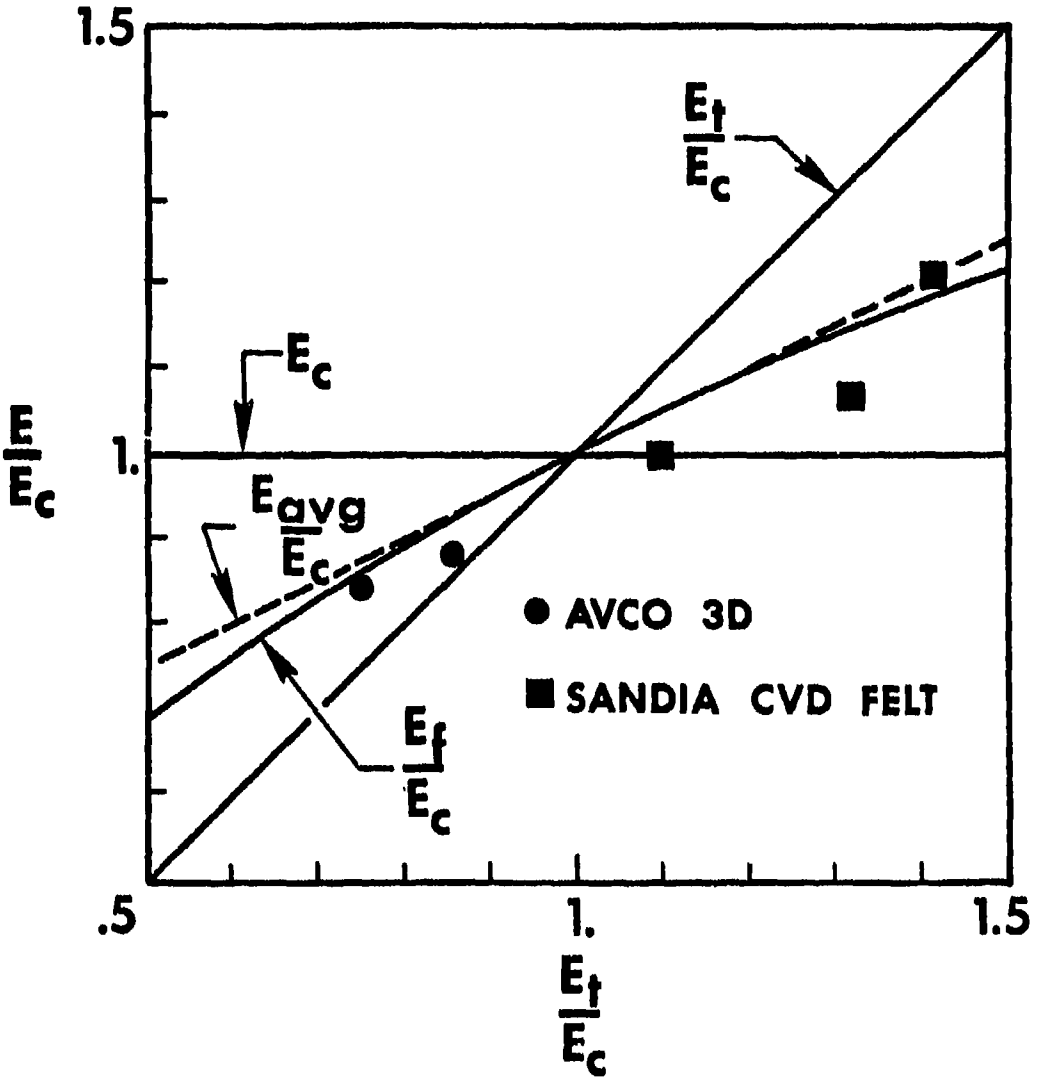

FIGURE 4-16 NORMALIZED FLEXURAL MODULUS

- EXPERIMENTAL AND THEORETICAL RESULTS

TABLE 4-1

STIFFNESSES OF SANDIA CVD CARBON FELT

DEPOSITION PRESSURE mm Hg	E_t 10^6psi (GN/m^2)	E_c 10^6psi (GN/m^2)	$\frac{E_t}{E_c}$	E_f		
				MEASURED 10^6psi (GN/m^2)	CALCULATED 10^6psi (GN/m^2)	ERROR
35	2.2 (15.2)	2.0 (13.8)	1.10	2.0 (13.8)	2.1 (14.5)	+5.0%
100	3.7 (25.5)	2.8 (19.3)	1.32	3.0 (20.7)	3.2 (22.1)	+6.7%
760	4.7 (32.4)	3.3 (22.8)	1.42	4.0 (27.6)	3.9 (26.7)	-2.5%

TABLE 4-2

STIFFNESSES OF AVCO 3D THORNEL/PHENOLIC

THORNEL VOLUME FRACTION	E_t 10^6psi (GN/m^2)	E_c 10^6psi (GN/m^2)	$\frac{E_t}{E_c}$	E_f		
				MEASURED 10^6psi (GN/m^2)	CALCULATED 10^6psi (GN/m^2)	ERROR
50	4.54 (31.3)	5.31 (36.6)	.855	4.68 (32.3)	4.90 (33.8)	+4.7%
66	4.70 (32.4)	6.26 (43.2)	.750	5.28 (36.4)	5.40 (37.2)	+2.3%

we can claim the ability to calculate the flexural modulus for these materials without having to resort to the expense and time of an ASTM flexure test (not to mention the high cost of the material for the test specimens!).

4.3.3 APPARENT FLEXURAL STRENGTH

Irrespective of whether 3-point or 4-point loading is used, the ASTM maximum stress versus moment relation is

$$\sigma_{ASTM_{max}} = \frac{Mc}{I} = \frac{Md/2}{bd^3/12} = \frac{6M}{bd^2} \tag{4.23}$$

in which the neutral axis is presumed to be at the mid-depth of the beam. If the maximum moment versus load relation for each type of loading is considered, then the ASTM maximum stress versus load relations are

$$\sigma_{ASTM_{max}} = \begin{cases} \frac{6}{bd^2}\ \frac{P}{2} \cdot \frac{L}{2} = \frac{3PL}{2bd^2}, & \text{3-point loading} \\ \frac{6}{bd^2}\ \frac{P}{2} \cdot \frac{L}{3} = \frac{PL}{bd^2}, & \text{4-point loading} \end{cases} \tag{4.24}$$

For multimodulus materials, we will derive the correct maximum stress versus moment relation in which the difference between the neutral axis and the beam mid-depth is accounted for.

The maximum stresses in the beam cross section are

$$\begin{aligned} \sigma_{t_{max}} &= E_t\, \varepsilon_{t_{max}} = E_t\, v_o''\, y_{t_{max}} = E_t\, v_o''\, d_n \\ \sigma_{c_{max}} &= E_c\, \varepsilon_{c_{max}} = E_c\, v_o''\, y_{c_{max}} = E_c\, v_o''\, (d-d_n) \end{aligned} \tag{4.25}$$

irrespective of whether $E_t \quad E_c$ or $E_t \quad E_c$. We solve for v_o'' from Eq. (4.19) and substitute for d_n from Eq. (4.15) to get

$$\sigma_{t_{max}} = E_t \frac{3M}{bd^3} \left\{ \left[\frac{E_t E_c}{(E_t^{1/2} + E_c^{1/2})^2} \right] \right\} \left[\frac{E_t^{1/2}}{E_t^{1/2} + E_c^{1/2}} d \right]$$

$$\sigma_{c_{max}} = E_c \frac{3M}{bd^3} \left\{ \left[\frac{E_t E_c}{(E_t^{1/2} + E_c^{1/2})^2} \right] \right\} \left[\frac{E_t^{1/2}}{E_t^{1/2} + E_c^{1/2}} d \right] \tag{4.26}$$

which can be simplified to

$$\sigma_{t_{max}} = \left\{ \left[(E_t/E_c)^{1/2} + 1 \right] \Big/ 2 \right\} \frac{6M}{bd^2}$$

$$\sigma_{c_{max}} = \left\{ \left[1 + (E_c/E_t)^{1/2} \right] \Big/ 2 \right\} \frac{6M}{bd^2} \tag{4.27}$$

where the terms in braces are the corrections due to noncoincidence of the neutral axis and the beam mid-depth. Obviously, when $E_t = E_c$, the stresses in Eq. (4.27) are equal to each other and to the ASTM maximum stress in Eq. (4.23).

The actual maximum tensile and compressive stresses for multimodulus materials in the ASTM flexure test can be summarized in the form

$$\sigma_{t_{max}} = C_t \, \sigma_{max_{ASTM}}$$

$$\sigma_{c_{max}} = C_c \, \sigma_{max_{ASTM}} \tag{4.28}$$

where the correction factors C_t and C_c are multipliers on the calculated ASTM stresses used to obtain the actual maximum stresses. These correction factors are plotted in Fig. 4-17 as a function of the multimodulus

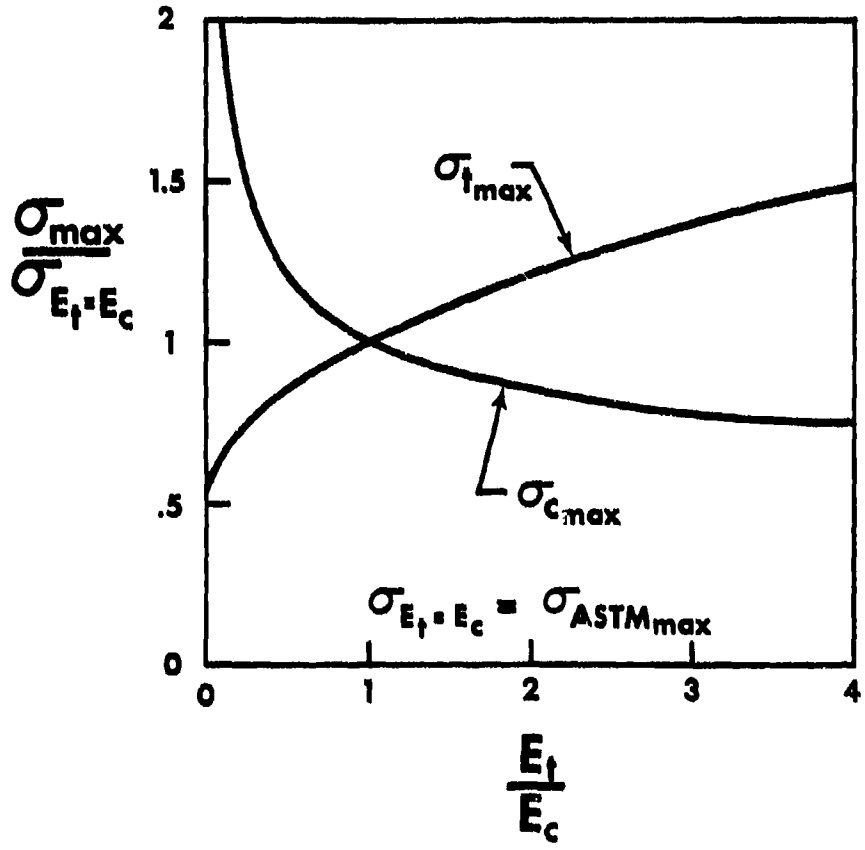

FIGURE 4-17 ACTUAL MAXIMUM TENSILE AND COMPRESSIVE STRESSES VERSUS MULTIMODULUS RATIO

ratio E_t/E_c. We see from Eq. (4.27) and Fig. 4-17 that the largest maximum stress occurs on the side of the beam where the largest modulus is excited. If $E_t > E_c$, then $C_t > 1$ and $C_c < 1$. That is, for materials which are stiffer in tension than in compression, the actual maximum tensile stress exceeds the ASTM stress whereas the actual maximum compressive stress is less than the ASTM stress as in Fig. 4-18. Moreover, if $E_t < E_c$, then $C_t < 1$ and $C_c > 1$. That is, for materials which are more flexible in tension than in compression, the actual maximum tensile stress is less than the ASTM stress whereas the actual maximum compressive stress exceeds the ASTM value as in Fig. 4-18.

Quantitatively, if $E_t/E_c = .5$, the actual maximum compressive stress is 21% higher than the value prescribed in the ASTM calculation. Also, the actual maximum tensile stress is 15% lower than the ASTM value. On the other hand, if $E_t/E_c = 2$, the actual maximum tensile stress is 21% higher than the ASTM value and the actual maximum compressive stress is

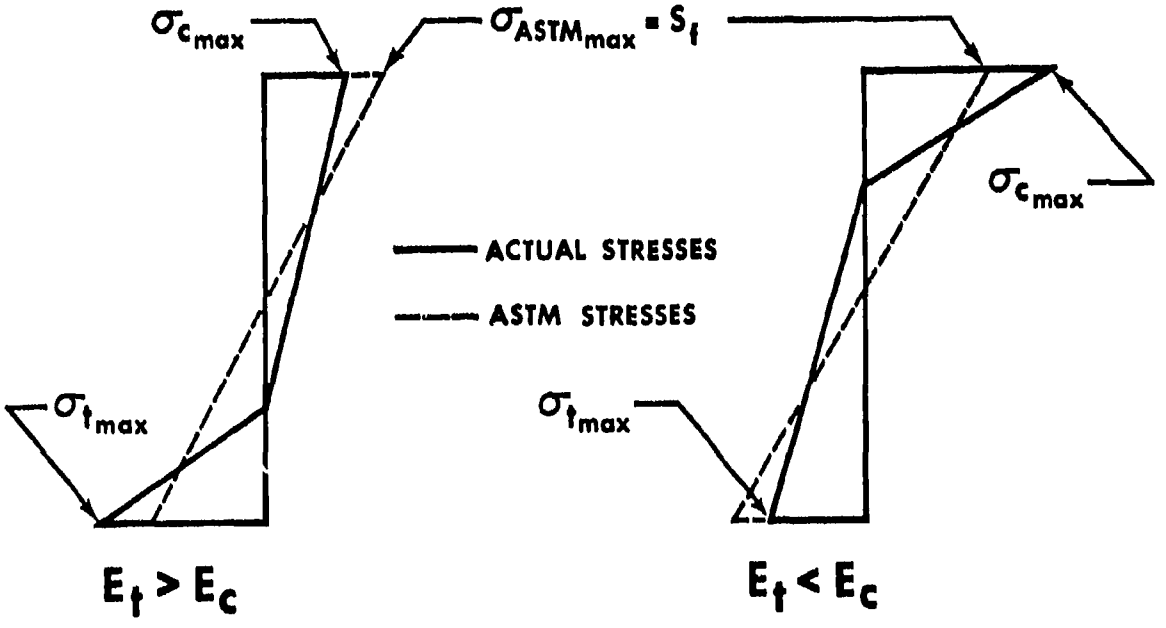

FIGURE 4-18 ACTUAL VERSUS ASTM STRESS DISTRIBUTIONS

15% lower than the ASTM value.

Note that simultaneous failure in tension and compression is not implied in these calculations. That is, neither $\sigma_{t_{max}}$ nor $\sigma_{c_{max}}$ is necessarily the respective strength S_t or S_c. Thus, if we are given the load or moment at which a beam fails, we calculate the maximum tensile and compressive stresses from Eq. (4.27) and compare them with the respective strengths. However, the analysis is restricted to materials which can be approximated with the bilinear stress-strain curve in Fig. 4-13 and which are linear elastic to failure. This latter restriction is probably the toughest to satisfy for most materials.

Four subcases of behavior occur based on whether E_t is larger or smaller than E_c and whether S_t is larger or smaller than S_c:

(1) $E_t > E_c$, $S_t > S_c$

(2) $E_t > E_c$, $S_t < S_c$

(3) $E_t < E_c$, $S_t > S_c$

(4) $E_t < E_c$, $S_t < S_c$

In both cases (1) and (2), $\sigma_{t_{max}}$ is underpredicted and $\sigma_{c_{max}}$ is overpredicted with the ASTM equations, Eq. (4.8), as seen in Fig. 4-18. On the other hand, in cases (3) and (4), $\sigma_{t_{max}}$ is overpredicted and $\sigma_{c_{max}}$ is underpredicted. In case (2), the beam fails in tension because $\sigma_{t_{max}} > \sigma_{c_{max}}$ and $S_t < S_c$. Thus, the apparent flexural strength is

$$S_f = \frac{S_t}{C_t} \tag{4.29}$$

which is always less than the tension strength because $C_t > 1$. In case (3), the beam fails in compression because $\sigma_{c_{max}} > \sigma_{t_{max}}$ and $S_c < S_t$. Thus, the apparent flexural strength is

$$S_f = \frac{S_c}{C_c} \tag{4.30}$$

which is always less than the compression strength because $C_c > 1$. No definite failure mode exists for the inequalities in cases (1) and (4); instead, the apparent flexural strength is

$$S_f = \text{lowest of } \frac{S_t}{C_t} \text{ and } \frac{S_c}{C_c} \tag{4.31}$$

which is always between the tension and compression strengths. Obviously, the apparent flexural strength never coincides with either S_t or S_c for multimodulus materials. In fact, S_f is sometimes lower than S_t [case (2)], sometimes lower than S_c [case (3)], and sometimes between S_t and S_c [cases (1) and (4)].

Sandia CVD Carbon Felt has $E_t > E_c$ and $S_c > S_t$ as seen in Table 4-3 so is a case (2) material which always fails in tension. The apparent flexural strengths are calculated from Eq. (4.29) and listed in Table 4-3. Note that the calculated flexural strengths are below the values of S_t (as we calculated them to be), but the measured flexural strengths are above the S_t values.

Avco 3D has $E_c > E_t$ and $S_c < S_t$ as seen in Table 4-4 so is a case (3) material which always fails in compression. The apparent flexural strengths are calculated from Eq. (4.30) and listed in Table 4-4. However, the calculated S_f values are lower than S_c, but the measured values of S_f are even higher than the S_t values (which in turn are higher than the S_c values).

The measured behavior is significantly different from the predicted behavior for both example materials. Thus, we must question either the

TABLE 4-3

STRENGTHS OF SANDIA CVD CARBON FELT

DEPOSITION PRESSURE mm Hg	S_t 10^3psi (MN/m^2)	S_c 10^3psi (MN/m^2)	$\frac{E_t}{E_c}$	S_f		
				MEASURED 10^3psi (MN/m^2)	CALCULATED 10^3psi (MN/m^2)	ERROR
35	4.78 (33.0)	23.5 (162)	1.10	6.18 (42.6)	4.67 (32.2)	-24%
100	6.55 (45.2)	35.5 (245)	1.32	9.07 (62.5)	6.10 (42.0)	-33%
760	6.26 (43.2)	51.8 (357)	1.42	9.26 (63.9)	5.89 (40.6)	-36%

TABLE 4-4

STRENGTHS OF AVCO 3D THORNEL/PHENOLIC

THORNEL VOLUME FRACTION	S_t 10^3psi (MN/m^2)	S_c 10^3psi (MN/m^2)	$\frac{E_t}{E_c}$	S_f		
				MEASURED 10^3psi (MN/m^2)	CALCULATED 10^3psi (MN/m^2)	ERROR
50	19.3 (133)	13.3 (91.7)	.855	22.1 (152)	12.8 (88.3)	-42%
66	23.6 (163)	17.6 (121)	.750	30.9 (213)	16.3 (112)	-47%

theory, its applicability to the data, or the data themselves. Presuming the data are correct, we examine the theory to see if any deficiencies exist. The most obvious deficiency of this theory as applied to orthotropic materials is the neglect of shear behavior. However, Sandia CVD carbon felt has only mild orthotropy and has the same kind of disagreement between theory and experiment as Avco 3D so a shear-related deficiency is not likely.

Perhaps another possible reason for the disagreement is that the stress-strain behavior of both example materials is not linear elastic to failure. Thus, since the theory is not applicable to nonlinear stress-strain behavior, it is not applicable to the strength analysis of these materials. However, the ASTM prescribed maximum stress calculations are not applicable to these kinds of materials either. Thus, the meaning of the reported flexural strength data is not clear. What is clear is that the ASTM flexure test and calculations, as presently prescribed, are not applicable to multimodulus materials or to materials with nonlinear stress-strain behavior. However, these expensive tests continue to be run and reported without sufficient information for proper interpretation and utilization.

4.3.4 SUMMARY

Flexural modulus and flexural strength data for multimodulus materials cannot be used to extract what happens individually in tension and in compression. Instead, flexure behavior is simply some kind of averaging of those two behaviors with shear effects thrown in for confusion. Neglecting shear is ignoring an important behavioral aspect of most composite materials. However, the inclusion of shear effects in the flexure test analysis may not be warranted because flexure data are not basic

data (i.e., not independent of other parameters) and therefore need not be refined. Accordingly, the ASTM flexure test is very misleading when applied to materials with distinctly different stiffnesses and strengths in tension than in compression. Moreover, the typically nonlinear stress-strain behavior of fiber-reinforced composite materials, especially carbon-carbon, is another invalidating factor for the ASTM flexure test. Designers who seem to want these flexure data are actually avoiding or masking the real problems of nonlinear stress-strain behavior as well as sometimes low and sometimes high shear modulus and shear strength of many composite materials. (In fact, the span-to-depth ratio for the flexure test specimen is probably so different from the actual designer's application that shear plays entirely different roles in the specimen and the design application.) The proper course of action is to develop and use more rational analyses of nonlinear behavior and shear effects coupled with better shear modulus and shear strength data that are reported only in conjunction with the pertinent stress-strain curves to failure.

4.4 FUTURE MODELING WORK

The Jones-Nelson-Morgan nonlinear material model must be fit to representative carbon-carbon materials. Subsequently, the model must be exercised in various theoretical-experimental correlation efforts to validate the model.

The first step for each material is to fit the model to the mechanical behavior in the principal material directions and at 45° to the principal material directions for an orthotropic material (more complicated mechanical behavior must be treated for anisotropic materials). The only

practical way to perform these material model fits is to use the JNMDATA computer program (discussed in Section 2.4) to ease the burden of plotting the actual and approximate stress-strain and mechanical property versus energy curves. However, before the JNMDATA program can be utilized, it must be extended to orthotropic materials and possibly to anisotropic materials. These extensions are relatively straightforward. With the extensions, the JNMDATA program will be an essential element in the procedure for modeling carbon-carbon properties.

The next logical step in applying the material model is a series of validations of the model by comparison of predicted and measured strains for a representative set of loading conditions ranging from simple to complex and including both mechanical and thermal loads. The simplest such situation is uniaxial mechanical loading at some angle to the principal material directions (other than the 45° angle at which E^{45} is measured. The next simplest loading condition is a biaxial stress state such as occurs in the MDAC tubular test specimen for graphite [4-15].

Various carbon-carbon materials have been examined in the Southern Research Institute thermal stress disk test which is described for graphitic materials in Section 3.2. However, the response of a carbon-carbon disk is not axisymmetric because of the orthotropic character of carbon-carbon, i.e., the disk does not have cylindrical orthotropy much less the in-plane isotropy of a graphite disk. Accordingly, the analysis of a carbon-carbon disk is a substantial escalation in difficulty over that of a graphite disk. For example, the Jones-Nelson-Morgan nonlinear material model could be incorporated in the ASAAS finite element program [4-16] with modification for noncylindrical orthotropy or some three-dimensional finite element computer program. Obviously, such analyses would involve

considerable escalation in cost for computer time over the cost for graphitic material analyses.

Jortner obtained preliminary measurements of strains in carbon-carbon disks under a biaxial stress field due to high speed rotation [4-17]. Experimental results such as these could be used in yet another correlation of theoretical and experimental results.

The next logical step in a hierarchy of correlations between theory and experiment is to consider the thermal and mechanical loading for an actual reentry vehicle nosetip. The level of analysis needed is identical to that for the thermal stress disk test because of the noncylindrical orthotropy of carbon-carbon. Accordingly, the nosetip analyses would be quite expensive relative to those for graphitic materials.

Obviously, the foregoing series of correlations between theory and experiment is much more complicated than the series just completed for ATJ-S graphite (completed with the exception of the nosetip strain correlation). Moreover, because of the relatively high expense and variability of the mechanical properties of carbon-carbon, the basic mechanical properties will not be available with the statistical confidence of graphitic materials. Thus, there is no room in the continuing development of carbon-carbon for time, scarce material, and money for tests such as the flexural modulus and strength test which are not justified or useful. We must strive to obtain the most and highest quality information from each and every measurement.

5. CONCLUDING REMARKS

The major graphitic material analysis problem areas of biaxial softening and multimodulus nonlinear behavior have been successfully treated with the various Jones-Nelson-Morgan nonlinear material models. The models have been validated by comparison of predicted response with measured response for a series of meaningful physical problems. These problems include uniaxial off-axis and biaxial mechanical loading as well as biaxial thermal loading of an annular disk and multiaxial thermal and mechanical loading of a reentry vehicle nosetip. The capability to accurately predict stresses and strains in ATJ-S graphite under complex mechanical and thermal loading has been achieved.

On the other hand, the application of the Jones-Nelson-Morgan nonlinear material model to carbon-carbon materials is just beginning. The model is apparently well-suited for treatment of the stress-strain response typical of carbon-carbon materials. However, this supposition must be verified in a meaningful series of correlations between Jones-Nelson-Morgan material model predictions and carefully measured response for various mechanical and thermal loading problems.

APPENDIX

DETERMINATION OF THE POINT OF ZERO SLOPE ON AN IMPLIED STRESS-STRAIN CURVE BY INTERVAL HALVING

The point of zero slope on an implied stress-strain curve or the point at which the slope of the stress-strain curve has some prescribed nonzero value must be determined before the linear extrapolations of the stress-strain data described in Section 2.3.3 can be implemented. The expression for the slope of an implied stress-strain curve in Eq. (2.20) is a function of the stress and the strain. However, for a given strain the corresponding implied stress is easily determined from the implied stress-strain relation in Eq. (2.19) so the slope is a function of the strain only. The strain ε^* at which the slope of the implied stress-strain curve is zero or a prescribed nonzero value is the root of a complicated nonlinear equation obtained by combining Eqs. (2.19) and (2.20). This root is easily found by the numerical technique of interval halving. Interval halving, in general, involves halving an interval in which the root of a nonlinear expression lies until the root is enclosed by a very small interval. This technique is described in this appendix for finding the point of zero slope, but the general procedure is the same for finding a point of prescribed nonzero slope.

Before the interval halving technique can be applied, an interval in which the strain ε^* lies must be determined. This interval is found by choosing an initial strain at which the slope of the implied stress-strain curve is positive and then increasing this strain by prescribed increments until a strain level is reached at which the slope of the implied stress-strain curve is negative. For example, at the last stress-strain data point in Fig. A-1, the slope of the implied stress-strain

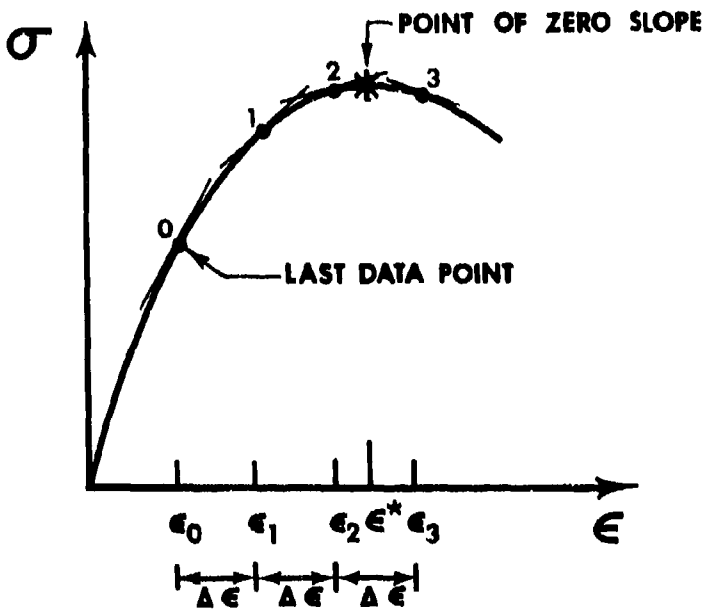

FIGURE A-1 STRAIN INCREMENTS FOR FINDING POINT OF ZERO SLOPE ON A IMPLIED STRESS-STRAIN CURVE

curve is positive. The point of zero slope is located to the right of this point. Thus, the strain ε_0 corresponding to the last data point in Fig. A-1 is used as the initial left bound of the interval in which ε^* lies. Then, the strain ε_0 is increased by a prescribed increment $\Delta\varepsilon$, and the slope is evaluated at this new strain ε_1. The slope of the implied stress-strain curve in Fig. A-1 is positive at ε_1, so ε_0 is replaced as the left bound of the interval by the new strain ε_1. Next, ε_1 is increased by $\Delta\varepsilon$, and the slope is evaluated at ε_2. Again, the slope is positive so ε_1 is replaced as the left bound of the interval by ε_2. The incrementing process is continued until finally, at the strain ε_3, the slope of the implied stress-strain curve is negative. Thus, the strain ε^* is located in the interval $\varepsilon_2 < \varepsilon < \varepsilon_3$. The size of the prescribed increment $\Delta\varepsilon$ used in finding the interval surrounding ε^*

is arbitrary but should be chosen wisely. The increment should not be so small that the strain has to be increased a large number of times before a point of negative slope is found. At the same time, the increment $\Delta\varepsilon$ should not be so large that the interval enclosing the point of zero slope is exceedingly wide. However, due to the rapid convergence of the method after interval halving is initiated, reasonably large increments are preferable over very small increments.

The interval $\varepsilon_2 < \varepsilon < \varepsilon_3$ surrounding ε^* in Fig. A-1 is large and must be decreased until the difference between the left and right bounds of the interval is very small; i.e., until ε^* is known to a specified level of accuracy. The interval around the point of zero slope is decreased in an orderly manner by use of interval halving. The interval halving technique is easily described with the aid of the slope-strain curve in Fig. A-2. The initial interval surrounding ε^*, the strain at zero slope, is bounded in Fig. A-2 by ε_p and ε_n, the strains at which

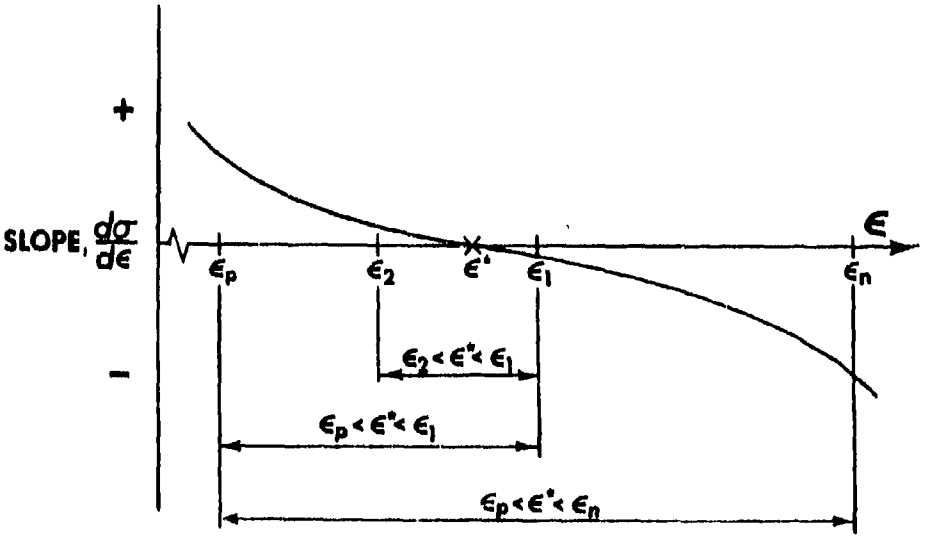

FIGURE A-2 INTERVAL HALVING OF A SLOPE-STRAIN CURVE TO FIND POINT OF ZERO SLOPE

the slope is positive and negative, respectively. The strains ε_p and ε_n in Fig. A-2 correspond to the strains ε_2 and ε_3, respectively, in Fig. A-1. The search for ε^* is initiated by evaluating the slope at the midpoint of the interval bounded by ε_p and ε_n. This initial strain is labeled ε_1 in Fig. A-2. If the slope is negative at ε_1 as in Fig. A-2 ε^* lies between ε_p and ε_1. If the slope is positive at ε_1, ε^* lies between ε_1 and ε_n. Thus, ε_1 lies in an interval half as large as the original interval. The slope is then evaluated at the midpoint of this new interval, i.e., at ε_2 in Fig. A-2. The slope at ε_2 is positive so ε^* lies between ε_1 and ε_2. Thus, the interval enclosing ε^* is halved again. This interval halving process is continued until the interval around ε^* becomes sufficiently small; i.e., until ε^* is known to a desired level of accuracy.

In conclusion, the point of zero slope on an implied stress-strain curve is quickly and easily determined by the numerical technique of interval halving. The process consists of two steps. First, an interval of strain in which the strain corresponding to zero slope is located must be determined. Then, this interval is halved until it becomes very small about the strain corresponding to zero slope. A point of nonzero slope on the implied stress-strain curve can be found by a procedure analogous to the one for finding the point of zero slope. The only difference between the two procedures is that for finding a point of nonzero prescribed slope, the strain at which the slope-strain curve crosses the line $\frac{d\sigma}{d\varepsilon} = \left(\frac{d\sigma}{d\varepsilon}\right)^* \neq 0$ is desired instead of the strain at which the slope-strain curve crosses the slope axis $\frac{d\sigma}{d\varepsilon} = 0$.

REFERENCES

1-1. Robert M. Jones, "Reentry Vehicle Nosetip Stress Analysis," in Proceedings of the Nosetip Stress Analysis Technical Interchange Meeting, (San Bernardino, California, 20 September 1967), Robert M. Jones, Editor, TR-0158(S3816-22)-2, The Aerospace Corporation, San Bernardino, California, November 1967.

1-2. Robert M. Jones and John R. Koenig, "Reentry Vehicle Nosetip Stress Analysis," presented at the Conference on Brittle Fracture of Graphites and Carbon-Carbon Composites, Asilomar, Pacific Grove, California, 27 February-1 March 1973. Also AFML-TR-75-76, August 1975.

1-3. J. Jortner, Biaxial Mechanical Properties of ATJ-S Graphite, Final Report under AF Contract F04701-068-C-0288, Change Order 15, McDonnell-Douglas Report No. MDC G 2072, December 1970.

1-4. J. Jortner, Multiaxial Behavior of ATJ-S Graphite, Interim Report, McDonnell-Douglas Astronautics Company, Air Force Materials Laboratory Report AFML-TR-71-160, July 1971.

1-5. J. Jortner, Multiaxial Behavior of ATJ-S Graphite, McDonnell-Douglas Astronautics Company, Air Force Materials Laboratory Report AFML-TR-71-253, December 1971.

1-6. J. Jortner, Multiaxial Response of ATJ-S Graphite, McDonnell-Douglas Astronautics Company, Air Force Materials Laboratory Report AFML-TR-73-170, October 1973.

1-7. Robert M. Jones and Dudley A. R. Nelson, Jr., "A New Material Model for the Nonlinear Biaxial Behavior of ATJ-S Graphite," Journal of Composite Materials, January 1975, pp. 10-27.

1-8. J. William Davis and N. R. Zurkowski, Put the Strength and Stiffness Where You Need It, Report T-STDB(101.05)R, Reinforced Plastics Division, Minnesota Mining and Manufacturing Company.

1-9. Structural Design Guide for Advanced Composites Applications, Vol. 1, Material Characterization, 2nd Edition, Air Force Materials Laboratory, January 1971.

1-10. K. M. Kratsch, J. C. Schutzler, and D. A. Eitman, "Carbon-Carbon 3-D Orthogonal Material Behavior," AIAA Paper No. 72-365, AIAA/ASME/SAE 13th Structures, Structural Dynamics, and Materials Conference, San Antonio, Texas, 10-14 April 1972.

1-11. E. J. Seldin, "Stress-Strain Properties of Polycrystalline Graphites in Tension and Compression at Room Temperature," Carbon, July 1966, pp. 177-191.

1-12. H. S. Starrett and C. D. Pears, Probable and Average Properties of ATJ-S(WS) Graphite, Southern Research Institute, AFML-TR-73-14, Vol. 1, February 1973.

1-13. Personal communication with Dr. H. W. Babel of McDonnell-Douglas Astronautics Company, Western Division, Huntington Beach, California.

1-14. S. A. Ambartsumyan, "The Axisymmetric Problem of a Circular Cylindrical Shell Made of Material with Different Stiffness in Tension and Compression," Izvestiya akademii nauk SSSR, Mekhanika, No. 4 (1965), pp. 77-85. Translation available from STAR as N69-11070.

1-15. S. A. Ambartsumyan and A. A. Khachatryan, "Basic Equations in the Theory of Elasticity for Materials with Different Stiffness in Tension and Compression," Inzhenernyi zhurnal, Mekhanika tverdogo tela, No. 2 (1966), pp. 44-53. Translation available as

LRG-67-T-12, The Aerospace Corporation, El Segundo, California.

1-16. S. A. Ambartsumyan, "Equations of the Plane Problem of the Multimodulus Theory of Elasticity," Izvestiya akademii nauk armianskoi SSR, Mekhanika, Vol. 19, No. 2 (1966), pp. 3-19. Translation available as LRG-67-T-14, The Aerospace Corporation, El Segundo, California.

1-17. S. A. Ambartsumyan and A. A. Khachatryan, "Theory of Multimodulus Elasticity," Inzhenernyi zhurnal, Mekhanika tverdogo tela, No. 6 (1966), pp. 64-67. Translation available from STAR as N67-27610.

1-18. Robert M. Jones,"Buckling of Circular Cylindrical Shells with Different Moduli in Tension and Compression," AIAA Journal, January 1971, pp. 53-61.

1-19. S. A. Ambartsumyan, "Basic Equations and Relations in the Theory of Elasticity of Anisotropic Bodies with Differing Moduli in Tension and Compression," Inzhenernyi zhurnal, Mekhanika tverdogo tela, No. 3 (1969), pp. 51-61. Translation available as LRG-70-T-1, The Aerospace Corporation, El Segundo, California.

1-20. Robert M. Jones,"Buckling of Stiffened Multilayered Circular Cylindrical Shells with Different Orthotropic Moduli in Tension and Compression," AIAA Journal, May 1971, pp. 917-923.

1-21. N. G. Isabekian and A. A. Khachatryan, "On the Multimodulus Theory of Elasticity of Anisotropic Bodies in a Plane Stress State," Izvestiya akademii nauk armianskoi SSR, Mekhanika, Volume 22, No. 5, 1969, pp. 25-34. IAA Accession Number A70-22152. Translation available from Robert M. Jones.

1-22. J. K. Legg, H. S. Starrett, H. G. Sanders, and C. D. Pears, Mechanical and Thermal Properties of Mod 3, Southern Research Institute,

Air Force Materials Laboratory Report AFML-TR-73-14, Volume IV, September 1973.

1-23. D. Geiler, Thermostructural Analysis of Three-Dimensional Orthogonally Reinforced Carbon-Carbon Materials, The Aerospace Corporation, U. S. Air Force Space and Missle Systems Organization Report SAMSO-TR-74-164, 5 June 1974.

1-24. James G. Crose, ASAAS, Asymmetric Stress Analysis of Axisymmetric Solids with Orthotropic Temperature-Dependent Material Properties That Can Vary Circumferentially, TR-0172(S6816-15)-1, The Aerospace Corporation, San Bernardino, California, December 1971.

1-25. C. D. Pears, and H. S. Starrett, Polygraphites Subjected to Temperature Stress Loadings, Southern Research Institute, Air Force Materials Laboratory Report AFML-TR-73-59, March 1973.

1-26. James G. Crose, and Robert M. Jones, SAAS III, Finite Element Stress Analysis of Axisymmetric and Plane Solids with Different Orthotropic Temperature-Dependent Material Properties in Tension and Compression, TR-0059(S6816-52)-1, The Aerospace Corporation, San Bernardino, California, June 1971.

2-1. James G. Crose, and Robert M. Jones, SAAS III, Finite Element Stress Analysis of Axisymmetric and Plane Solids with Different Orthotropic Temperature-Dependent Material Properties in Tension and Compression, TR-0059(S6816-52)-1, The Aerospace Corporation, San Bernardino, California, June 1971.

2-2. Robert M. Jones and Dudley A. R. Nelson, Jr., Nonlinear Deformation of Graphitic Materials, Air Force Materials Laboratory Technical Report AFML-TR-74-259, Southern Methodist University, Dallas, Texas,

February 1975.

2-3. Robert M. Jones and Dudley A. R. Nelson, Jr., "A New Material Model for the Nonlinear Biaxial Behavior of ATJ-S Graphite," Journal of Composite Materials, January 1975, pp. 10-27.

2-4. Robert M. Jones and Dudley A. R. Nelson, Jr., "Further Characteristics of a Nonlinear Material Model for ATJ-S Graphite," Journal of Composite Materials, July 1975, pp. 251-265.

2-5. Robert M. Jones and Dudley A. R. Nelson, Jr., "Material Models for Nonlinear Deformation of Graphite," AIAA Journal, June 1976, pp. 709-717.

2-6. Robert M. Jones and Dudley A. R. Nelson, Jr., "Theoretical-Experimental Correlation of Material Models for Nonlinear Deformation of Graphite," AIAA Journal, October 1976, pp. 1427-1435.

2-7. S. A. Ambartsumyan, "Basic Equations and Relations in the Theory of Elasticity of Anisotropic Bodies with Differing Moduli in Tension and Compression," Inzhenernyi zhurnal, Mekhanika tverdogo tela, No. 3, 1969, pp. 51-61 (translation available as LRG-70-T-1 from The Aerospace Corporation, El Segundo, Calif).

2-8. H. S. Starrett and C. D. Pears, Probable and Average Properties of ATJ-S(WS) Graphite, Southern Research Institute, Birmingham, Alabama, Air Force Materials Laboratory Technical Report AFML-TR-73-14, Volume I, February 1973.

2-9. B. M. Lempriere, "Poisson's Ratio in Orthotropic Materials," AIAA Journal, November 1968, pp. 2226-2227.

3-1. H. S. Starrett and C. D. Pears, Probable and Average Properties of ATJ-S(WS) Graphite, Southern Research Institute, Birmingham, Alabama, Air Force Materials Laboratory Report AFML-TR-73-14, Volume I,

February 1973.

3-2. Robert M. Jones and Dudley A. R. Nelson, Jr., "A New Material Model for the Nonlinear Biaxial Behavior of ATJ-S Graphite," Journal of Composite Materials, January 1975, pp. 10-27.

3-3. Robert M. Jones and Dudley A. R. Nelson, Jr., "Further Characteristics of a Nonlinear Material Model for ATJ-S Graphite," Journal of Composite Materials, July 1975, pp. 251-265.

3-4. Robert M. Jones, "Stress-Strain Relations for Materials with Different Moduli in Tension and Compression," AIAA Journal, January 1977, pp.

3-5. Robert M. Jones and Dudley A. R. Nelson, Jr., "Material Models for Nonlinear Deformation of Graphite," AIAA Journal, June 1976, pp. 709-717.

3-6. Robert M. Jones and Dudley A. R. Nelson, Jr., "Theoretical-Experimental Correlation of Material Models for Nonlinear Deformation of Graphite," AIAA Journal, October 1976, pp. 1427-1435.

3-7. C. D. Pears and H. S. Starrett, Polygraphites Subjected to Temperature Stress Loadings, Southern Research Institute, Birmingham, Alabama, Air Force Materials Laboratory Report AFML-TR-73-59, March 1973.

3-8. J. Jortner, Uniaxial and Biaxial Stress-Strain Data for ATJ-S Graphite at Room Temperature, McDonnell-Douglas Astronautics Company, Huntington Beach, California, Report MDC G3564, June 1972.

3-9. James G. Crose and Robert M. Jones, SAAS III, Finite Element Stress Analysis of Axisymmetric and Plane Solids with Different Orthotropic, Temperature-Dependent Material Properties in Tension and Compression, TR-0059(S6816-53)-1, The Aerospace Corporation, San Bernardino,

California, June 1971.

3-10. MOATS Computer Program, Southern Research Institute undocumented version of OATS in-depth temperature response computer program developed by Frank C. Weiler, Weiler Research, Inc., Mountain View, Calif.

3-11. Robert M. Jones and Harold S. Morgan, "Analysis of Nonlinear Stress-Strain Behavior of Fiber-Reinforced Composite Materials," Presented at the 17th AIAA/ASME/SAE Structures, Structural Dynamics, and Materials Conference, Valley Forge, Pennsylvania, 5-7 May 1976. Submitted to AIAA Journal.

3-12. Duane L. Baker, H. Stuart Starrett, and C. L. Budde, Thermostructural Testing of Instrumented ATJ-S Graphite Shell Nosetips in the AFFDL 50 MW Facility, Aerotherm Division/Acurex Corporation, Mountain View, California and Southern Research Institute, Birmingham, Alabama, Air Force Materials Laboratory Technical Report AFML-TR-75-26, April 1976.

3-13. Frank C. Weiler, DOASIS, A Computer Program for the Deformation Plastic, Orthotropic, Axisymmetric (and Plane) Solution of Inelastic Solids, Volumes I-III, Weiler Research, Inc., Mountain View, Calif., Air Force Materials Laboratory Technical Report AFML-TR-75-37, September 1975.

3-14. Robert M. Jones and Dudley A. R. Nelson, Jr., Nonlinear Deformation of Graphitic Materials, Air Force Materials Laboratory Technical Report AFML-TR-74-259, Southern Methodist University, Dallas, Texas, February 1975.

3-15. James G. Crose, personal communication, Prototype Development Associates, Inc., Santa Ana, California, Spring 1976.

3-16. Samuel B. Batdorf, Fracture Statistics of Brittle Materials with Intergranular Cracks, The Aerospace Corporation, El Segundo, California, U. S. Air Force Space and Missile Systems Organization Technical Report SAMSO-TR-74-210, October 1974.

4-1. Robert M. Jones, "Stress-Strain Relations for Materials with Different Moduli in Tension and Compression," AIAA Journal, January 1977.

4-2. K. M. Kratsch, J. C. Schutzler, and D. A. Eitman, "Carbon-Carbon 3-D Orthogonal Material Behavior," AIAA Paper No. 72-365, AIAA/ASME/SAE 13th Structures, Structural Dynamics, and Materials Conference, San Antonio, Texas, 10-14 April 1972.

4-3. J. K. Legg, H. S. Starrett, H. G. Sanders, and C. D. Pears, Mechanical and Thermal Properties of Mod 3, Southern Research Institute, Birmingham, Alabama, Air Force Materials Laboratory Technical Report AFML-TR-73-14, Volume IV, September 1973.

4-4. James G. Crose, Structural Assessment of Carbon-Carbon Materials for the Carbon-Carbon Assessment Program (CCAP), Prototype Development Associates, Inc., Costa Mesa, California, PDA Report No. 1011-00-01, January 1974.

4-5. H. S. Starrett, F. C. Weiler, and C. D. Pears, Thermostructural Response of Carbon-Carbon Materials under High Heat Flux Environments, Southern Research Institute, Birmingham, Alabama, Air Force Materials Laboratory Technical Report AFML-TR-73-255, Volume I, February 1974.

4-6. Eric M. Ross, The Carbon-Carbon Assessment Program, Air Force Materials Laboratory Technical Report AFML-TR-74-39, September 1974.

4-7. J. K. Legg and C. D. Pears, Mechanical and Thermal Properties of

Mod 3a, A Pierced Fabric Carbon-Carbon Material, Southern Research Institute, Birmingham, Alabama, Air Force Materials Laboratory Technical Report AFML-TR-74-211, December 1974.

4-8. J. K. Legg, H. G. Sanders, H. S. Starrett, W. T. Engelke, and C. D. Pears, The Carbon-Carbon Assessment Program, Supplement I (Appendix A), Materials Characterization, Southern Research Institute, Birmingham, Alabama, Air Force Materials Laboratory Technical Report AFML-TR-74-39, Supplement I, January 1975.

4-9. J. K. Legg, H. G. Sanders, H. S. Starrett, W. T. Engelke, and C. D. Pears, The Carbon-Carbon Assessment Program, Supplement 5 (Appendix E), Failure Analysis, Southern Research Institute, Birmingham, Alabama, Air Force Materials Laboratory Technical Report AFML-TR-74-39, Supplement 5, January 1975.

4-10. H. S. Starrett and C. D. Pears, Elastic Compliances for ATJ-S Graphite and Mod 3a Carbon-Carbon, Southern Research Institute, Birmingham, Alabama, Air Force Materials Laboratory Technical Report AFML-TR-74-271, February 1975.

4-11. H. S. Starrett, F. C. Weiler, and C. D. Pears, Thermostructural Response of Carbon-Carbon Materials under High Heat Flux Environments, Southern Research Institute, Birmingham, Alabama, Air Force Materials Laboratory Technical Report AFML-TR-74-232, June 1975.

4-12. "Standard Methods of Test for Flexural Properties of Plastics," ASTM D 790 - 71, American Society for Testing and Materials, 1971.

4-13. Tommy R. Guess and Charles W. Bert, "Material Design Concepts for Filament-Wound, Graphite-Graphite Heatshields," Journal of Spacecraft and Rockets, March 1972, pp. 165-172.

4-14. E. M. Lenoe, D. W. Oplinger, and J. C. Serpico, "Experimental Studies of Three-Dimensionally Reinforced Composite Shells," AIAA

Paper No. 69-122, AIAA 7th Aerospace Sciences Meeting, New York, New York, 20-22 January 1969.

4-15. J. Jortner, Biaxial Mechanical Properties of ATJ-S Graphite, Final Report under AF Contract F04701-068-C-0288, Change Order 15, McDonnell-Douglas Report No. MDC G 2072, December 1970.

4-16. James G. Crose, ASAAS, Asymmetric Stress Analysis of Axisymmetric Solids with Orthotropic Temperature-Dependent Material Properties That Can Vary Circumferentially, TR-0172(S6816-15)-1, The Aerospace Corporation, San Bernardino, California, December 1971.

4-17. Julius Jortner, Biaxial Tensile Fracture of ATJ-S Graphite, McDonnell Douglas Astronautics Company, Huntington Beach, California, Air Force Materials Laboratory Technical Report AFML-TR-74-262, March 1975.